THÈSE DE DOCTORAT EN COTUTELLE DE L'UNIVERSITÉ DE LILLE ET DE L'UNIVERSITÉ SUN YAT-SEN

réalisée au sein de

École doctorale n°632 : Sciences de l'Ingénierie et des Systèmes – ENGSYS

Laboratoire de Génie Civil et Géo-Environnement – LGCgE ULR4515

Étude de l'effet de l'eau sur les propriétés interfaciales et de frottement des minéraux du sol par dynamique moléculaire

Molecular dynamics study on the effect of water on the interfacial and frictional properties of expansive soil minerals

Thèse soutenue publiquement le 07/11/2023, par

Pengchang WEI

pour obtenir le grade de

DOCTEUR en Mécanique, génie mécanique, génie civil de L'UNIVERSITE DE LILLE
Devant le jury composé de:

Siham KAMALI-BERNARD	INSA-Rennes	Professeur	Président
Andrey G. KALINICHEV	SUBATECH (UMR 6457 - IMT Atlantique)	Directeur de Recherche	Rapporteur
Wei YANG	University of Hunan (China)	Professeur	Rapporteur
Xue-You LI	Sun Yat-Sen University (China)	Professeur	Examinateur
Ali ZAOUI	Université de Lille	Professeur	Direction de thèse
Yuanyuan ZHENG	Sun Yat-Sen University (China)	Professeur	Direction de thèse

Laboratoire
de Génie Civil
et géo-Environnement

Abstract

Expansive soil mainly comprises detrital minerals (e.g., quartz) and clay minerals (such as montmorillonite, kaolinite, etc.). Due to the existence of the hydrophilic mineral montmorillonite, the expansive soil has the deformation characteristics of water absorption expansion and water loss shrinkage, which could seriously affect the stability of engineering structures. For expansive soil in permafrost regions, the mechanical properties of the frozen soil could change due to the phase transformation between unfrozen water and ice caused by temperature changes, which could easily cause engineering problems such as frost heave or thaw settlement deformation. At present, lots of researchers have focused more on the interface friction of expansive soil minerals, their interaction with ice water multi-media, and the mechanical properties of ice in macroscale. However, there is relatively little exploration in microscale. Especially, the study on the interfacial friction behavior of minerals in microscale (nano-tribology) is a new field that needs to be developed urgently. Moreover, the research on the ice-water phase transformation process on clay mineral interface is rarely reported.

In this PhD dissertation, molecular dynamics (MD) simulation method is employed to investigate the interfacial and frictional properties of expansive soil minerals. The hydrated montmorillonite, quartz-quartz/kaolinite-(water) interface model, montmorillonite-water-ice, and bulk ice models were established, to reveal the interface friction mechanism of expansive soil minerals at microscale, clarify the process of ice water phase transformation on clay interface, and explore the deformation and failure mechanism and phase transformation process of bulk ice system. The main conclusions obtained are as follows:

(1) **Effect of water on the frictional and mechanical behavior of montmorillonite: a MD study**

The hydrated montmorillonite models with different water contents for friction tests were established, revealing the friction mechanism of montmorillonite in nanoscale. The simulation results found that the low friction coefficient of 0 ~ 30% hydrated montmorillonite was 0.058 ~ 0.17, where the friction coefficient of 5% hydrated montmorillonite is the highest. The distribution of interlayer water could further change when normal load changed. The interlayer

water could greatly reduce the attraction force between clay layers.

(2) Nanoscale Friction at the Quartz-Quartz and Quartz-Clay Interface

The five quartz-quartz/clay-(water) interface model (including quartz-quartz, quartz-water-quartz, quartz-kaolinite, quartz-water-kaolinite, and quartz-montmorillonite) for friction test were established, and then revealing their friction mechanism considering the normal load, sliding velocity, temperature, and hydration. The simulation results showed that the stick-slip effect was found in the quartz-quartz/clay-(water) interface during the friction process. The presence of clay could weaken the frictional strength of quartz. The friction coefficient and cohesion of quartz rose with the rising sliding velocity or decreasing temperature. The relationship between shear stress and normal load was linear in nanoscale friction.

(3) Phase Transformation of Ice-Unfrozen Water on Montmorillonite Surface: a Molecular Dynamics Study

Based on the results of nuclear magnetic resonance and molecular simulation, the microscopic mechanism of the ice-water phase transformation process on montmorillonite interface was revealed. The main reason for unfrozen water in frozen soil was the surface effect of clay, where coulomb electrostatic interaction dominated. The microstructure of unfrozen water and ice on clay particles could be divided into "montmorillonite-bound water-cubic ice-hexagonal ice-cubic ice-'quasi-liquid' water-air".

(4) Phase Transformation Evolution and Mechanical Properties of Bulk Ice under Tension at Nanoscale

The mechanical behavior of ice-Ih with the effect of temperature and confining pressure and ice-water phase transformation in bulk ice system were studied. The simulation results indicated that solid-solid phase transformation was found at $73 \sim 140$ K, and solid-liquid at $150 \sim 270$ K. Phase transformation significantly affected total potential energy and structural failure. Tensile strength decreased linearly with increasing temperature at a low strain rate. Ice-Ih was earlier and more likely to be melted at higher confining pressure.

Keywords: Clay minerals; Quartz; Molecular dynamics; Interfacial friction; ice-water phase transformation.

Résumé

Les sols expansés sont principalement composés de minéraux détritiques tels que le quartz et de minéraux argileux tels que la Montmorillonite, la Kaolinite, etc. en raison de la présence de Montmorillonite minérale hydrophile, les sols expansés ont des caractéristiques de déformation qui absorbent l'expansion de l'eau et la contraction de la perte d'eau, ce qui affecte gravement La stabilité de la structure d'ingénierie. Pour les sols expansés dans les zones de pergélisol, les propriétés mécaniques du sol gelé peuvent varier en raison de la transition de phase entre l'eau non gelée et la glace causée par les changements de température, ce qui peut causer des problèmes d'ingénierie tels que le gonflement par le gel ou la déformation par sédimentation. À l'heure actuelle, de nombreux chercheurs se concentrent davantage sur le frottement Interfacial des minéraux des sols en expansion, leur interaction avec les multimilieux eau - glace et les propriétés macromécaniques de la glace. Cependant, il y a relativement peu d'exploration à l'échelle microscopique. L'étude du comportement de frottement Interfacial des minéraux (nanotribologie) en particulier à l'échelle microscopique est un nouveau domaine à développer d'urgence. De plus, peu d'études ont été menées sur les processus de changement de phase eau - glace à l'interface argile - minéral.

Cet article examine les propriétés interfaciales et de frottement des minéraux des terres expansées à l'aide d'une méthode de simulation de dynamique moléculaire (MD). La Montmorillonite hydratée, le modèle d'interface quartz - quartz / Kaolinite - (eau), la Montmorillonite - glace d'eau, le modèle de glace de bloc ont été établis, révélant le mécanisme de frottement Interfacial des minéraux de terre expansée à l'échelle microscopique, clarifiant le processus de changement de phase eau - glace sur l'interface argileuse, explorant le mécanisme de destruction de la déformation et le processus de changement de phase du système de glace de bloc. Les principales conclusions sont les suivantes:

(1) Effet de l'eau sur le comportement mécanique par frottement de la Montmorillonite: étude MD

Un modèle d'essai de frottement du monticule hydraté avec différentes teneurs en eau a été établi, révélant le mécanisme de frottement du monticule à l'échelle nanométrique. Les résultats

des simulations montrent que le coefficient de frottement faible de 0 à 30% de Montmorillonite hydratée est de 0058 à 0,17, dont 5% de Montmorillonite hydratée a le coefficient de frottement le plus élevé. La redistribution de l'eau entre les couches peut se développer davantage lorsque la charge normale varie. L'eau inter - couches peut réduire considérablement les interactions entre les couches d'argile.

 (2) nanofriction aux interfaces quartz - quartz et quartz - argile

Cinq modèles d'interface quartz - quartz / argile - (eau) ont été établis pour les essais de frottement (y compris quartz - quartz, quartz - eau - quartz, quartz - kaolinite, quartz - eau - kaolinite et quartz - montmorillonite) et ont révélé leurs mécanismes de frottement en tenant compte de la charge normale, de La vitesse de glissement, de la température et de l'action de l'hydratation. Les résultats des simulations montrent qu'il existe un effet de viscosité à l'interface quartz - quartz / argile - (eau) pendant le frottement. La présence d'argile affaiblit la résistance au frottement du quartz. Le coefficient de frottement et la cohésion du quartz augmentent avec une augmentation de la vitesse de glissement ou une diminution de la température. La relation entre la contrainte de cisaillement et la charge normale est linéaire dans le nanofrottement.

(3) Étude de la dynamique moléculaire des changements de phase de l'eau non gelée à la surface de la Montmorillonite

En combinant les résultats de la résonance magnétique nucléaire et de la simulation moléculaire, les mécanismes microscopiques du processus de changement de phase eau - glace à l'interface Montmorillonite ont été révélés. La principale raison de la présence d'eau non gelée dans le sol gelé est l'effet de surface de l'argile, où l'interaction électrostatique coulombienne prédomine. La Microstructure de l'eau et de la glace non gelées sur les particules d'argile peut être divisée en "glace cubique d'eau liée à la Montmorillonite glace cubique hexagonale -" quasi liquide "eau - air".

(4) Evolution de changement de phase et propriétés mécaniques de grands blocs de glace sous étirement à l'échelle nanométrique

On a étudié le comportement mécanique de la glace IH sous l'influence de la température, de la pression de confinement et de la transition de phase eau - glace dans un système de glace de grand volume. Les résultats des simulations montrent que la transition de phase solide - solide

se produit entre 73 et 140 K et la transition de phase solide - liquide se produit entre 150 et 270 K. la transition de phase a un impact important sur l'énergie potentielle totale et la défaillance structurelle. La résistance à la traction diminue linéairement avec l'augmentation de la température à faible vitesse de déformation. La glace IH est plus tôt et plus susceptible de fondre à des pressions de confinement plus élevées.

Mots clés : Minéraux argileux; Quartz; Dynamique moléculaire; Friction de l'interface; Changement de phase eau - glace.

Acknowledgments

Contents

Chapter 1. General introduction

1.1 Research background

Expansive soil is distributed in more than 60 countries and regions on six continents worldwide, mainly containing detrital minerals (e.g., quartz) and clay minerals (e.g., montmorillonite, kaolinite, etc.). Based on the classification of clay minerals, expansive soils could be classified into two categories: one is mainly montmorillonite, and the other is primarily illite and kaolinite. Moreover, expansive soil has significant deformation characteristics of water absorption expansion and water loss contraction due to strong hydrophilic montmorillonite clay [1, 2]. According to relevant data statistics, the construction area caused by expansive soil foundation in China exceeds 10^8 m^2, and the annual economic loss exceeds 90 billion RMB [3]. Expansive soil is known as "engineering cancer" due to its typical properties (such as swelling shrinkage, cracking, and overconsolidation), and then causing engineering disasters easily under external environmental [4]. In addition, the stability of the geotechnical structure largely depends on the stability of the main constituent minerals (or weak minerals) to environmental changes. Research on special rocks and soils such as expansive soil [5], loess [6], bentonite [7], and soft rock [8] showed that layered clay minerals were extremely sensitive to environmental changes. In many natural and engineering environments, layered clay minerals could affect and control the mechanical properties of soil and participate in solute transport, so they played a crucial role in the multi-scale evolution of many rocks and soil structures [9]. For example, the destruction of large landslides on rocks and soils and even the initial structural change might start from the deformation of clay minerals or the change of sedimentary mode.

The macroscopic behavior of geotechnical materials is the cumulative manifestation of their microstructure changes [9]. For example, Zhu et al. [10] reported that clay-based materials' deformation at macroscale was controlled by the local motion of clay particles and their aggregates at microscale, and clay particles played a dominant role in the failure and deformation process. They also pointed out that the characterization of the mechanical behavior

of soil should be based on multi-scale methods to consider the effects of mineral composition and multi-scale heterogeneity appropriately. Furthermore, the thermal effect, hydration effect, and anisotropic mechanical behavior of clay particles at nanoscale are closely related to the macroscopic mechanical behavior of clay-based materials [11-13]. Therefore, to fundamentally understand the mechanical behavior of expansive soil, it is essential to study its main minerals at microscales.

As is well known, the sliding (or shearing) between clay particles plays an essential role in the deformation of clay. The friction characteristics between clay particles are the basis for determining the mechanical properties of clay [14]. Montmorillonite in expansive soil minerals has a high ion exchange property [15], water swelling property and adsorption property [16], and weak friction property [17-19]. Previous studies have shown that montmorillonite was a vital component in affecting the failure strength of soil samples and controlling the fracture strength [17, 18]. For example, Sakuma et al. [20] reported that montmorillonite could significantly reduce the strength of crustal faults and may cause the creep of natural faults in the absence of major earthquakes. Moreover, the abnormal large slip (50~80 m) of the 2011 Northeast Japan earthquake was attributed to the thin and weak clay (e.g., montmorillonite) in the fault zone [21, 22]. Meanwhile, the friction behavior between different mineral particles, such as quartz-montmorillonite, quartz-kaolinite, etc., is also worth exploring. During the sliding process of mineral particles, it is difficult for macroscopic tests to reveal what happens on their contact surface accurately. Krim [23] pointed out that more information on the basic mechanisms of friction could be found in atomic scale. Therefore, it is necessary to explore the interfacial friction behavior between expansive soil mineral particles at the molecular/atomic level.

On the other hand, there are also many expansive soils in seasonally frozen regions of some countries [24-26], which undergo conventional dry wet cycles and freeze-thaw cycles, easily causing some engineering problems. Expansive soil in seasonally frozen soil areas is a four-phase complex composed of solid particles, ice, liquid water (unfrozen water), and gas [27]. The mutual transformation between ice and unfrozen water in frozen soil was directly affected by temperature changing, causing the change in the physical and mechanical properties of frozen

soil, ultimately leading to engineering problems such as frost heave and thaw settlement [27, 28]. At present, it is challenging to directly study some microscopic mechanisms of frozen soil through physical testing methods, such as the transformation of liquid water phase into ice and migrating unfrozen water in frozen soil [29]. It was due to the complex chemical composition, small size, and complex surface properties of clay mineral particles. Thus, it is worth exploring the ice-water phase transformation process on montmorillonite interface and the phase transformation process of pure ice systems and its deformation mechanism under external loads through microscale analysis method.

The traditional research on the mechanical properties of clay is mainly carried out through theoretical and experimental means. Some current microstructural mechanics theories are still in their infancy [30], and are not applicable to analyze some special geotechnical problems. For theoretical derivation, many assumptions are often proposed, causing theoretical descriptions which cannot fully reflect the actual situation of the material. On the other hand, the stress response and structural changes of materials could be obtained by experiment, but often lacking quantitative explanations and ignoring some fundamental mechanisms. At the same time, it is challenging to prepare samples and requires high test equipment, such as nanoindentation and atomic force microscopy tests [31]. Moreover, it is difficult to accurately obtain the internal structural changes and micromechanical properties of expansive soil minerals, due to the limitation of the geometric size of expansive soil minerals and test equipment [32, 33].

With the rapid development of computer technology, computer simulation technology has become the third important research tool independent of theoretical analysis and experimental research, serving as a bridge between theory and experiment. The finite element and discrete element methods are commonly used in geotechnical engineering, and could better predict macroscopic properties. However, they have certain limitations when dealing with small-scale (micro/nano scale) geotechnical and mechanical problems. For example, these methods are difficult to predict the swelling behavior of expansive soil [34, 35]. In the past few decades, molecular dynamics (MD) simulation methods have developed into a good tool suitable for solving specific problems in materials science, which could effectively solve the above issues

and have been widely applied to study the thermodynamic properties, interface behavior, and multi-medium interactions of geotechnical materials at microscale [36-38]. This method could make the "black box" of geotechnical materials transparent, thereby revealing more basic physical and mechanical mechanisms, and providing a basis for the mechanism interpretation of macroscopic and mesoscopic simulation results.

In this PhD dissertation, MD simulation method has been employed to explore the nanoscale interfacial friction behavior of hydrated montmorillonite and quartz-kaolinite-water, and further revealing the friction mechanism of expansive soil mineral interface at microscale by considering different hydration degrees, normal loads, sliding velocity, etc. The phase transformation process of ice-water on montmorillonite interface was discussed, and analyzing the evolution law of unfrozen water with temperature change, as well as revealing the interface effect of clay minerals. Finally, the deformation and failure mechanism and phase transformation process of pure ice systems under external loads was investigated. Interpreting macroscopic phenomena from the essential properties of microstructure, provides a theoretical basis at the microscale for the study of the mechanical performance of expansive soil and the surface characteristics of mineral particles.

1.2 Research objectives and shortcomings in current research

The main research objectives of this PhD dissertation are as follows:

(1) Clarifying the fundamental mechanism: providing the mechanism explanation of the interface friction behavior of expansive soil minerals and the interaction between clay minerals and ice-water.

(2) Explaining the experimental phenomenon or data: (a) Why the unfrozen water content in frozen soil increases with increasing temperature? (b) Why does the stick-slip effect occur during the nanoscale friction process?

(3) Predicting the behavior of materials: (a) Exploring the effects of various influencing factors on the frictional behavior between mineral particles. (b) How does the phase transformation process between unfrozen water and ice occur in frozen soil, and how is the phase composition distributed?

Based on the previous works mentioned in Section 1.1, the shortcomings of current research studies are collected in Table 1-1.

Table 1-1 Shortcomings of current research studies, based on previous works.

Research subject	Shortcomings of current research studies
The frictional behavior of expensive soil minerals	1) It is difficult to accurately reveal the friction mechanism of the mineral particles interface through friction and shear experiments; 2) The study of nano-tribology of minerals is a new field that urgently needs to be developed; 3) The impact of external environmental factors such as normal load, sliding velocity, and hydration state on the nanoscale friction mechanism and structural properties of rock/soil materials is still unclear.
Ice-water phase transformation behavior on clay minerals surface	1) The physical process of ice-water phase transformation cannot be directly observed using physical experimental methods, and it is also difficult to reveal the microscopic mechanisms involved; 2) Most experimental methods are used to measure the unfrozen water content in frozen soil to analyze the problem of ice water phase transformation. Moreover, the ice nucleation process at kaolinite interface has been mostly concerned currently. However, research on the ice-water phase transformation process at the hydrophilic mineral montmorillonite interface has not been reported yet.
The mechanical behavior and phase transformation process of bulk ice	1) The effect of temperature and confining pressure on the tensile dynamic mechanical behavior of ice at a low strain rate and its phase transformation is still unclear. 2) The following questions need to be answered: a) Under tensile loading with a low strain rate, could the anomalous temperature effect still be found? b) Does the water-ice phase transition depend on temperature? c) How does the confining pressure affect the microstructure and failure path of ice?

1.3 Research contents

Figure 1-1 and Table 1-2 show the technology roadmap and main research contents of this PhD dissertation, respectively.
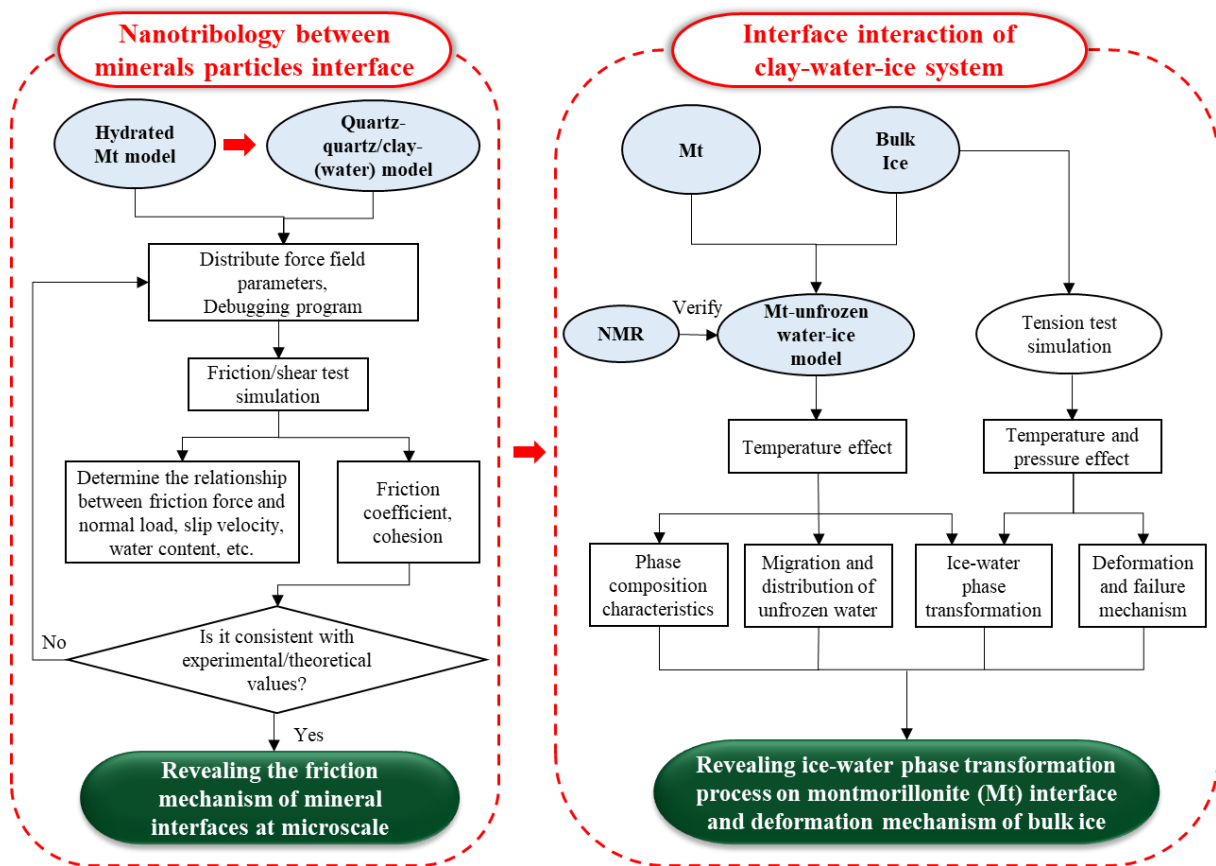
Figure 1-1. Technology roadmap of this PhD dissertation

Table 1-2 Main research contents of this PhD dissertation

Chapter	Main research content
Chapter 1. General introduction	1) Introduction to the main research background of expansive soil minerals; 2) Introduction to the research objectives of this PhD dissertation. 3) Introduction to the research content of each chapter in this PhD dissertation.
Chapter 2. Introduction to minerals and Molecular Dynamic simulation	1) Introduction to the structural composition of quartz, montmorillonite, and kaolinite; 2) Introduction to MD simulation method, including its development history, basic principles, and other important content; 3) Introduction to some data analysis.

Chapter 3. Effect of water on the frictional and mechanical behavior of montmorillonite: A MD study	1) Established the different hydrated montmorillonite models for friction test; 2) Studying the effects of normal load and water content on the interfacial friction behavior of montmorillonite particles; 3) Deriving the friction coefficient, then verifying the accuracy of the established model and applied force field by comparing the results of previous experiments and simulations.
Chapter 4. Nanoscale Friction at the Quartz-Quartz and Quartz-Clay Interface	1) Established the four quartz-quartz/kaolinite-(water) interface model (including quartz-quartz, quartz-water-quartz, quartz-kaolinite, and quartz-water-kaolinite) for friction test; 2) Investigating the effects of normal load, sliding velocity, temperature, and hydration on the interfacial friction behavior of quartz-quartz/kaolinite-(water) interface model; 3) Discussing the effect of normal load, hydration, and sliding velocity on the stick-slip effect.
Chapter 5. Phase Transformation of Ice-Unfrozen Water on Montmorillonite Surface: A Molecular Dynamics Study	1) Established the initial montmorillonite-unfrozen water-ice model; 2) Exploring the evolution process of ice water phase transformation on montmorillonite interface at different undercooled temperatures; 3) Analyzing the phase composition characteristics in the system and exploring the migration and distribution of unfrozen water; 4) Revealing the microscopic mechanism of the ice water phase transformation process on montmorillonite interface.
Chapter 6. Phase Transformation Evolution and Mechanical Properties of Bulk Ice under Tension at Nanoscale	1) Establishing the bulk ice-Ih model; 2) Exploring the deformation and failure mechanism of ice under temperature-pressure effect; 3) Studying the phase transformation of ice-water under external load.
Chapter 7. Summary and perspectives	Introduction to the conclusion, main innovation points, and perspectives of this PhD dissertation.

Chapter 2

Introduction of clay minerals and MD method

Chapter 2. Introduction of clay minerals and MD method

2.1 Clay minerals: montmorillonite and kaolinite

As shown in Figure 2-1(a) and Figure 2-2(a), montmorillonite, 2:1 type layered silicate clay mineral, and its structural unit is a sandwich crystal structure consisting of two silica tetrahedron layer (Figure 2-2(b)) sandwiched with one aluminum oxide (hydrogen) octahedron layer (Figure 2-2(c)). Natural montmorillonite could be regarded as being made of pyrophyllite (structural formula: $Si_4Al_2O_{10}(OH)_2$) in which part of the silicon atoms (Si) in the silicon oxygen tetrahedron layer are replaced by aluminum atoms (Al), and part of the aluminum atoms (Al) in the aluminum oxide octahedron layer are replaced by iron (Fe), magnesium (Mg) and other low-price metal atoms. The negative charges in clay minerals existed due to the above atom substitutions, which must be balanced by the adsorption of a certain number of cations to achieve electrical neutrality. Among them, the atom substitution of montmorillonite mainly occurs in aluminum oxide octahedrons. In addition, the adjacent sheet layers of montmorillonite are mostly intermolecular Van der Waals force, with weak gravity. The cations in the upper layer are easy to hydrate, and water molecules easily enter the layers, so montmorillonite has a relatively large expansion. Montmorillonite has been widely used in sewage and nuclear waste treatment, shale gas exploitation, oil drilling, nanocomposite materials, medicine, catalysts, and catalyst carriers due to its high ion exchange, water swelling, and adsorption properties [39-41].

As shown in Figure 2-1(b), kaolinite (structural formula: $Al_2Si_2O_5(OH)_4$) is a 1:1 type layered silicate clay mineral, and its structural unit is composed of one layer of silica tetrahedron and one layer of alumina octahedron. There is no atom substitution in kaolinite, so it is electrically neutral without interlayer absorb cations. The hydrogen bonds between kaolinite layers are composed of hydrogen atoms and oxygen atoms on the surface, where its connection force is much greater than the Van der Waals force between montmorillonite layers. Thus, kaolinite does not have expansibility.

9

(a) montmorillonite [15]   (b) kaolinite
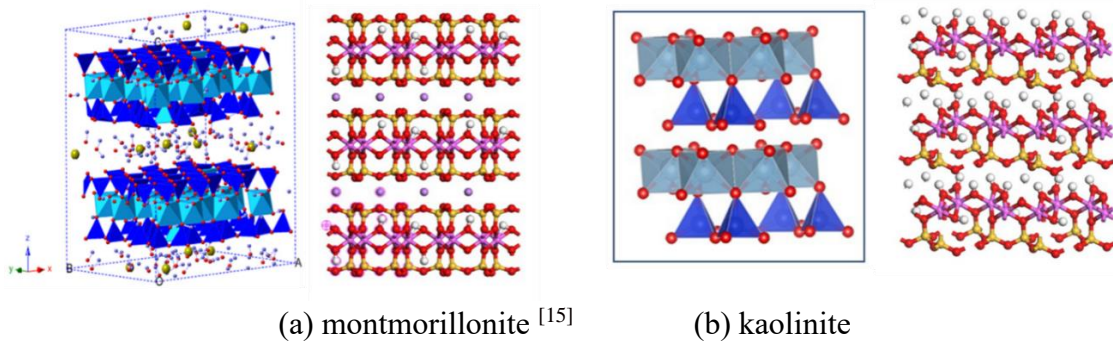
Figure 2-1. Crystal structure of layered silicate clay minerals of montmorillonite
(2:1 type) and kaolinite (1:1 type)
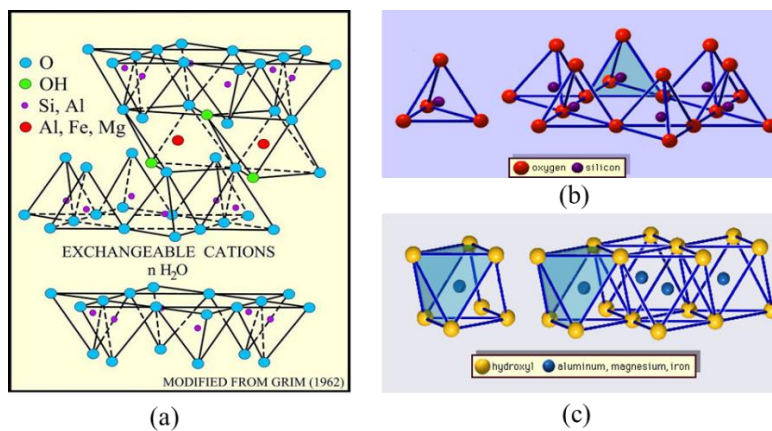
Figure 2-2. (a) Schematic diagram of the structure of montmorillonite; (b) silico-
oxygen tetrahedrons and silico-oxygen tetrahedrons arranged in a hexagonal
network; (c) The sheet structure of the aluminoxy-octahedral element and the
aluminoxy-octahedral element. [42]

The tetrahedron and octahedron units are made up of atoms, then form thin sheets, stack into layers, and combine to produce different clay mineral groups, as shown in Figure 2-3. The basic structure shown in the bottom row of the figure contains the vast majority of clay mineral types found in rocks and soils. It is convenient to distinguish the type of clay minerals according to crystal structure and stacking order of layers, where members of the same group usually have similar engineering properties.

As shown in Figure 2-3, the difference between 2:1 type clay mineral mainly lies in the type and quantity of "glue" that binds two clay layers together. For example, montmorillonite has loose cations between layers, while illite contains potassium ions embedded on the surface of the mineral layer, and vermiculite has a layer of organized water and cations.
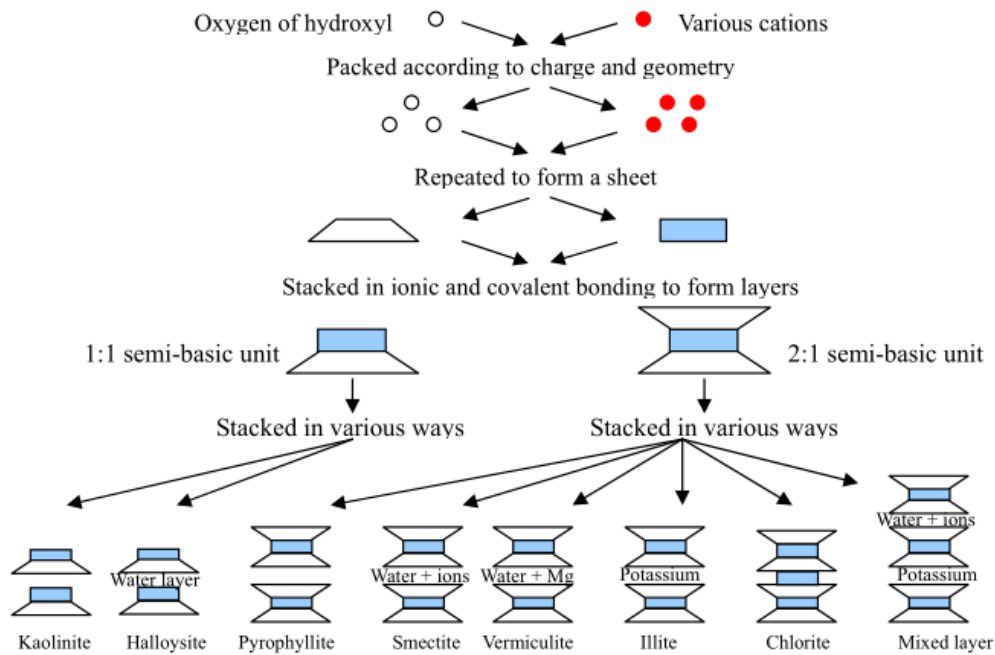
Figure 2-3. Synthesis pattern for the clay minerals [43]

2.2 Molecular Dynamic simulation method

2.2.1 Method introduction

With the rapid development of computer technology, multi-scale numerical simulation methods have been constantly developed (see Figure 2-4). According to the scale of time and space, four scales could be proposed: macroscopic, mesoscopic, microscopic, and nanoscale (or atomic), where each scale has corresponding numerical simulation methods (see Table 2-1).

Table 2-1. Correspondence between various material simulation methods and space-time scale.

Scale	Representative simulation methods	Space scale (m)	Time scale	Basic unit	Theoretical basis	Typical applications
nanoscale (or atomic)	First principles	$10^{-10} \sim 10^{-8}$ (Could handle hundreds of atoms)	ps (10^{-12} s)	Electrons /nuclei	quantum mechanics	The structure of single lattice defects, their dynamic characteristics, and the calculation of various constants of materials

microscopic	Molecular dynamics method, Monte Carlo method, molecular force field	$10^{-10} \sim 10^{-6}$ (Atoms number can reach the order of 1012)	μs $(10^{-6}$ s)	Atom (ignoring Electronic effect)	Quantum mechanics /Classical mechanics /Statistical mechanics	The Structure and Dynamic Characteristics of Lattice Defects
mesoscopic	Dislocation dynamics, Dissipative particle dynamics, etc	$10^{-9} \sim 10^{-4}$	ms $(10^{-3}$ s)	Beads/ Some Atoms	Defect Mechanics and Phase Transformation Mechanics	Crystal plasticity, regeneration and recovery, microstructure, dislocation distribution map, thermal activation energy
macroscopic	Finite element method, boundary element method, Finite difference method	$10^{-5} \sim 100$	s	Grid	Continuum mechanics	Average solution of difference equation at macro scale (mechanics, Electromagnetism, hydrodynamics, temperature field, etc.)

Computer molecular simulation technology is a microscopic experimental method that can be used for both theoretical research and experimental verification. It can not only simulate the molecular structure of various substances, but also predict the properties of materials. In addition, it can also simulate the dynamic changes in the reaction process of substances and explain the experimental phenomena observed at the macro scale. Computer molecular simulation technology mainly includes Molecular mechanics simulation technology (MM), molecular dynamics simulation method (MD), and Monte Carlo simulation method (MC).

MD simulation method is a comprehensive technology combining physics, chemistry, and mathematics, and is also an effective method for computing complex molecular systems. The research object of MD simulation is molecules or atoms, following Newton's second law, solving the interaction potential function and equations of motion between classical particles (particles are regarded as rigid bodies, ignoring electronic effect), and then analyzing the

behavior law of particle motion. Based on statistical mechanics, the instantaneous average behavior of many particles are replaced by the long-term average behavior of a few particles, that is, the macroscopic physical quantities of a macroscopic object, such as temperature, pressure, energy, stress, etc. Moreover, in recent decades, MD simulation technology has been widely applied in many fields such as physical chemistry, materials science, life science, earth science, environmental protection, and environmental geotechnical engineering, due to its high accuracy, fast speed, and enormous computational system [44, 45]. The number of published articles has increased yearly（Figure 2-5(a)). The number of articles applying molecular dynamics to geotechnical engineering is also constantly increasing (Figure 2-5(b)).
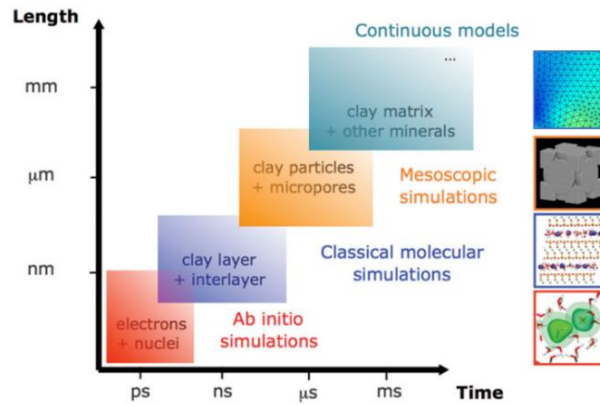
(a) Schematic diagram of multi-scale numerical simulation for handling clay (with minor modifications in this work) [46]
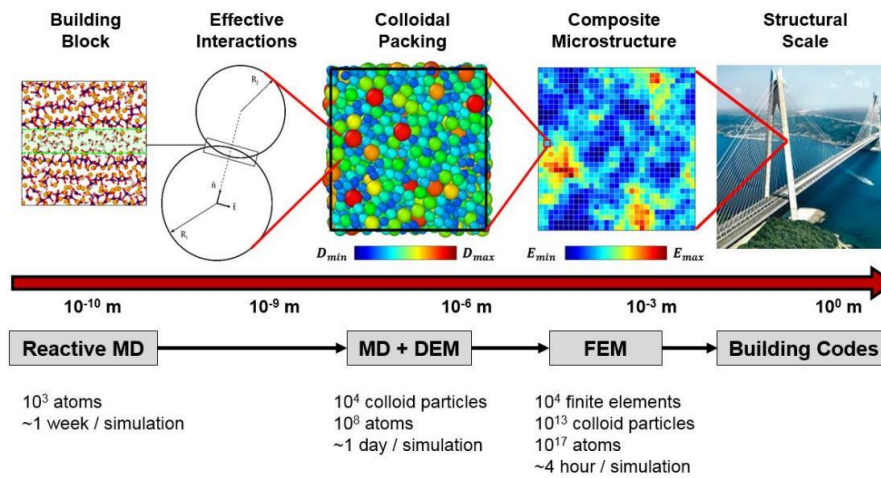
(b) A multi-scale framework for converting atomic behavior into engineering scale [47]

Figure 2-4. Multi-scale numerical simulation methods

(a)   (b)
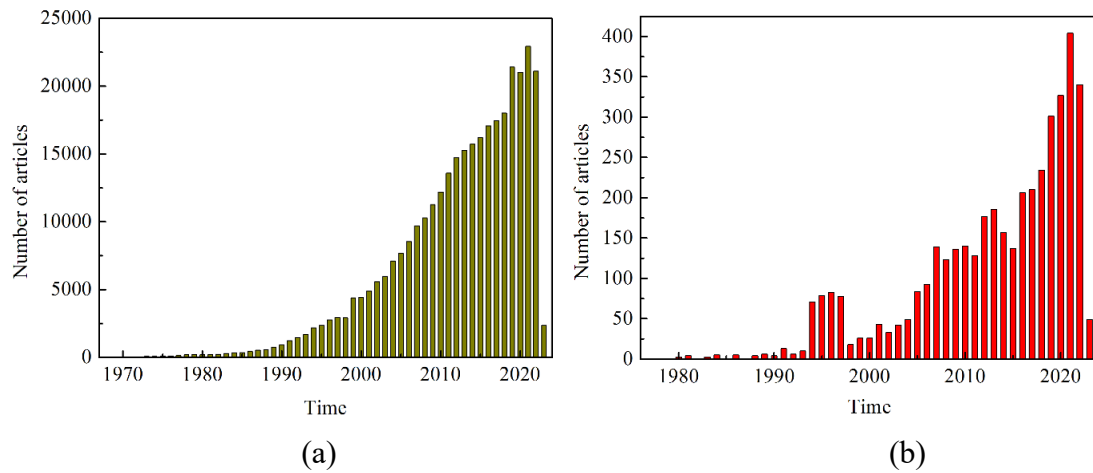
Figure 2-5. The number of articles published on Web of science based on different topic keywords: (a) the topic keyword of "Molecular dynamics simulation" (1968-2023.02); (b) Thematic keywords: "Molecular dynamics simulation" and "Soil or rock" (1977-2023.02).

2.2.2 Development History

The development of MD simulation could be traced back to the 1950s, when scientists began using computers to simulate molecular motion. With the rapid development of computer technology and the multi-body potential functions method, MD simulation technology has also developed rapidly and has become an important research tool [48]. Table 2-2 shows the development history of MD simulation methods.

Table 2-2. Development history of MD simulation methods. [48]

Time	Researchers	Progress
1957	Alder et al.	Molecular dynamics simulations were first reported by studying the aggregation of hard spheres.
1959	Alder et al.	The molecular dynamics simulation of real material models has been reported for the first time, which simulates the radiation hazards of cobalt crystals.
1964	Ralman et al.	The molecular dynamics simulation of real fluid argon was first reported, using the Lennard-Jones potential function to represent the interaction between atoms.
1972	Less et al.	The method is developed and extended to nonequilibrium systems with a velocity gradient.
1980	Andersen et al.	Created a constant pressure molecular dynamics method.

1983	Gillan et al.	The method was extended to non-equilibrium systems with temperature gradients, thus forming a non-equilibrium molecular dynamics method system.
1984	Nose et al.	Completed the creation of a constant temperature molecular dynamics method.
1985	Car et al.	A first-principles molecular dynamics method was proposed to unify electron theory with molecular dynamics methods organically.
1991	Cagin and Pettit	Furthermore, the Grand canonical ensemble molecular dynamics method is proposed.

2.2.3 Basic principles

In MD simulation, we first establish a reasonable theoretical model, then solve the Newton's Equations of motion of all particles in the system by integration. Furthermore, the motion trajectories of each particle can be obtained, allowing for the calculation of thermodynamic quantities and other macroscopic properties of the system [49].

The total energy of the system is equal to the sum of kinetic energy (U_k) and potential energy (U_r), where potential energy includes intermolecular atomic interactions (U_{inter}) and intramolecular atomic interactions (U_{intra}).

$$U = U_k + U_r = \sum_{i=1}^{N} \frac{1}{2} m_i v_i^2 + U_r(r_1, r_2, \dots r_N) \tag{2-1}$$

$$U_r = U_{inter} + U_{intra} \tag{2-2}$$

According to Newton's Classical mechanics, the force on any atom i in the system is the gradient change of potential energy:

$$F_i = -\nabla_i U = -\left(i \frac{\partial}{\partial x_i} + j \frac{\partial}{\partial y_i} + k \frac{\partial}{\partial z_i} \right) U \tag{2-3}$$

According to Newton's laws of motion, the acceleration of atom i is:

$$a_i = \frac{F_i}{m_i} \tag{2-4}$$

By integrating and solving for time, it is possible to predict the new velocity and position of atom i after time t:

$$v_i = v_i^0 + a_i t \tag{2-5}$$

$$r_i = r_i^0 + v_i^0 t + \frac{1}{2} a_i t^2 \qquad (2\text{-}6)$$

where v is the velocity, r is the position, a is the acceleration, and r_i^0 is the current position of the particle. When the initial velocity and position of the atom are known, the position, velocity, and acceleration of all particles in the system can be obtained at any time using the above equation.

The mentioned above is the theoretical basis for solving the energy, force, and displacement parameters of all particles in the system through MD simulation methods. Moreover, in MD simulation, the common integration algorithms for solving Newton's Equations of motion mainly include the Verlet algorithm and its improved Leap-frog algorithm, the Velocity Verlet algorithm, and the Predictor corrector method [48]. Their advantages and disadvantages are shown in Table 2-3. Among them, the Velocity Verlet algorithm is widely used due to its high computational accuracy and moderate computational complexity, and performed in this work.

Table 2-3. Advantages and disadvantages of common integration algorithms. [48]

Integral algorithm	Advantages	Disadvantages
Verlet algorithm	Simple in form and easy to program; The calculation accuracy of coordinate positions is high, reaching fourth order; Calculate the force only once per integration; Time is reversible.	The calculation accuracy of speed is relatively low, which is second-order; The obtained motion trajectory is independent of speed and cannot be coupled with a hot bat.
Leap-frog algorithm	The calculation accuracy of coordinate position and velocity has been improved, both of which are fourth order; The trajectory of particles is related to velocity and can be coupled with a hot bath.	The calculation of position and velocity is not synchronized, and kinetic energy and potential energy cannot be calculated separately based on velocity and position at the same time; The calculation time cost is higher than the Verlet algorithm.
Velocity Verlet algorithm	The calculation accuracy of coordinate position and velocity is superior to the Verlet algorithm; It also overcomes the disadvantage of asynchronous computation in the Leap-frog	The computational complexity is higher than the Verlet algorithm and Leap-frog algorithm.

	algorithm; Moderate computational complexity, currently widely used.	
Predictor-corrector method	Combining the advantages of the first two algorithms, Numerical stability and energy conservation performance are improved.	Higher computational complexity, which consumes a large amount of computer memory during the calculation process, is not suitable for simulating large-scale systems.

2.2.4 Calculation process

As shown in Figure 2-6, the calculation process of MD simulation is as follows:

(1) Setting the initial position and velocity of atoms in the system: For geotechnical materials, the spatial coordinates of the atoms contained in the material can generally be obtained through X-ray diffraction tests to determine the initial position of the atoms. At the same time, the initial velocity of the atoms in the system is also set.

(2) Calculate the potential energy and interaction forces between atoms: Defining the atomic force field in the structure by defining the interaction potential function between atoms, and calculating the potential energy of the atoms. Then, the force acting on each atom through the partial derivative of the potential energy to the coordinates were obtained.

(3) Numerical integration is performed on Newton's Equations of motion to calculate the new position and velocity of each particle: since the mass of each atom is known, the acceleration of each atom in the structure can be obtained by using Newton's second law. By selecting an appropriate time step (usually $1 fs = 10^{-15} s$), integrating the acceleration to obtain the velocity of each atom, and then integrating the velocity to obtain the displacement of each atom, a new structure configuration could be obtained. The potential energy of each atom in this configuration was recalculated.

(4) Repeat steps 2 and 3, iterating for enough time to achieve balance in the system.

(5) Analyze trajectory results to obtain system information.
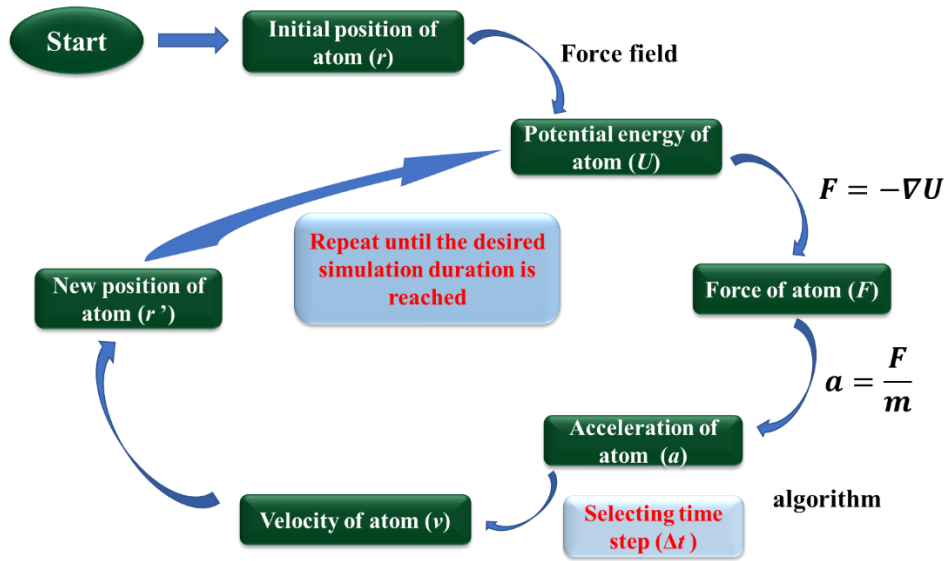
Figure 2-6. Molecular dynamics calculation flow chart

2.2.5 Introduction to the ensemble

Statistical mechanics is an essential tool to calculate the macroscopic properties of systems through its microscopic physical states (such as kinetic energy and potential energy). In statistical mechanics, according to different physical and chemical conditions, various ensembles are constructed to describe the microscopic state of system, and the required physical quantities are calculated by ensemble averaging. Moreover, the ensemble refers to the collection of all microscopic states corresponding to a macroscopic state of a system. The commonly used ensemble includes the following categories: Microcanonical ensemble (NVE), Canonical ensemble (NVT), Isothermal–isobaric ensemble (NPT), Grand canonical ensemble (μVT), Equienthalpy isobaric ensemble (NHP), etc.

The NVE, NVT, and NPT ensembles were used in this thesis, where the temperature and pressure of system were controlled under different methods. The commonly used methods for controlling temperature include direct speed calibration, Berendsen, Nose-Hoover, and Langevin hot bath temperature control. The main methods for controlling pressure include Anderson, Berendsen, and Parrinello Rahman constant pressure method [50].

2.2.6 Boundary Conditions

Due to the limited simulation ability of molecular dynamics, it is not possible to simulate a large number of particles (systems with millions of atoms), and can only simulate a specific number of particle systems in a limited space. Therefore, the concept of boundary conditions [51] was proposed to solve this problem, which can be divided into periodic boundary conditions and non-periodic boundary conditions. Periodic boundary conditions could make the simulation system become an infinite molecular system with the same properties, allowing the use of a relatively small number of particles to simulate the macro system. Non-periodic boundary conditions are applicable to non-uniform systems, where external particles cannot exchange matter and energy with the system at the boundary.

As shown in Figure 2-7, the periodic minimum image refers to the central box in the figure representing the simulated system, and the surrounding boxes have the same arrangement and motion as the simulated system. When the system is under periodic boundary conditions, if any particle moves out of the box, one particle must move in from the opposite direction. Thus, the number of particles in the system remains constant.

The closest periodic image method is usually used, when calculating the intermolecular forces in a system. It is assumed that there are N particles in the original cell. In the repeated molecular dynamics original cell, each particle only interacts with the other N-1 particles or the closest minimum image particles in the original cell. When using the closest periodic image method, the truncation radius (r_c) method is usually used to calculate the remote forces of system. In MD simulation, if the distance between molecules is greater than the truncation radius, their interaction force is considered as zero, and the truncation radius is generally around 10 Å. In addition, the maximum truncation radius cannot exceed half of the box edge length (L), that is, $r_c \leqslant L/2$.
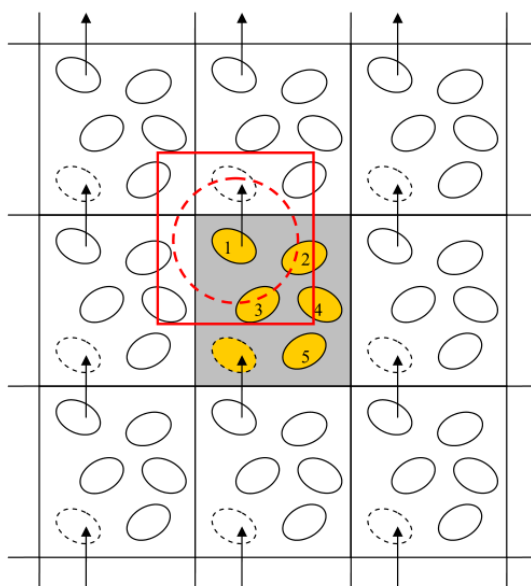
Figure 2-7. Schematic diagram of periodic boundary conditions in two-dimensional direction, where the dashed circle represents a potential cutoff. [42]

2.2.7 Introduction of Force Field

In MD simulation, we need to provide initial atomic positions and force field parameters for the interaction potential function of the system. Force field is a mathematical model that describes the interaction forces between atoms in molecules. It is one of the most fundamental parts of computational molecular dynamics simulation and the key to simulating materials using MD methods. The force field could quantitatively describe the bond energy, bond angle energy, dihedral angle energy, van der Waals interaction, coulomb electrostatic interaction, etc., between atoms in molecules. The interaction between the microscopic particles of the system is calculated through the force field, where the force field parameters are derived from the empirical fitting of many crystallography, thermodynamics, spectroscopy, and other experimental data or accurate quantum chemistry calculations.

Since the 1970s, a series of force fields applicable to organic molecules (e.g. protein, nucleic acid, sugar), inorganic materials (e.g., metal, metal oxide, clay), and polymer systems have been developed, such as the common AMBER, CHARMM, CVFF, COMPASS, CLAYFF, OPLS, and other force fields [48].

(a) bond stretching model

$$U_{\text{bond}} = \sum_{bonds} \frac{1}{2} k_b (r - r_0)^2$$

(b) bond angle bending model

$$U_{angle} = \sum_{angles} \frac{1}{2} k_a (\theta - \theta_0)^2$$

Bond interaction

(c) dihedral angle twisting model

$$U_{dihedral} = \sum_{dihedral} \frac{1}{2} \left[V_1[1 + \cos\varphi] + V_2[1 - \cos 2\varphi] + V_3[1 + \cos 3\varphi] \right]$$

(d) off plane bending vibration model

$$U_{\text{torsion}} = \sum_{torsion} \frac{1}{2} k_\chi (\chi - \chi_0)^2$$

Non-bond interaction

$$U_{non-bonding} = \sum_{j=1}^{N-1} \sum_{i=j+1}^{N} \left\{ 4\epsilon_{i,j} \left[\left(\frac{\sigma_{ij}}{r_{ij}} \right)^{12} - \left(\frac{\sigma_{ij}}{r_{ij}} \right)^6 \right] + \frac{q_i q_j}{4\pi\epsilon_0 r_{ij}} \right\}$$

Van der Waals Interaction U_{VDM} + Coulomb electrostatic Interaction U_{Coulomb}

(e) Intramolecular and intermolecular non-bond model

Intramolecular atomic interactions

bond stretching potential

dihedral angle twisting potential

Intramolecular non-bond interaction

Coulomb electrostatic potential

Van der Waals potential

bond angle bending potential

off plane bending vibration potential

Intermolecular atomic interaction

Intermolecular non-bond interaction

Coulomb electrostatic potential

Van der Waals potential

(f) Intramolecular and intermolecular interactions

Figure 2-8. Molecular force field models: Models of intramolecular and intermolecular interactions.

Molecular force field models are divided into intramolecular and intermolecular interaction models. As shown in Figure 2-8, intramolecular interaction models mainly include bond stretching model, bond angle bending model, dihedral angle twisting model, off plane bending vibration model, and intramolecular non-bond interaction model. Among them, the intramolecular non-bond interaction model refers to the non-bond interaction between two

atoms connected by non-bond in the same molecule (including coulomb electrostatic and van der Waals interaction), such as the interaction between atoms 2 and 5 in molecule A.

In addition, as shown in Figure 2-8(e), the intermolecular interaction model refers to the non-bond interaction of two atoms between different molecules, which also consists of coulomb electrostatic and van der Waals interaction, such as the interaction between atom 5 in molecule A and atom 6 in molecule B [40].

2.2.7.1 CLAYFF force field

The molecular structure of clay minerals is mainly composed of silica tetrahedron, aluminum oxide octahedron, and unique isomorphic substitution, adsorption of counter ions and water molecules. Due to the complex molecular interaction, the common force field could not reasonably describe the mechanical behavior of clay mineral crystal materials. In 1989, Skipper et al. first used MCY and QPEN two different force fields for clay minerals. In 1994, Kumagai proposed another CFF force field that could simulate aluminum silicate. In 1997, Teppen et al. optimized this force field to better describe the structural characteristics of various clay mineral. In 2004, Cygan et al. developed the CLAYFF force field applicable to geotechnical materials through first principles [52].

Since the CLAYFF force field was first proposed in 2004, it has been successfully applied to calculate the characteristics of rock fractures, interface adsorption, pore oil hydrocarbon transport, carbon storage, etc., especially the interaction between clay mineral base surface and multi-media, such as the structure and dynamic analysis of interlayer water and cations, organic intercalation modification, etc. Currently, this force field has been cited thousands of times. The CLAYFF force field in MD simulation is widely used to understand the structure, dynamics, and thermodynamics of clay, reveal the expansion phenomenon and adsorption characteristics of montmorillonite crystals, as well as accurately describe the structure and dynamics process of surfactants on clay mineral surface [53]. Many of the simulation results above are consistent with many experimental results.

The CLAYFF force field [52] has been widely used for clay minerals in MD simulation [14, 15, 54, 55], so it was employed in this doctoral thesis. The potential parameters of the CLAYFF force

field are shown in Table 2-4 and Table 2-5, where the total potential energy (E_{total}) of the entire system could be calculated using eq. (2-7).

$$E_{total} = E_{bond\ stretch} + E_{angle\ bend} + E_{Coulomb} + E_{VDW} \tag{2-7}$$

$$E_{bond\ stretch} = k_1 \left(r_{ij} - r_0 \right)^2 \tag{2-8}$$

$$E_{angle\ stretch} = k_2 \left(\theta_{ijk} - \theta_0 \right)^2 \tag{2-9}$$

The bond stretching potential energy ($E_{bond\ stretch}$) and the bond angle bending potential energy ($E_{angle\ stretch}$) could be obtained by eq. (2-8) and (2-9), where k_1 and k_2 are the elastic constants in bond stretching and bond angle bending, respectively; r_0 and r_{ij} are the equilibrium bond length and atomic distance between atoms i and j, respectively; θ_{ijk} is the bond angle value constructed by atoms i, j, and k, θ_0 is the equilibrium bond angle.

$$E_{VDW} = 4\varepsilon_{ij} \left[\left(\frac{\sigma_{ij}}{r_{ij}} \right)^{12} - \left(\frac{\sigma_{ij}}{r_{ij}} \right)^{6} \right] \tag{2-10}$$

$$E_{Coulomb} = \frac{e^2 q_i q_j}{4\pi\varepsilon_0 r_{ij}} \tag{2-11}$$

The Lennard-Jones potential/van der Waals potential energy (E_{VDW}) and coulomb electrostatic potential energy ($E_{Coulomb}$) could be obtained from the above equation, where σ is the distance when the Lennard-Jones potential is zero, ε is the depth of the potential; q_i and q_j is the charge of atoms i and j, respectively. e is the elementary charge, and ε_0 is the vacuum dielectric constant. Moreover, the interaction between different atoms σ_{ij} and ε_{ij} can be obtained through the Mixing Lorentz-Berthelot's law [48], as shown in eq. (2-12) and (2-13).

$$\sigma_{ij} = \frac{\sigma_i + \sigma_j}{2} \tag{2-12}$$

$$\varepsilon_{ij} = \sqrt{\varepsilon_i \varepsilon_j} \tag{2-13}$$

Table 2-4. Parameters of non-bond items in CLAYFF force field [52, 53]

Species	symbol	Charge (e)	ε (kcal/mol)	σ (Å)	Ref.
water hydrogen (SPC/E)	h*	0.4238			a
water oxygen (SPC/E)	o*	-0.8476	0.1554	3.1655	a
hydroxyl hydrogen	ho	0.425			b
hydroxyl oxygen	oh	-0.95	0.1554	3.1655	b
bridging oxygen	ob	-1.05	0.1554	3.1655	b
bridging oxygen with octahedral substitution	obos	-1.1808	0.1554	3.1655	b
bridging oxygen with tetrahedral substitution	obts	-1.1688	0.1554	3.1655	b
hydroxyl oxygen with substitution	ohs	-1.0808	0.1554	3.1655	b
tetrahedral silicon	st	2.1	1.8405×10^{-6}	3.3020	b
octahedral aluminum	ao	1.575	1.3298×10^{-6}	4.2713	b
tetrahedral aluminum	at	1.575	1.8405×10^{-6}	3.3020	b
octahedral magnesium	mgo	1.36	9.0298×10^{-7}	5.2643	b
aqueous sodium ion	Na	1	0.1301	2.35	c

Reference: a:[56]; b:[52]; c:[57].

Table 2-5. Bond and angle parameters in CLAYFF force field [53]

Harmonic bond stretch			k_1 (kcal/mol-Å^2)	r_o (Å)	
	species i	species j			
SPC or SPC/E	o*	h*	554.1349	1.0	
	oh	ho	554.1349	1.0	
	ohs	ho	554.1349	1.0	
Harmonic bond-angle bend			k_2 (kcal/mol-rad^2)	θ_o (deg)	
	species i	species j	species k		
SPC	h*	o*	h*	45.7696	109.47
SPC/E	h*	o*	h*	45.7696	109.47
Morse bond stretch			D_o	a	r_o
	species i	species j	(kcal/mol)	(Å^{-1})	(Å)
dioctahedral	oh	ho	132.2	2.182	0.945
trioctahedral	oh	ho	132.2	2.135	0.9572
M-O-H harmonic bond-angle bend			k_2 (kcal/mol-rad^2)	θ_o (deg)	
	species i	species j	species k		
	st	oh	ho	15	100

| bulk	ao	oh	ho	15	116
surface	ao	oh	ho	15	110
bulk	mgo	oh	ho	6	120
surface	mgo	ohs	ho	6	110

2.2.7.2 Water molecular force field

The number, position, and quantity of charge points vary among different water molecule models, as well as the number, position, and force field parameters of van der Waals force points. Most water molecule models are composed of three to six force points, where the four force point water model (such as TIP4P/ICE, TIP4P/2005, etc.) is an extension of the traditional three force point water model (such as SPC, SPC/E, TIP3P, etc.) through adding a massless, oxygen atom dependent charge and placing it at an additional position M (see Figure 2-9). The distance between this position M and oxygen along the angle bisector of the HOH bond angle is fixed. The water molecule models used in this work contain SPC, SPC/E, and TIP4P/ICE, and their potential parameters are shown in Table 2-6.

Table 2-6. Force field and potential parameters of some common water molecules.

Model	ε (kcal/mol)	σ (Å)	d_{OH} (Å)	d_{OM} (Å)	q_O	q_H	$\theta_{H\text{-}O\text{-}H}$	Ref.
SPC	0.1554	3.1656	1		-0.82	0.41	109.47	a
SPC/E	0.1554	3.1656	1		-0.8476	0.4238	109.47	b
TIP4P/ICE	0.2108	3.1668	0.9572	0.1577	-1.1794	0.5897	104.52	c
TIP4P/2005	0.1852	3.1589	0.9572	0.1546	-1.1128	0.5564	104.52	d

a:[58]; b: [56] ; c: [59]; d:[60].
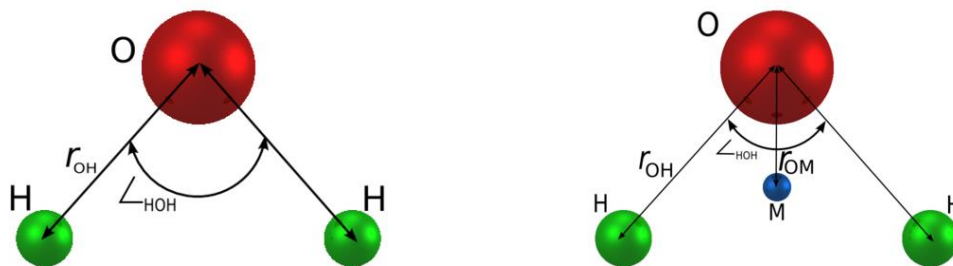
(a) three force point (e.g. SPC, SPC/E)   (b) four force point (e.g. TIP4P/ICE, TIP4P/2005)
Figure 2-9. Force points and distribution of water molecular models. [61]

2.3 Data analysis

2.3.1 Friction load, friction coefficient, and potential mean force (PMF)

The friction load (f) or pulling force is equal to the force of the virtual spring (F_{spring}), which could be obtained through eq. (2-14). Furthermore, Wei et al. [14] verified that the stiffness coefficient (K) of the virtual spring did not affect the result of friction load in MD simulation. Thus, to ensure reliability and save computing resources, the stiffness coefficient of 100 N/m of the virtual spring was also applied in this work.

$$f = F_{spring} = K(R - R_0) \tag{2-14}$$

where f is the friction load, F_{spring} is the force of all atoms in the group. $(R - R_0)$ is the spring elongation, and K is the stiffness coefficient of the virtual spring[50].

The friction coefficient (μ) can be obtained via the following equations:

$$f = \mu F_n + F_0 \tag{2-15}$$

$$\tau = \mu \sigma_n + c, \ \mu = tan\varphi \tag{2-16}$$

where f, μ, F_n, and F_0 are the friction load, friction coefficient, applied normal force, and offset friction load when $F_n = 0$, respectively. The shear load (τ) and normal load (σ_n) are obtained from f and F_n divided by the shear area of the system, and c and φ are the cohesion and friction angle, respectively.

The potential energy (U_{spring}) and the work (W) of virtual spring could be calculated by the following equations.

$$U_{spring} = \frac{1}{2} K[vt - (\vec{r_t} - \vec{r_0}) \cdot \vec{n}]^2 \tag{2-17}$$

$$W = \int_{r_0}^{r_f} \nabla U_{spring} \cdot d\vec{r} \tag{2-18}$$

where v, t, n are the pulling velocity of spring, pulling time, and pulling direction, respectively. Moreover, r_t and r_o are the positions of the slider centroid (i.e., the upper boundary layer in this work) in the current or initial state, respectively. r_f is the final position of slider centroid.

The potential mean force (PMF)[62] is used to describe the changing of free energy, and calculated by Jarzynski's equation as following:

$$\text{PMF} = \Delta F = -k_B T \, ln\left(\overline{e^{-\frac{W}{k_B T}}}\right) \tag{2-19}$$

where ΔF, W, k_B, and T are the Helmholtz free energy difference between the initial and final configurations, work of spring, Boltzmann constant, and temperature of system, respectively.

2.3.2 Radial distribution function (RDF) and coordination number (CN)

The radial distribution function (RDF) obtained by eq. (2-18) is often employed to calculate and represent the distance between different particles to reflect their interaction relationship[63]. The RDF could be also used to analyze and distinguish the crystals, liquids, and gases, such as a long-range ordered structure for crystals, a short-range ordered and long-range disordered structure for liquids, and no apparent structure for gases.

Moreover, the coordination number (CN_{ij}) could quantitatively describe the numbers of atoms of surrounding atom j around central atom i, which is calculated by integrating the RDF curves from the origin to the position of the first valley based on eq. (2-19).

$$g(r)_{ij} = \frac{n(r)_j}{\rho_j V} \approx \frac{n(r)_j}{4\pi\rho_j r^2 \Delta r} \tag{2-20}$$

$$CN_{ij} = 4\pi\rho_j r^2 \int_0^{r_{ij}} g(r) r^2 dr \tag{2-21}$$

where $n(r)_j$ is the average number of atom j around atom i in a shell with radius r to $(r + \Delta r)$, ρ_j is the number density of atom j, r is the distance between atom i and j.

2.3.3 Order parameter F_3

The order parameter F_3 is a three-body structural parameter to investigate the properties of dissociated water, proposed by Baez and Clancy [64]. The F_3 is used to measure the tetrahedral arrangement of an oxygen atom's n neighbors, and is calculated by equation (2-20), where the equilibrium angle was set as 104.52°, as determined in TIP4P/ICE water model.

$$F_3 = \langle (cos\ \varphi_{jik}\ |cos\ \varphi_{jik}|\ +\ cos^2\ (104.52°))^2 \rangle \tag{2-22}$$

where φ_{jik} is the angle between a water oxygen (i) and two oxygens (j and k) in its neighbor shell. F_3 is equal to zero for perfect tetrahedrally coordinated oxygens, such as ice, and 0.1 for liquid water.

2.3.4 Mean square displacement (MSD) and diffusion coefficient (D_s)

The mean square displacement (MSD, m^2/s) and diffusion coefficient (D_s) were given by the following equations.

$$MSD(t) = R^2(t) = \frac{1}{N} \sum_{i=1}^{N} (r_i(t) - r_i(0))^2 \tag{2-23}$$

$$D_s = \frac{MSD(t)}{2d \times t} \tag{2-24}$$

where d represents the simulation dimension, which is equal to 3 in three-dimensional space, such as the overall diffusion coefficient; and equal to 1 in one-dimensional space, such as diffusion coefficient along the x-, y-, and z-direction.

2.3.5 Work of adhesion (W_{AB})

The work of adhesion (W_{AB}) [65] is defined as a work required to separate two phases from each other, either liquid-liquid or liquid-solid interface (Figure 2-10). In this work, the work of adhesion between the water-ice system and montmorillonite surface was calculated according to the following equation:

$$W_{AB} = \frac{(E_{water-ice}\ +\ E_{Mt}) - E_{Mt-water-ice}}{2A} \tag{2-25}$$

where $E_{Mt-water-ice}$, E_{Mt}, and $E_{water-ice}$ are the total energy of the whole Mt-water-ice system (Figure 2-10(a)), bulk montmorillonite system (Figure 2-10(b)), and water-ice system (Figure 2-10(c)), respectively. Moreover, A is the contact area between montmorillonite and water-ice system (Figure 2-10(a)).
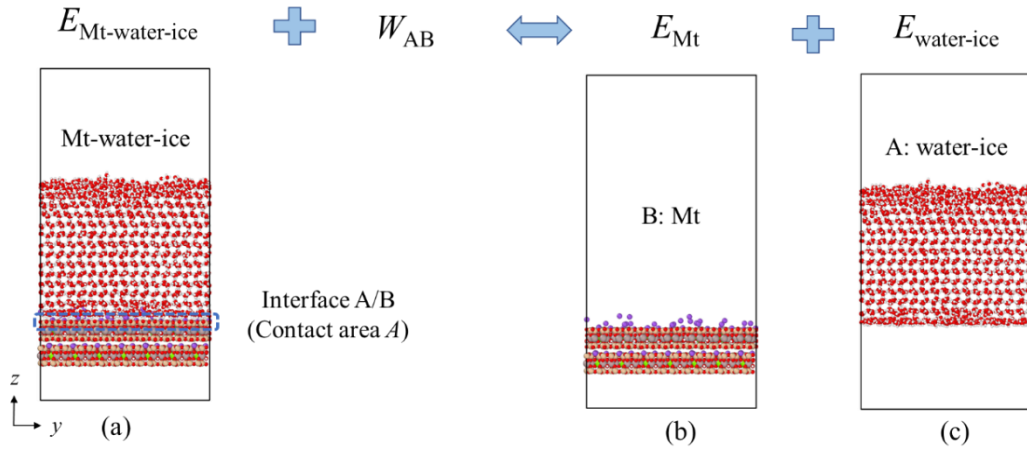
Figure 2-10. Structure diagram of (a) montmorillonite-water-ice, (b) montmorillonite, and (c) water-ice system.

2.3.6 Chill+ algorithm

Nguyen and Molinero [66] proposed Chill+ algorithm, which could identify the structure of ice (containing cubic, hexagonal, and interfacial ice), clathrate (containing hydrate and interfacial hydrate), and liquid water using the number of staggered and eclipsed bonds in the target system, as shown in Table 2-7.

As shown in Figure 2-11, the hexagonal and cubic ice could form and exist spontaneously in nature, and they had different crystal structure, stacking sequence, length of hydrated bond, density, and form conditions, where the hexagonal ice was stable ice, and cubic ice was metastable ice[67].

Figure 2-11. A dislocation mechanism for the reversible transformation between hexagonal Ice I_h and cubic Ice I_c. Balls and sticks show the oxygen atoms and the hydrogen bonds, respectively: (a) and (c) for the Ice I_h structure projected on a pris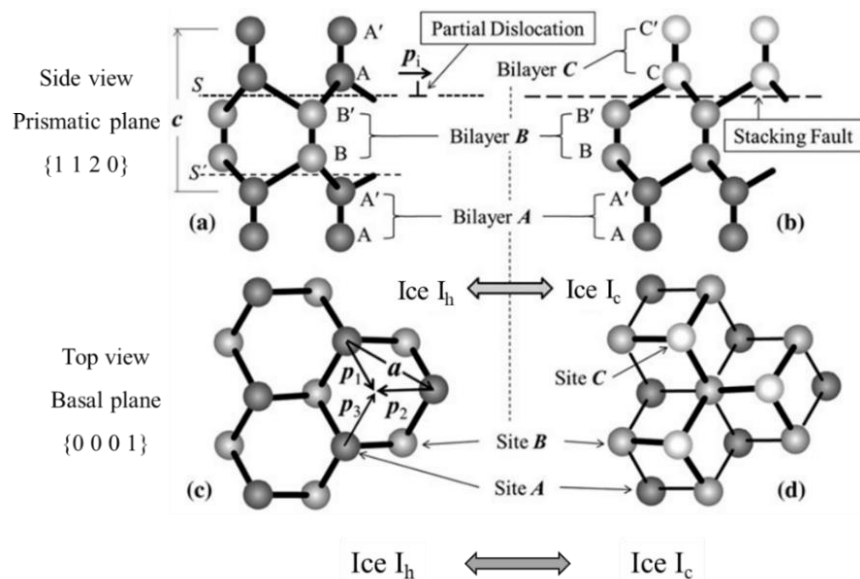matic plane {1 1 2 0} and on a basal plane, respectively, and (b) and (d) for the corresponding projections of the Ice I_c structure. Bimolecular layers A-A', B-B', and C-C' are simply designated bilayers *A*, *B* and *C*, respectively. Reversible transformation between Ice I_h and Ice I_c can be made by glide motion of a partial dislocation with a Burgers vector p_i (i = 1, 2 or 3) along the basal slip plane S between the bilayers *A* and *B.* The bilayer *A* turns into a new bilayer *C* by this glide motion, transforming Ice I_h to Ice I_c, and vice versa for the transformation from Ice I_c to Ice I_h [68].

Table 2-7. Identification of Ice, Clathrate, and Liquid in CHILL+ Using the Number of Staggered and Eclipsed Bonds. [66]

Structure	Eclipsed bonds	Staggered bonds	Neigh. a
Hexagonal ice	1	3	4
Cubic ice	0	4	4
Interfacial ice	2 or 1	2 or 3	4
Hydrate	4	0	4
Interfacial hydrate	3	any	4
Liquid water	N/A	N/A	any

Note: a Number of water neighbors within 3.5 Å (first coordination shell).

Chapter 3

Effect of water on the frictional and mechanical behavior of montmorillonite: a MD study

Chapter 3. Effect of water on the frictional and mechanical behavior of montmorillonite: a MD study [I]

Abstract

The interparticle friction behavior of clay plays an essential role in controlling its mechanical properties, but remains unclear in nanoscale. As one of the major clay particles, the nanoscale friction properties of hydrated montmorillonite have been studied using steered molecular dynamics simulation (SMD) method, considering the coupling effect of water content of 0 ~ 30% and normal load of 1 atm ~ 10 GPa. The SMD has been performed to investigate the frictional mechanism of hydrated montmorillonite and its structural properties of interlayer water. The evolution of average friction load with water content, friction coefficients, and the distribution of interlayer water molecules were obtained. Furthermore, the SMD pulling along z-direction was conducted to study the effect of interlayer water molecules on the interaction between montmorillonite layers. All simulation results showed that more energy and a higher friction load were required to slide at a higher normal load. The friction coefficient of 0.058 ~ 0.17 for hydrated montmorillonite agreed well with the previous experimental and simulation results, showing its weak friction properties. The evolution of friction coefficient with water content was different at different normal loads, where the friction coefficient of 5% hydrated montmorillonite was the highest at 3 ~ 10 GPa. Moreover, the increasing normal load could promote the redistribution of interlayer water.

Keywords: Molecular Dynamics; Water content; Normal load; Montmorillonite; Nanoscale friction.

[I] This chapter is based on the following paper: Wei, P., Zheng, Y., Zaoui, A. Effect of water on the frictional and mechanical behavior of montmorillonite: a MD study, 2023. (Under review).

Other relevant work concerning about nanoscale friction of clay minerals:

Wei P., Zhang L., Zheng Y., Diao Q., Zhuang D., and Yin Z. Nanoscale friction characteristics of hydrated montmorillonites using molecular dynamics[J]. Applied Clay Science, 2021,210:106155.

Wei P., Zhou S., Zheng Y. et al. Nanoscale Stick-Slip Behavior and Hydration of Hydrated Illite Clay. Computers and Geotechnics, 2023. (In press)

3.1 Introduction

Montmorillonite, one of the widespread clay minerals, is the most prevalent 2:1 type clay, found in soils, sediments, and atmospheric particles as part of clay particles. It has not only a strong water sorption capacity, low permeability, and high expansibility, but also extremely weak friction coefficient [17-19]. Thus, montmorillonite was an important component that could significantly control the failure strength of soil samples [19]. Moreover, Sakuma et al. [20] reported that smectite could dramatically decrease the mechanical strength of crustal faults and may cause creep on natural faults without great earthquakes. For example, the abnormally large slip (50 ~ 80 m) of the 2011 Tohoku earthquake was due to the existence of montmorillonite in the fault zone [21, 22]. Therefore, the friction behavior of montmorillonite particles is very worth studying.

Some macroscopic experimental tests [19, 69-71] were used to study the friction properties of montmorillonite. It is observed that its friction coefficient could be significantly affected by different environmental factors, such as hydration state [19, 72], temperature [70], normal stress [69, 73], interlayer cation [71], sliding/shearing velocity [73], and clay content [74, 75]. Previous studies have advanced the knowledge of friction properties on montmorillonite-based soils in macroscale, but it is challenging to reveal some friction/shear mechanism between materials interfaces. Furthermore, in microscale, the nanoscale friction behavior of hydrated montmorillonite is still relatively less, and has gradually started to be studied recently [14, 20, 76]. The investigation at the atomistic level could give more information on the basic mechanisms of friction [23].

At the end of the 20th century, with the rapid development of nanoscience and technology, many mechanical phenomena and their mechanisms have developed from macroscale to nanoscale. Nano-tribology [77] has been well developed through theoretical, experimental, and simulation methods, such as atomic force microscopy [78], friction force microscopy test [79], optical microscope, scanning electron microscopy [80], and molecular dynamics (MD) simulation[14]. MD simulation method is an excellent tool to effectively study the friction mechanism in rotating carbon nanotube bearings [81], friction behavior between silica nanospheres [82], adhesion of epoxy-silica interface in the salt environment [83], etc. So far, in

nanoscale tribology, most previous studies have been performed on the nanoscale friction behavior of carbon [84], muscovite mica [78], nanocomposites [80], etc.

On the other hand, in recent years, the nanoscale friction of soil minerals has been gradually studied. For example, Leng and Cummings [85] investigated the shear dynamics of hydration layers of the thickness of $0.6 \sim 2.44$ nm confined between two mica surfaces via MD simulation. Xu et al. [86] studied the interfacial friction behavior of quartz under dry and wet states using MD simulation, concerning normal load, water lubrication, and surface orientation. The effects of normal load and sliding velocity on the nanoscale friction behavior of hydrated montmorillonite [14] and quartz-quartz/kaolinite interface [87] have been studied using MD simulation. Abbasi et al. [76] studied the nanoscale stick-slip behavior of hydrated Na-montmorillonite considering the effect of hydrostatic stress and interlayer water through MD simulation, and found that the stick-slip effect was related to the structures of interlayer water. Furthermore, some previous studies reported that the water content could significantly affect the friction strength [19, 88] and mechanical strength [15, 76] of montmorillonite. Tetsuka et al. [19] showed that the friction coefficient declined with increasing water content through the biaxial friction test. Sakuma et al. [20] found that the friction coefficient of dry montmorillonite increased with the ionic radius of interlayer cations using density-functional-theory (DFT) calculations and shear experiments, and also discussed the relationship between molecular friction and macroscale friction [89, 90], as well as they proposed a central question: what degree the interlayer water is stable to act as a lubricant at depth.

To sum up, some questions arose as follows: Does interlayer water in clay minerals play a role in lubrication or bonding? How much interlayer water is needed to stabilize the lubricant? Therefore, the effect of interlayer water molecules on the nanoscale friction mechanism of hydrated clay and its structural properties are still unclear. The nanoscale friction behavior of montmorillonite could help to understand the interaction and deformation mechanism between clay particles, and explain some friction phenomenon in macroscale, such as shear zone formation, slip mechanism, etc.

This study aimed to probe the nanoscale friction behavior of different hydrated montmorillonites using steered molecular dynamics (SMD) simulations. The frictional

mechanism of hydrated montmorillonite and its structural properties of interlayer water were investigated. The obtained friction coefficient in this work was compared with previous studies. Subsequently, the SMD pulling was performed to study the effect of interlayer water molecules on the interaction between montmorillonite layers.

3.2 Computational details

3.2.1 System setup and force field

The Wyoming-type montmorillonite model used here is derived from [91], and its structural formula of unit cell is $Na_{0.75}(Si_{7.75}Al_{0.25})(Al_{3.5}Mg_{0.5})O_{20}(OH)_4 \cdot nH_2O$. The hydrated montmorillonite with water content of 0%, 5%, 10%, 15%, 20%, 25%, and 30% weight percent (the ratio between water mass and solid mass) were established, respectively. Moreover, the rigid SPC/E water model [56] was used to describe the interactions among hydrated montmorillonite. As shown in Figure 3-1(a), the supercell of 10% hydrated montmorillonite obtained from [92] was composed of 128 unit cells ($8a \times 4b \times 4c$), and the simulation box dimensions is 41.44 Å × 35.92 Å × 77.58 Å. In this work, the interparticle friction behavior of hydrated montmorillonite tactoid with interlayer water in microscale (see Figure 3-2) was investigated, where the interlayer water between montmorillonite sheets (less than four water layers, around 12 Å) was usually referred to bound water in soil. Because [93] reported that the thickness of bound water in individual Na-montmorillonite sheet containing two water layers was determined as about 6 Å using MD simulation.

For steered molecular dynamics (SMD) friction along y-direction, it is noted that the vacuum along z-direction of 30 Å is set to avoid the interaction between the neighboring upper and lower boundary atoms of montmorillonite due to the periodicity of the z-direction (Figure 3-1(a)). On the other hand, for SMD pulling along z-direction, the vacuum along z-direction for all hydrated cases is 70 Å (Figure 3-1(c)). The vacuum along z-direction of 30 Å for SMD friction and 70 Å for SMD pulling are both set in other hydrated montmorillonite systems.

SMD simulation method was one of non-equilibrium molecular dynamics simulation, and its principle was based on Newton's laws of motion and the concept of force-induced structural changes. During SMD simulation, an external force or bias potential through a virtual spring

was continuously applied to selected atoms or groups of atoms in a system along a specific direction (e.g., x-/y-/z-direction, etc.), allowing the system to be driven along a desired reaction coordinate or pathway. Moreover, SMD method could allow to induce conformational changes in whole system and compute the potential of mean force (PMF) along the assumed reaction coordinate [50], so it was particularly useful for studying the response behavior of structural changes and mechanical properties caused by external forces. SMD method was different from the conventional MD simulation (namely equilibrium MD simulation), which was usually employed to investigate equilibrium properties and dynamics of systems at thermal equilibrium. At present, SMD method has been effectively used to investigate the friction mechanism of soil/rock minerals in microscale [14].

As shown in Figure 3-1(b), the whole simulation model contains three kinds of layers: Boundary, Thermostat, and Newtonian layers, which each contain different atoms. 1) The lower boundary layer was fixed in their position during the whole simulation. The upper boundary layer was set as independent rigid body (i.e., a single entity), which could transfer the external loads on the clay-water system. Moreover, for SMD friction along y-direction, uniform normal load and a controlled sliding velocity via a virtual spring were applied in the upper boundary layer (Figure 3-1(a)). On the other hand, for SMD pulling along z-direction, a controlled pulling velocity via a virtual spring along the z-direction was applied in the upper boundary layer (Figure 3-1(c)). 2) The thermostat layer was set as a temperature-controlled layer to keep the whole system at a target temperature, so it was performed by Langevin thermostat and micro-canonical (NVE) ensemble for this atoms group. 3) The Newtonian layer with NVE ensemble was free to move. The above simulation setting method was drawn from the method proposed in the literature [14, 94]. CLAYFF force field [52] used in this work, has been effectively applied to investigate the mechanical behavior of clay [15, 95] and the interatomic interaction of clay-water system [16, 55].
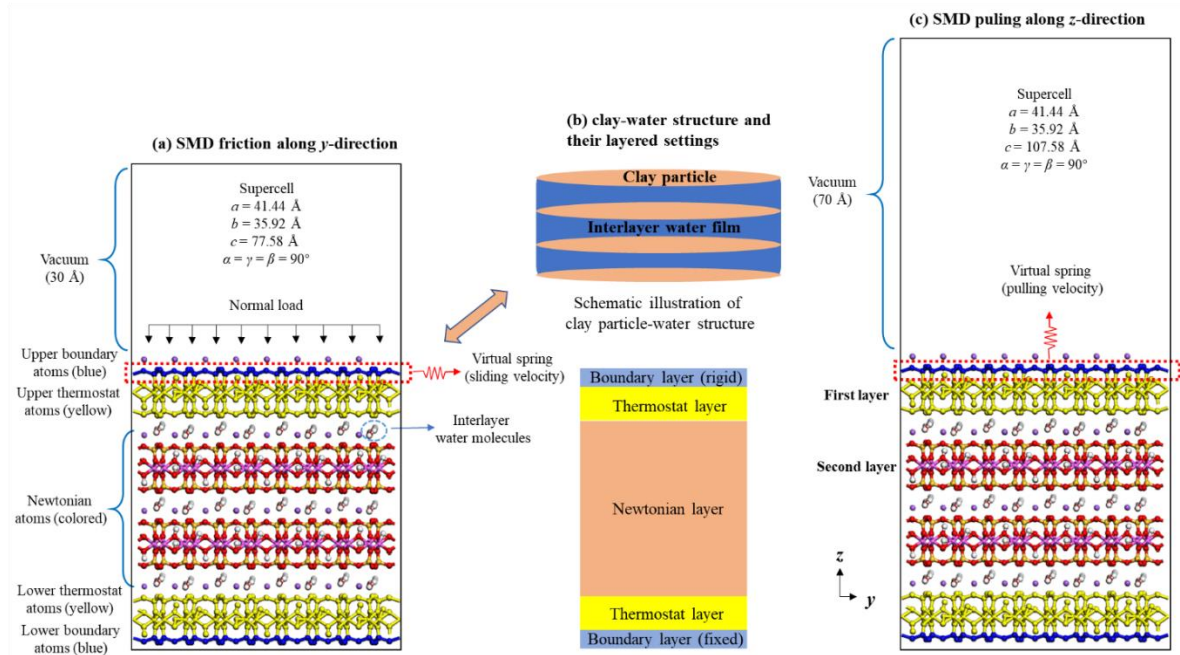
Figure 3-1. Hydrated montmorillonite model with water content of 10% used in this work: (a) steered molecular dynamics (SMD) friction along *y*-direction; (b) Schematic illustration of clay particle-water structure and their layered setting; (c) SMD pulling along *z*-direction. This model contains three kinds of atoms: boundary atoms, thermostat atoms, and Newtonian atoms, where (1) lower boundary atoms - rigid and fixed the position; (2) upper boundary atoms - rigid and upon applied a normal load and a controlled sliding velocity via a virtual spring along the *y*-direction for SMD friction, as well as rigid and a controlled pulling velocity via a virtual spring along the *z*-direction for SMD pulling; (3) thermostat atoms - temperature-controlled layers; (4) atoms - free to move.
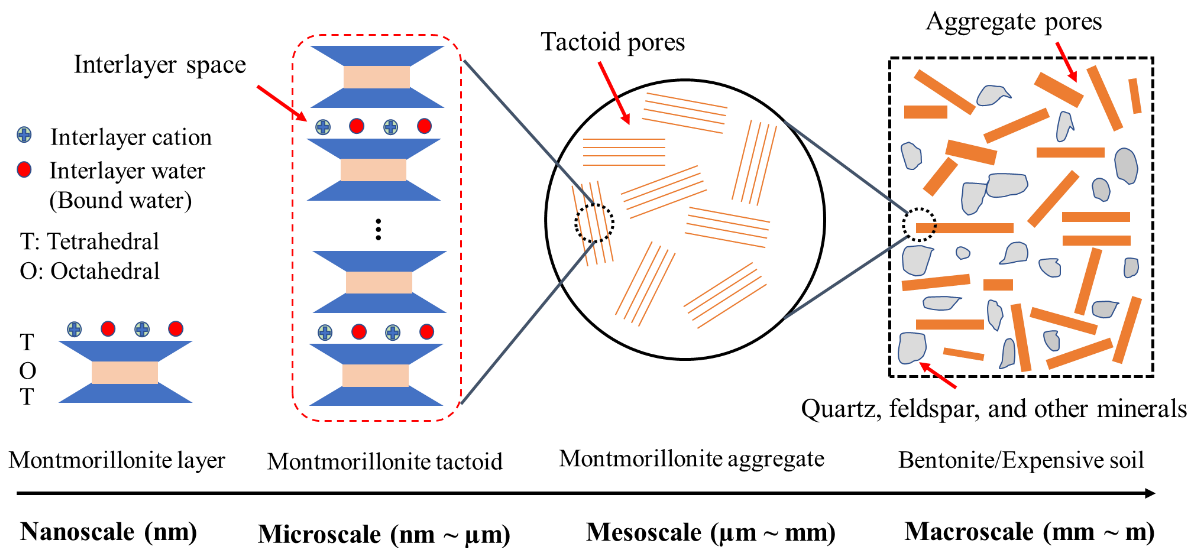

Figure 3-2. Schematic illustration of the multi-scale structure of bentonite or expensive soil. (This figure was revised from the reference [96])

3.2.2 Relaxation and simulation details

MD simulations were performed using LAMMPS code[50]. Three-dimensional periodic boundary conditions and the Verlet algorithm[97] for integrating motion equations, were applied in whole simulations. The cut-off radius for the van der Waals forces is 10 Å, and that for long-range electrostatic interactions using the Ewald sum method [98] is 8.5 Å. The time step is 1.0 fs in whole simulations.

As shown in Table 3-1, to obtain a sufficient equilibrium configuration of montmorillonite-water system, the MD simulation scheme contains the following steps. (1) Firstly, the energy minimization is applied to montmorillonite-water system using the conjugate gradient (CG) method. (2) The system was equilibrated with the micro-canonical (NVE) ensemble for 200 ps, followed by the canonical (NVT) ensemble for 200 ps, and then with the isothermal-isobaric (NPT) ensemble for 600 ps, respectively. The Nose-Hoover anisotropic thermostat and barostat were used to control the temperature and pressure, with a temperature of 300 K and pressure of 1.0 atm. (3) The system was further equilibrated with NVE ensemble for 400 ps, where the temperature of thermostat atoms (yellow) in this system was controlled at 300 K by Langevin thermostat[99], and the upper boundary atoms (blue) was applied by normal load of 1 atm. (4) The different normal loads of 1 atm ~ 10 GPa were applied to the upper boundary atoms (blue) for 200 ps with NVE ensemble. (5) Based on the above steps, as shown in Figure 3-1(a), the steered molecular dynamics (SMD) friction along the y-direction ([0 1 0] crystal orientation) was performed for 200 ps, where a controlled sliding velocity of 0.0005 Å/fs via a virtual spring along the y-direction was applied to the upper boundary atoms (blue), so that the sliding distance of about 100 Å was obtained. (6) Based on step 2, the systems were further equilibrated with NVT ensemble at 300 K for 100 ps. (7) Based on step 6, the SMD pulling along the z-direction ([0 0 1] crystal orientation) was conducted for 80 ps, as shown in Figure 3-1(b), where a controlled pulling velocity of 0.0005 Å/fs via a virtual spring along the z-direction was applied to the upper boundary atoms (blue), so that the pulling distance of about 40 Å was obtained.

It was worth noting that the normal load ranging from 1 atm to 10 GPa was applied to investigate the normal load dependence in this wok, it was due to the typical high loads usually

reaching several GPa in nanoscale research, such as friction force microscale (FFM) [100], nanoindentation experiment [101, 102], and MD studies [87, 103]. [103] and [100] reported that the macroscopic pressure/stress was calculated by dividing the load by the nominal contact area (containing uncountable asperities), but the sliding of single-asperity contact (ultra-small contact area) was employed in FFM and MD simulation, causing easily reaching GPa level. Moreover, [104] also proposed that the order of magnitude of mechanical strength of clay was much different between nanoscale (GPa level) and macroscale (MPa level), where the claystone in macroscale contains some complex pores, interfaces, and mineral phases at different scales, which could significantly weaken the mechanical strength of soil sample. However, at nanoscale, the crystal structure of clay minerals in MD simulation or soil sample in nanoindentation experiment was more perfect, and did not contain the pores and cracks. On the other hand, the friction behavior under natural conditions (e.g., temperature of 20 ~ 200 °C and external load of a few hundred MPa) was also worth considering in the future.

Table 3-1. MD simulations schemes for hydrated montmorillonite system.

Step	Equilibrium (Equi.) and steered molecular dynamics (SMD) process	
1	Minimize	conjugate gradient (CG) algorithm: the energy of 1.0e-6 kcal/mol, the force of 1.0e-8 kcal•(mol•Å)-1, and the maximum number of iteration steps of 1000.
2	Equi. 1	(a) NVE, 200 ps ~ (b) NVT (300 K), 200 ps ~ (c) NPT (300 K, 1 atm), 600 ps
3	Equi. 2 under normal load	NVE + Langevin (300 K) + normal load of 1 atm, 400 ps
4	Equi. 3 under normal load	NVE + Langevin (300 K) + different normal loads of 1 atm ~ 10 GPa, 200 ps
5	SMD friction along y-direction	NVE + Langevin (300 K) + different normal loads of 1 atm ~ 10 GPa, SMD friction along y-direction with sliding velocity of 0.0005 Å/fs, 200 ps (Total process: steps 1-2-3-4-5)
6	Equi. 4 without normal load	NVE + Langevin (300 K), 100 ps (Note: this step is based on step 2, not step 5)
7	SMD puling along z-direction	NVE + Langevin (300 K), SMD puling along z-direction with pulling velocity of 0.0005 Å/fs, 80 ps (Total process: steps 1-2-6-7)

3.2.3 Model verification

To verify the accuracy of the built model and applied force field, the basal spacing of different hydrated Na-montmorillonite in this MD work and previous studies are shown in Table 3-2, where the definition and partition of water layer (WL) corresponding to water content were drawn from previous research [105, 106]. As shown in Table 3-2, the basal spacing of hydrated Na-montmorillonite increases with the rising water content, and its value in this MD work agrees well with other previous simulations and experiment results. It could be verified that these built hydrated montmorillonite systems in this work were accurate.

Table 3-2. The basal spacing of different hydrated Na-montmorillonite. (uc: unit cell)

Water content (%)	water layer (WL)	Results in this work (Å)	Other simulation results (Å)	Experiments (Å)
0	0 WL	9.33	9.51 ~ 10.01[107, 108]	9.74[109]; 9.5[110]
5 (2 H_2O/uc)	1 WL	11.08	11.96[105]; 9.85[111]; 11.02 ~ 11.87[107]	11.61[109]
10 (4 H_2O/uc)	1 WL	11.84	12.08[112]; 12.32[113]; 12.3[114]; 12.2[107]; 12.0[111]; 12.65[115]; 12.16[16]; 12.36[105]	12.0 ~ 12.6[109, 116-118]; 12[119]
15 (6 H_2O/uc)	2 WL	12.76	13.44[105]; 13.64[111]; 12.52 ~ 13.14[107]	12.6 ~ 14.4[109]
20 (8 H_2O/uc)	2 WL	14.26	15.28[112]; 14.96[113]; 15.3[114]; 15.7[107]; 15.5[111]; 15.0[115]; 14.52[16]; 14.96[105]	14.92 ~ 15.42[109]; 15.6[116]; 15.5[118]; 15.55[110]; 15[119]
25 (10 H_2O/uc)	2 WL	15.15	15.98[105]; 15.4 ~ 16.35[107]	15.5[109]
30 (12 H_2O/uc)	3 WL	16.36	18.77[112]; 17.07[113]; 18.7[107]; 18.0[111]; 16.79[16]; 17.21[105]	15.56[109]; 15.8[120]; 18[119]

3.3 Results and discussions

Sections 3.3.1 and 3.3.2 present the results and discussions of SMD friction along the *y*-

direction, studying the frictional mechanism of hydrated montmorillonite and its structural properties of interlayer water. Section 3.3.3 shows SMD pulling along the *z*-direction, focusing on the effect of interlayer water molecules on the interaction between montmorillonite layers.

3.3.1 Effect of water content on frictional mechanism

Figure 3-3 shows the evolution of friction load and PMF with sliding distance for 5% hydrated montmorillonite under different normal loads. As shown in Figure 3-3, the "stick-slip" effect [121] of montmorillonite was found in all cases, showing the periodic crenelated wave phenomenon of friction load at the sliding process. The higher the normal load, the higher the friction load and its wave amplitude, showing that the higher the stick-slip effect, which was consistent with the nanoscale friction behavior of quartz-quartz/kaolinite interface [87]. Moreover, As shown in Figure 3-4, the PMF linearly increases with the sliding distance, and the slope of PMF-sliding distance curve rises with increasing normal load, indicating that more energy is required during sliding at a higher normal load.
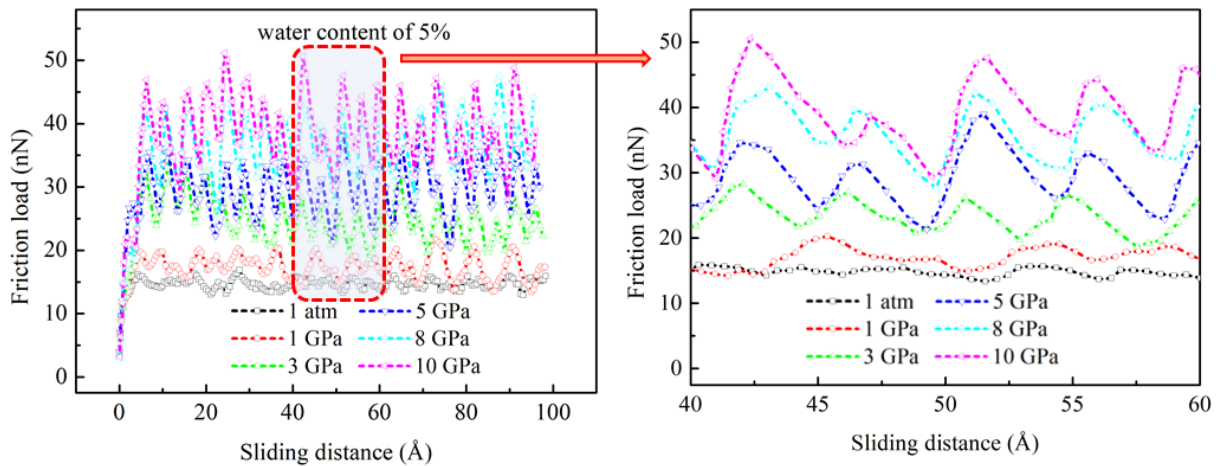

Figure 3-3. Evolution of friction load with sliding distance for 5% hydrated montmorillonite under different normal loads.
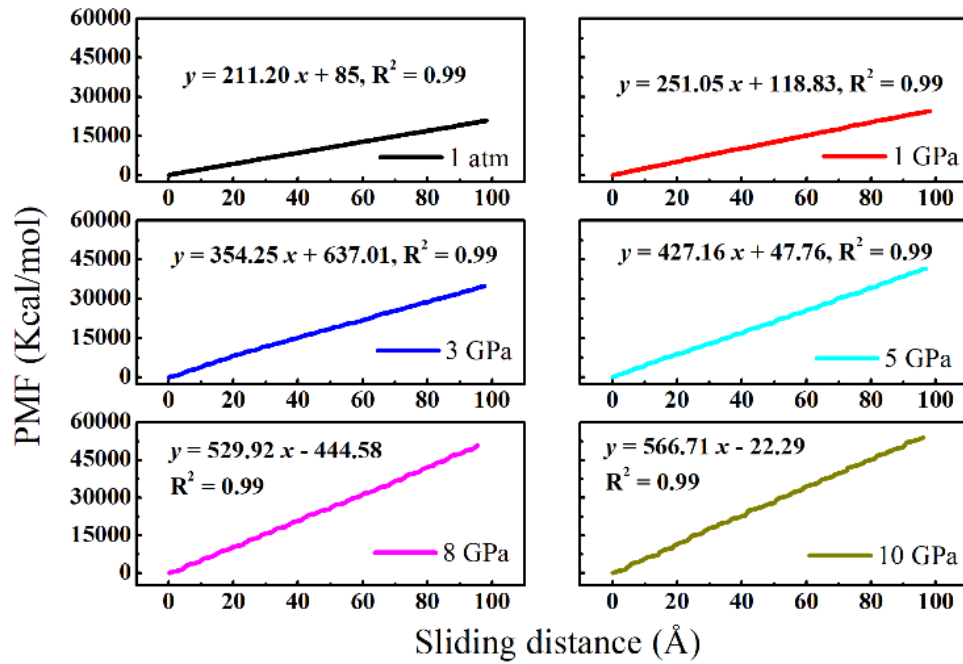
Figure 3-4. Evolution of Potential of mean force (PMF) with sliding distance for 5% hydrated montmorillonite under different normal loads.

Figure 3-5(a) shows the relationship of average friction load and water content under different normal loads, where the average friction load is equal to the mean value of friction load at sliding distance of latter 80 Å. At low normal load of 1 atm ~ 1 GPa, the average friction load decreased with the increasing water content of montmorillonite. However, at high normal load of 3 ~ 10 GPa, it is worth noting that two convex peaks are found in the average friction load-water content curve, corresponding to water content of 5% and 20%, where that of 5% is the greatest. This is a strange and interesting question: Does the interlayer water bond or lubricate at special condition? Sakuma et al. [20] also proposed that the interlayer water could act as a lubricant and reduce the shear strength of rock/soil, but a central question is: How much interlayer water is needed to stabilize the lubricant? Therefore, the friction mechanism of water content of 5% and 20% for hydrated montmorillonite were needed to be further investigated in the future.

On the other hand, the relationship between ultimate PMF and water content is shown in Figure 3-5(b), where the ultimate PMF is obtained from the maximum value of PMF at a sliding distance of 100 Å. The evolution of ultimate PMF with water content is similar to that of average friction load. It indicates that the normal load plays an important role in the friction

behavior of montmorillonite, especially at a high normal load.
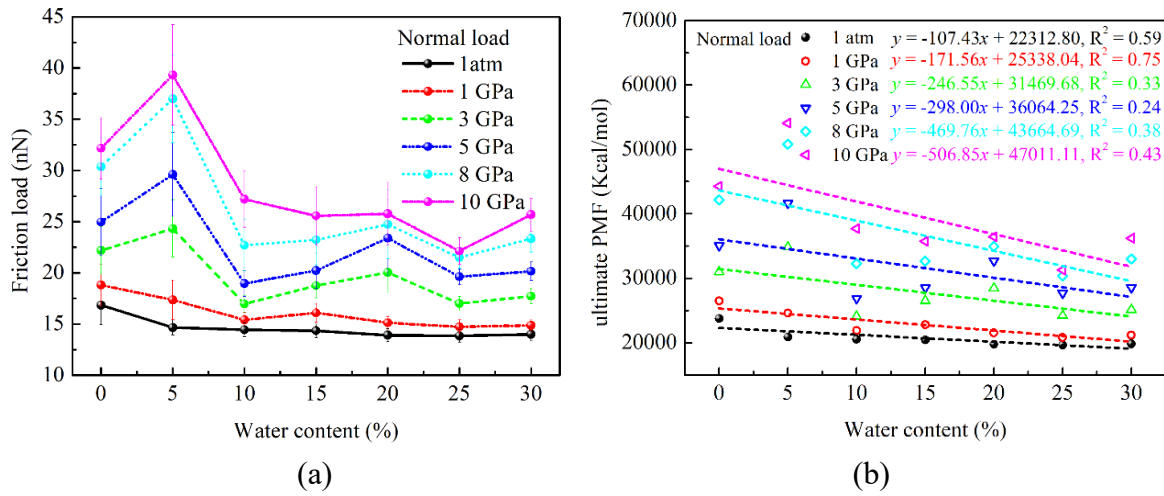
Figure 3-5. Evolution of (a) average friction load and (b) ultimate Potential of mean force (PMF) with water content for hydrated montmorillonite under different normal loads.
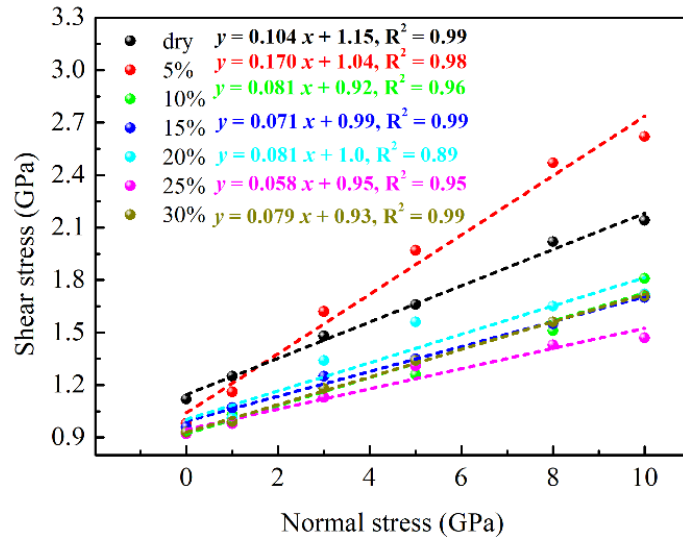
Figure 3-6. Relationship of shear stress and normal load and water content for different hydrated montmorillonites.

As shown in Figure 3-6, the linear relationship between shear stress and normal load for different hydrated montmorillonite is found, which is consistent with previous works, such as the friction properties of the montmorillonite using MD simulation [14], muscovite mica using AFM [78] and graphene films using means of angle-resolved photoemission spectroscopy [122]. Moreover, Li et al. [123] found the linear relationship between the static friction load and the

normal pressure through theoretical derivation based on Prandlt-Tomlinson's model [77].

Table 3-3 shows the evolution of friction coefficient with water content, and shear stress-normal load curve in Figure 3-6. As shown in Table 3-3, the friction coefficient of 5% hydrated montmorillonite is the highest, and then the dry case, followed by that of 10 ~ 30%. This evolution of friction coefficient with water content could be likely related to the structure and form of interlayer water, which will be discussed in the next section. Furthermore, Table 3-3 collects the friction coefficients of hydrated montmorillonite in this study and those of the previous experiments and simulations. For microscale, the friction coefficient value in this MD work are consistent within an order of magnitude with previous research from MD simulation [14, 76], DFT [90], and AFM [124], indicating the accuracy of this established model and force field. The low friction coefficient of 0.058 ~ 0.17 also illustrated the weak friction properties of montmorillonite [17-19]. On the other hand, [90] proposed that the friction coefficient in microscale could not be directly compared to that in macroscale, because the friction coefficient in microscale was obtained based on the true contact area, which was different from that in macroscale. In general, the friction coefficient of clay minerals in macroscale was greater than that in microscale [90], which was also found in this work, shown in Table 3-3.

Table 3-3. Friction coefficient of hydrated montmorillonite (Mt) at room temperature (300 K) compared to previous experimental and simulation results.

Materials	Method	Water content (%)	Friction coefficient	Internal friction angle (°)	Note	Scale
Hydrated Na-Mt	MD simulation	0 ~ 30	0.058 ~ 0.17	3.3 ~ 9.6	In this work, at the sliding velocity of 0.0005 Å/fs and normal loads (1 atm ~ 10 GPa), as well as room temperature.	Nano-/Micro- scale
Na-Mt [76]	MD simulation	10 ~ 40	0.058 (average)	3.3	At 300 K, normal stress of 5 ~ 12.5 GPa, and a constant shear strain rate of 2×10^9 s^{-1}.	
Hydrated Na-Mt [14]	MD simulation	A water film with	0.041 ~ 0.074	2.3 ~ 4.2	At 300 K, sliding velocity of 0.0001 ~ 0.005 Å/fs, as	

		260 water molecules			well as normal loads (1 atm ~ 25 GPa)	
Dry Mt [20]	DFT	0	0.22 (Na-Mt), 0.27 (K-Mt)	12.4 (Na-Mt), 15.1 (K-Mt)	-	
Pyrophyllite [90]	DFT	0	0.078	4.5	-	
Mica [124]	Atomic force microscopy/lateral force microscopy	0	~ 0.13	~ 7.4	At 20 °C, RH 50%	
Na-Mt [124]	Frictional sliding experiments	Dry and wet state	0.100 ~ 0.280 (saturated), 0.45 ~ 0.78 (dry)	5.7 ~ 15.6 (saturated), 24.2 ~ 38.0 (dry)	At room temperature and the range of normal stress 0 ~ 700 MPa	Macroscale
Ca-smectite [73]	double-dire shear test	~ 11%	0.150 ~ 0.320	8.5 ~ 17.7	At room temperature, room humidifies, and range of normal stress 5 ~ 45 MPa.	
Ca-Mt [88]	Biaxial stress experiments	1.6 ~ 20	0.02 ~ 0.41	1.1 ~ 22.3	At normal stresses 100 MPa and sliding velocities of 1–300 μm/s	
Na-Mt [19]	Biaxial friction testing	11 ± 1 ~ 93 ± 7	0.06 ~ 0.33	3.4 ~ 18.3	At room temperature and normal stress of 10 MPa.	
Brine-saturated Mt [20]	Triaxial shear experiments	Brine-saturated	0.13 (Na-Mt), 0.20 (K-Mt)	7.4 (Na-Mt), 11.3 (K-Mt)	At effective normal stress of 40 MPa.	

Table 3-4 displays the cohesion of hydrated montmorillonite in this work and previous work,

which could represent the shear resistance of clay minerals. As shown in Table 3-4, the cohesion of dehydrated montmorillonite was greater than that in other hydrated cases, indicating that the interlayer water could reduce the shear resistance of hydrated montmorillonite. On the other hand, combined with some previous research [14, 76], the sliding velocity could significantly affect the cohesion in MD study, where the cohesion could significantly increase with rising sliding velocity. Moreover, the cohesion of muscovite mica also could be affected by different sliding paths [89].

The cohesion plays a crucial role in determining the frictional properties and behavior of clay minerals. As shown in Figure 3-7, Duque-Redondo et al. [125] and Wei et al. [14] proposed that the cohesion between clay mineral sheets may have two origins: the electrostatic interactions between the charged clay mineral sheets and the interlaminar cations; as well as the hydrogen-bond network among water molecules and the clay mineral surface. The difference in the cohesion of hydrated montmorillonite between MD simulations and experimental studies arose from the inherent limitations, approximations, and scales of each approach. Moreover, experimental measurement of cohesion in hydrated montmorillonite was challenging, while the cohesion of hydrated montmorillonite in MD simulation referred to the cohesive forces between interlayer cation/water molecules and montmorillonite surface. On the other hand, Sakuma et al. [89] proposed that the cohesion did not originate from an adhesive force but rather from the roughness of the potential energy surfaces of sliding planes through DFT, which was the origin of molecular friction of minerals. It indicated that the effect of cohesion of clay minerals on various influential factors was complex, and should be investigated in the future.
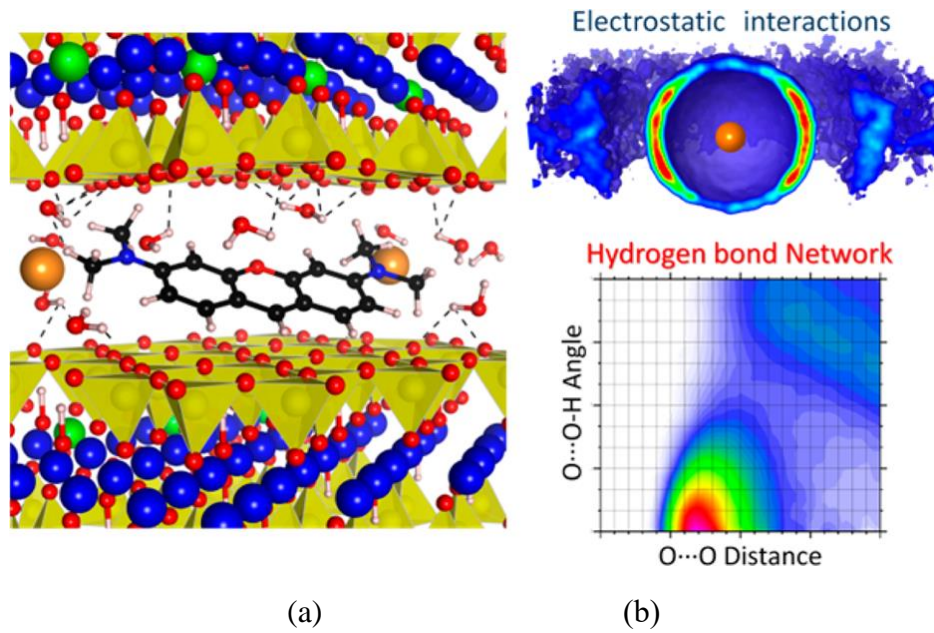
(a)   (b)

Figure 3-7. (a) The structure of Clay-Dye hybrid materials, where the interlayer water, cation, and dye molecules are between two clay layers. (b) The electrostatic interactions between the charged clay mineral sheets and the interlaminar cations and the hydrogen-bond network among water molecules and the clay mineral surface. [125]

Table 3-4. Cohesion (c) of hydrated montmorillonite with different water contents in this work and previous work.

Water content (%)	Cohesion (GPa)		
	Results of different hydrated montmorillonite in this work, sliding velocity is 0.0005 Å/fs	Results of hydrated montmorillonite with a water film under different sliding velocity from our previous MD work [14], where the sliding velocity values are in parentheses.	Results of hydrated montmorillonite through a shear test with a constant shear strain rate of 2×10^{-6} /fs using MD simulation. (Abbasi et al., 2020)
0	1.15	0.387 (0.0001 Å/fs)	0.026 ~ 0.346
5	1.04	2.1496 (0.001 Å/fs)	
10	0.92	6.2693 (0.003 Å/fs)	
15	0.99	8.323 (0.004 Å/fs)	
20	1.00	10.279 (0.005 Å/fs)	
25	0.95		
30	0.93		

3.3.2 Structural properties of interlayer water

Figure 3-8 shows the density profile of oxygen atom in interlayer water molecule for hydrated montmorillonite under different states: the case after NPT equilibrium without normal load, as well as the cases after friction test under normal load of 1 atm and 5 GPa. As shown in Figure 3-8(a) and (b), the density profile of oxygen atoms could slightly change, especially in the cases of low water content of 5 ~ 15%, where one peak changed into one higher peak and another one inapparent peak at 5% and 10 %, and unstable two peaks into two apparent and higher peaks at 15%. As shown in Figure 3-8(b) and (c), with the increasing normal load, the density value of the oxygen atom greatly increases, and the more apparent and stable peak of density is presented, especially for the 20% ~ 30% hydrated montmorillonite. It indicates that the normal load played an essential role in affecting the density profile of interlayer water molecules.

To understand the interaction between interlayer water molecules and montmorillonite surface, the radial distribution function (RDF) of Ob-H_2O atom pair are used to reflect their interaction and analyze the structure of crystals, liquids, and gases. There is usually a long-range ordered structure for crystals, a short-range order and long-range disorder for liquids, or almost no structure for gases. As shown in Figure 3-9 and Figure 3-10(a), the first and second peak values of RDF decline with increasing water content, where the radius corresponding to the first peak is almost unchanged. On the other hand, at high normal loads of 8 and 10 GPa, Figure 3-9(e) and (f) show that the radius corresponding to the first peak in water content of 5% is greater than that of other cases.

As shown in Figure 3-10(a) and Figure 3-9(a, b), the short-range order and long-range disorder of RDFs are found. In Figure 3-9(c ~ f), with the increasing normal load, the long-range order is gradually presented in all cases, where the lower water content or higher normal load, the more obvious the order. It is worth noting that the order of RDF of 5% hydrated montmorillonite is the most obvious at normal load of 3 ~ 10 GPa.

Additionally, as shown in Figure 3-11(a) ~ (c), the interlayer water molecules are all in the middle of the layer at normal load of 1 atm ~ 1 GPa. The interlayer water molecules gradually move towards the surface of the clay with increasing normal load at 3 ~ 10 GPa, as shown in Figure 3-11(d) ~ (g). Moreover, Table 3-5 shows the interlayer spacing of 5% hydrated

montmorillonite declining with increasing normal load, less than 3.3 Å at normal load of 3 ~ 10 GPa, which is further close to that of 2.5 Å for dry montmorillonite. Thus, it could improve interlayer interactions between clay sheets. This could explain why the friction coefficient of 5% hydrated system is the greatest at normal load of 3 ~ 10 GPa (Figure 3-6). Moreover, at the same water content, the higher the normal load, the greater the first and second peak value of RDF, illustrating that the probability of interlayer water molecules around oxygen atom in clay surface increases at higher normal load.
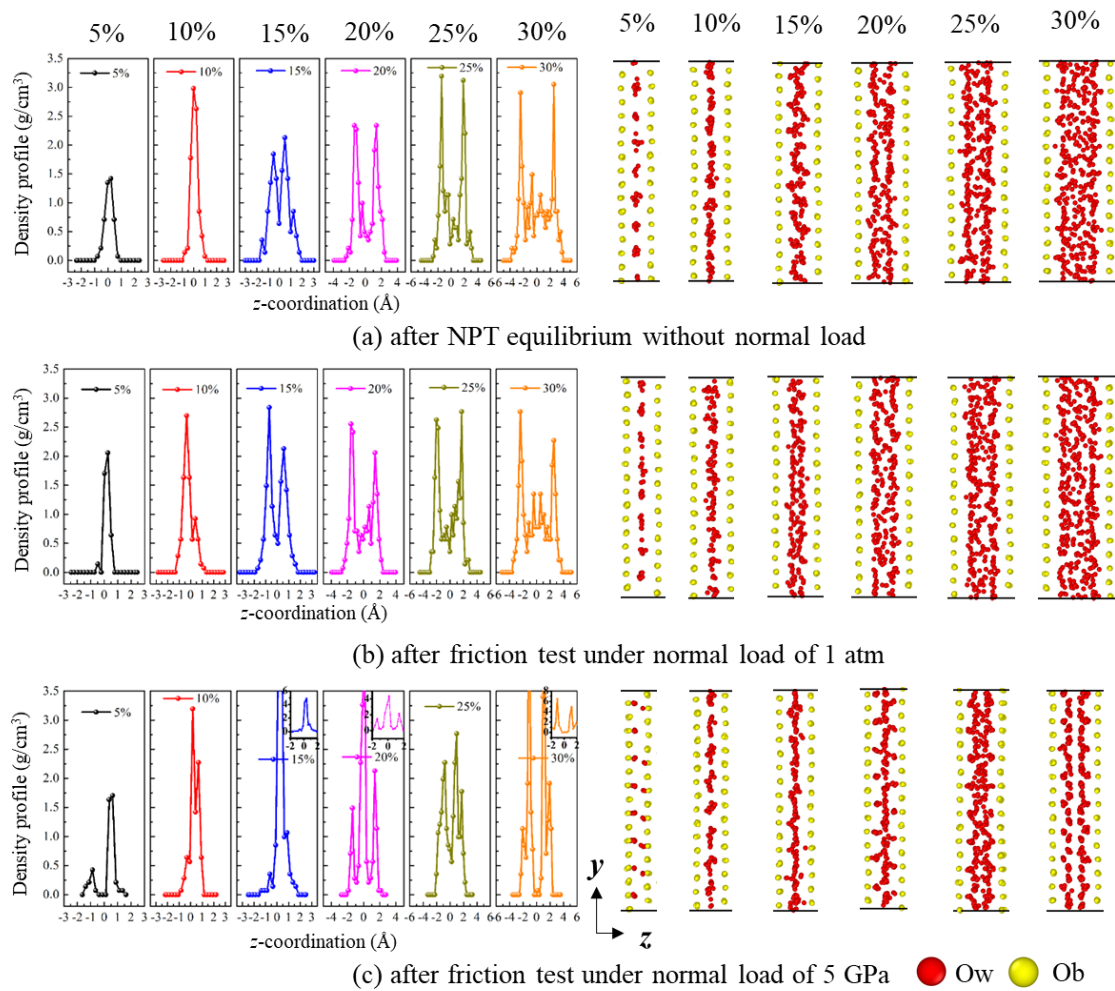

Figure 3-8. Density profile of oxygen atom in interlayer water molecule for different hydrated montmorillonite under different states: (a) after NPT equilibrium without normal load; after friction test under normal load of (b) 1 atm and (c) 5 GPa. Moreover, the right graphs show the distribution of oxygen atoms in interlayer water molecules, where Ob atom (yellow) is the oxygen in the surface of clay, and Ow (red) is the oxygen in the interlayer water molecules. Other atoms in montmorillonite-water system are hidden for a clearer view.
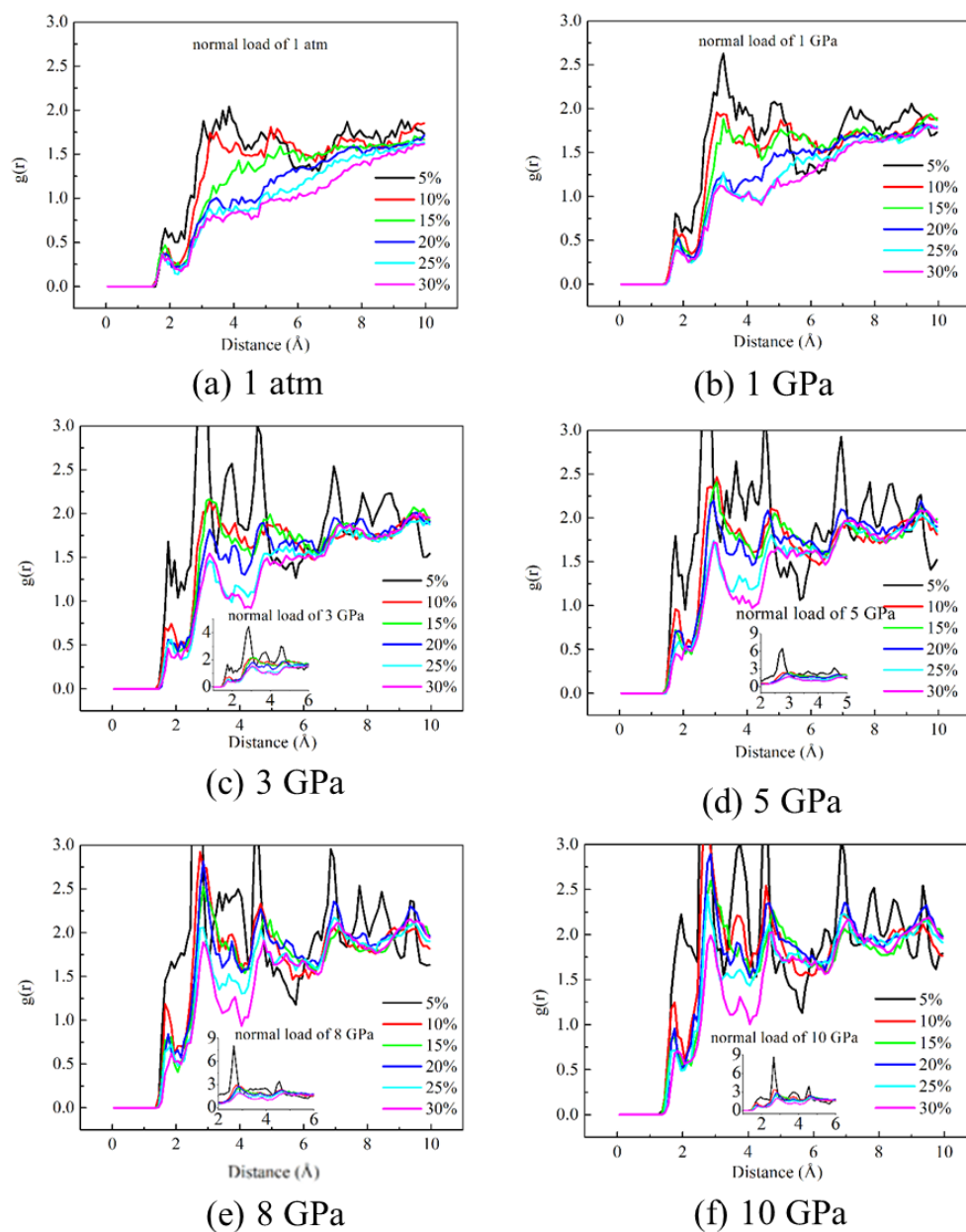
Figure 3-9. RDF of Ob-H₂O for different hydrated montmorillonites under different states: after friction test under normal load of (a) 1 atm, (b) 1GPa, (c) 3 GPa, (d) 5 GPa, (e) 8 GPa, and (f) 10 GPa.
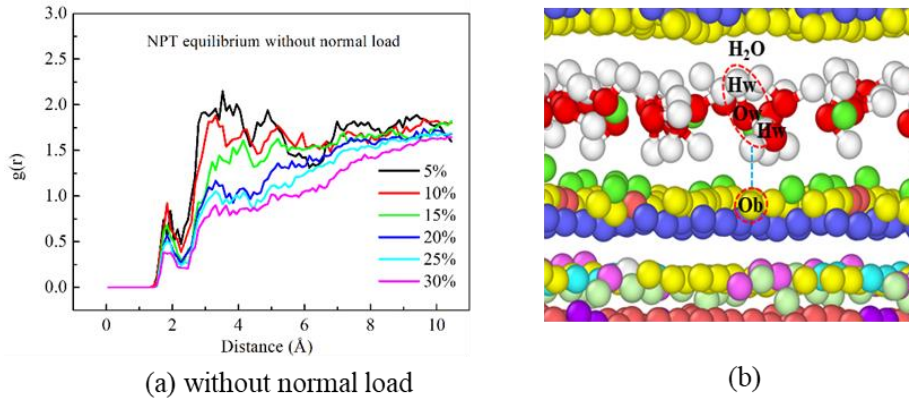
(a) without normal load
(b)

Figure 3-10. (a) RDF of Ob-H_2O for different hydrated montmorillonites under different states: after NPT equilibrium without normal load. Moreover, (b) the graph shows the Ob atom and water molecule.

(a) 0　　(b) 1 atm　　(c) 1 GPa　　(d) 3 GPa

(e) 5 GPa　　(f) 8 GPa　　(g) 10 GPa
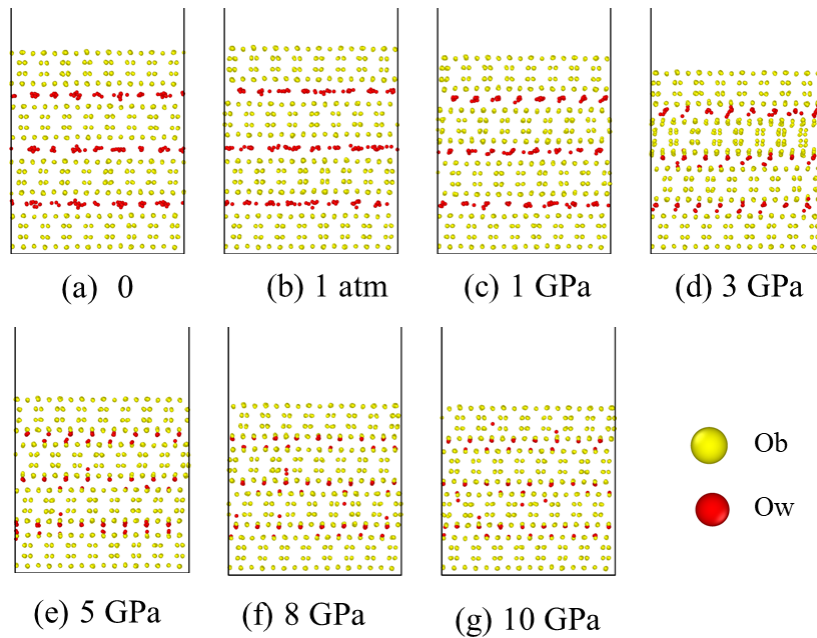
Figure 3-11. The distribution of oxygen atom in interlayer water molecule for 5% hydrated montmorillonite under different states: (a) after NPT equilibrium without normal load; (b) ~ (g) after friction test under normal load of 1 atm ~ 10 GPa, where Ob atom (yellow) is the oxygen in the clay surface, and Ow (red) is the oxygen in the interlayer water molecules.

Table 3-5. Evolution of interlayer spacing of 5% hydrated montmorillonite with normal load.

Normal load (GPa)	Interlayer spacing (Å)
0	4.98
0.0001	4.93
1	4.2

3	3.3
5	2.83
8	2.7
10	2.6

The pore water pressure is usually a key component in assessing the Terzaghi effective normal stress, which generally controls interparticle friction in rock/soil materials. In this MD simulation, the interlayer water pressure in hydrated montmorillonite system was similar to confined water, so it could not be directly regarded as the pore water pressure in macroscale soil sample (see Figure 3-2). It was mainly due to the different scales, as well as forms and states of existence between them. However, the interlayer water pressure was still used to analyze the stress state of interlayer water during friction.

Figure 3-12 and Table 3-6 display the interlayer water pressure along different directions of 5% hydrated montmorillonite, which could be calculated by Eqs.(3-1 ~ 3-3). Note that the pore water pressure in macroscale soil-water sample was the same in all directions, but there were various stress tensors along different directions for water molecules in MD simulation. Moreover, in this work, the interlayer water pressure might have two origins: (1) from water itself, as well as (2) from clay and applied normal load, where the interlayer water could withstand the external load. Figure 3-12(d) and Table 3-6 show that the overall interlayer water pressure increases with rising normal load. It illustrated that the higher the external normal load, the lower the interlayer spacing, and the higher the interlayer water pressure.

The stress tensor for atom i (S_{ab}) is given by the following formula, where a and b take on values x, y, z to generate the components of the tensor, where the tensor for each atom is symmetric with 6 components, such as xx, yy, zz, xy, xz, and yz. In this MD work, the interlayer water pressure (u) in hydrated montmorillonite is equal to the sum of the stress tensor of three main directions (i.e., xx, yy, zz-direction) of interlayer water molecules, and is calculated by the following equations.

$$u = \frac{S_{ab}}{V_i} = \frac{S_{xx} + S_{yy} + S_{zz}}{3V_i} \tag{3-1}$$

$$S_{ab} = -mv_a v_b - W_{ab} \tag{3-2}$$

$$W_{ab} = \frac{1}{2} \sum_{n=1}^{N_p} (r_{1_a} F_{1_b} + r_{2_a} F_{2_b}) + \frac{1}{2} \sum_{n=1}^{N_b} (r_{1_a} F_{1_b} + r_{2_a} F_{2_b})$$

$$+ \frac{1}{3} \sum_{n=1}^{N_a} (r_{1_a} F_{1_b} + r_{2_a} F_{2_b} + r_{3_a} F_{3_b}) + \frac{1}{4} \sum_{n=1}^{N_d} (r_{1_a} F_{1_b} + r_{2_a} F_{2_b} + r_{3_a} F_{3_b} + r_{4_a} F_{4_b}) \qquad (3\text{-}3)$$

$$+ \frac{1}{4} \sum_{n=1}^{N_i} (r_{1_a} F_{1_b} + r_{2_a} F_{2_b} + r_{3_a} F_{3_b} + r_{4_a} F_{4_b}) + \text{Kspace}(r_{i_a}, F_{i_b}) + \sum_{n=1}^{N_f} r_{i_a} F_{i_b}$$

where $-mv_a v_b$ is a kinetic energy contribution for atom i, and W_{ab} is the virial contribution due to intra and intermolecular interactions. For more details, please refer to the "compute stress/atom" command explanation in LAMMPS [50].
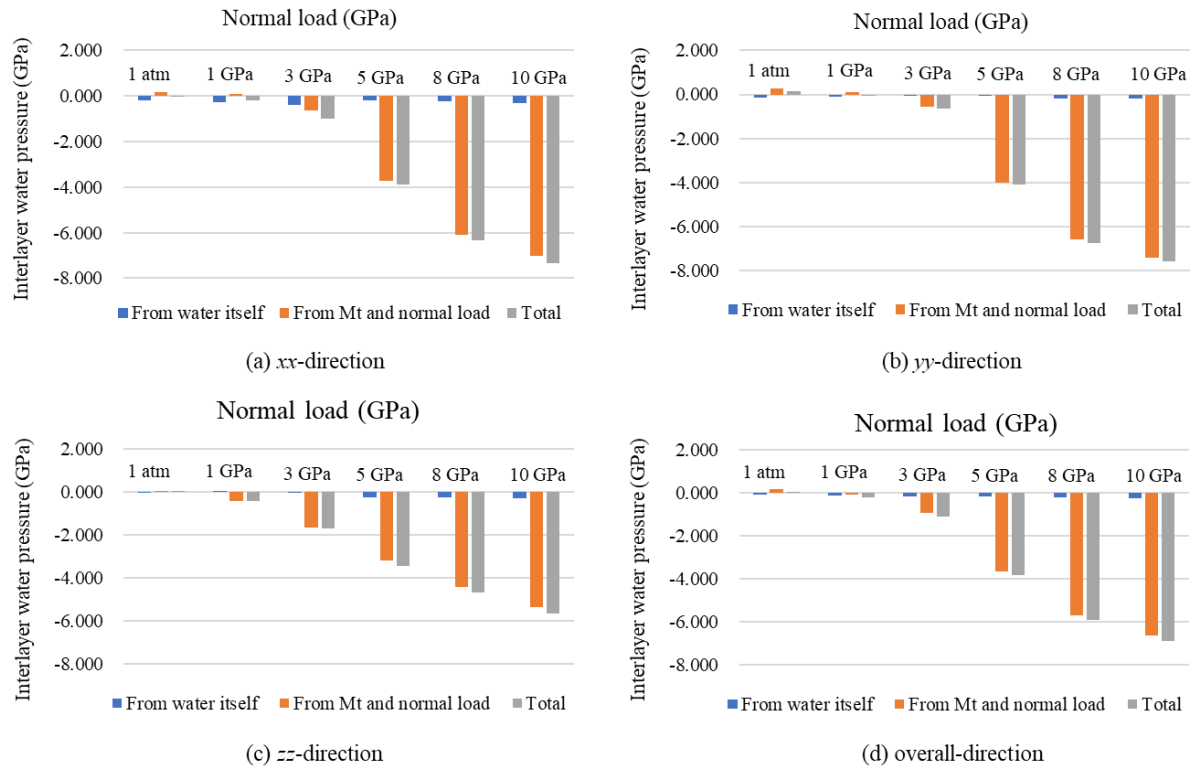

(a) *xx*-direction

(b) *yy*-direction

(c) *zz*-direction

(d) overall-direction

Figure 3-12. Interlayer water pressure along different directions (i.e., (a) *xx*-direction, (b) *yy*-direction, (c) *zz*-direction, and (d) overall-direction) of 5% hydrated montmorillonite at different normal loads, where interlayer water pressure (*u*) in overall direction is the arithmetic mean of three directions (i.e., *xx*, *yy*, *zz*-direction).

Table 3-6. Interlayer water pressure along different directions of 5% hydrated montmorillonite at different normal loads, where interlayer water pressure (*u*) in overall direction is the arithmetic mean of three directions (i.e., *xx*, *yy*, *zz*-direction).

Normal load (GPa)	From water itself	From Mt and normal load	Total	Direction
0.0001	-0.185	0.153	-0.032	*xx*-direction

1	-0.270	0.090	-0.180	
3	-0.395	-0.613	-1.007	
5	-0.169	-3.721	-3.890	
8	-0.242	-6.086	-6.328	
10	-0.316	-7.003	-7.319	
0.0001	-0.127	0.260	0.133	
1	-0.122	0.120	-0.003	
3	-0.081	-0.547	-0.629	
5	-0.066	-4.013	-4.079	
8	-0.175	-6.583	-6.758	
10	-0.167	-7.446	-7.613	*yy*-direction
0.0001	-0.005	0.033	0.028	
1	0.002	-0.424	-0.423	
3	-0.059	-1.646	-1.705	
5	-0.254	-3.207	-3.462	
8	-0.276	-4.420	-4.696	
10	-0.298	-5.376	-5.675	*zz*-direction
0.0001	-0.106	0.149	0.043	
1	-0.130	-0.072	-0.202	
3	-0.178	-0.935	-1.114	
5	-0.163	-3.647	-3.810	
8	-0.231	-5.696	-5.927	
10	-0.260	-6.609	-6.869	overall-direction

3.3.3 Effect of interlayer water on the interaction between montmorillonite layers

To understand the effect of interlayer water molecules on the interaction between montmorillonite layers, Table 3-7 shows the pairwise interaction energy and force between the first and second clay layers (Figure 3-1(b)) before SMD pulling. The absolute value of pairwise interaction energy reduced gradually with increasing water content. However, it is noted that the total pairwise interaction force at 5% hydration was the highest, which might explain why the friction coefficient of 5% hydrated montmorillonite is the highest.

Thereafter, SMD puling along z-direction of montmorillonite was conducted. The evolution of z-pulling force with z-displacement is shown in Figure 3-13(a), where the z-maximum pulling

force decreases significantly with increasing water content in ranging of 0 ~ 10%; while slightly declines for water content of 10 ~ 30% (Figure 3-13(b)). It indicates that water molecules in the interlayer spacing of montmorillonite reduce significantly the interaction of up and down layers, which is why z-maximum pulling force of dry montmorillonite is greatly higher than hydrated ones. With the increasing water content, the basal spacing of montmorillonite constantly rose, causing further reduction in the non-bonded interaction between montmorillonite layer.
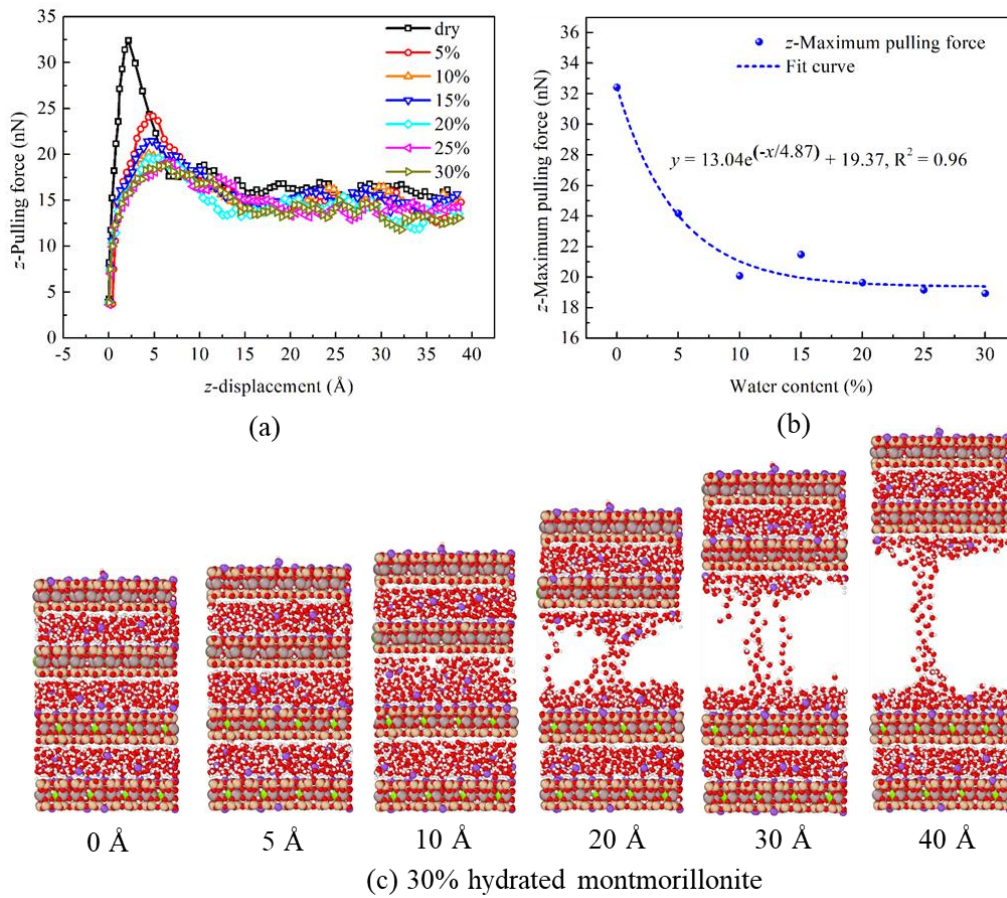

(a)

(b)

| 0 Å | 5 Å | 10 Å | 20 Å | 30 Å | 40 Å |

(c) 30% hydrated montmorillonite

Figure 3-13. Relationship of (a) z-pulling force and z-displacement, and (b) z-maximum pulling force and water content during SMD pulling process. Moreover, (c) the structure of 30% hydrated montmorillonite at different pulling distance.

Table 3-7. Pairwise interaction energy and its force between the first and second clay layers before SMD pulling, where pairwise interaction force in overall direction is the square mean of the other three directions (i.e., x, y, z-direction).

Water content (%)	Pairwise interaction energy (kcal/mol)	Pairwise interaction force (nN)			
		x-direction	y-direction	z-direction	Overall-direction
0	-422.289	0.621	-4.105	1.439	1.465

5	-209.629	0.235	-0.391	-11.945	3.984
10	-30.475	0.033	-0.027	-2.236	0.746
15	-28.570	-0.148	0.022	-2.131	0.712
20	-11.331	-0.028	0.008	-1.157	0.386
25	-6.761	-0.005	-0.021	-0.771	0.257
30	-7.028	0.005	-0.019	-0.767	0.256

3.4 Conclusions

The nanoscale friction properties of various hydrated montmorillonites have been studied using molecular dynamics simulations, considering the coupling effect of water content and normal load. This work may provide an insight into the friction behavior of hydrated clay. The conclusions are as follows:

(1) At the same water content, the friction load and its wave amplitude, as well as the Potential of mean force (PMF) value, increased with the increasing normal load, indicating that more energy was required to slide at higher normal load. On the other hand, the friction coefficient of $0.058 \sim 0.17$ for hydrated montmorillonite with water content of $0 \sim 30\%$ is consistent with the previous experimental and simulation studies, and further illustrates the weak friction properties of montmorillonite.

(2) At low normal load of 1 atm $\sim$ 1 GPa, the higher the water content, the lower the average friction load and ultimate PMF of montmorillonite. However, at high normal load of $3 \sim 10$ GPa, the friction coefficient of 5% hydrated montmorillonite is the highest, compared to the dry state and other higher water content.

(3) With the increasing normal load, the redistribution of interlayer water was developed, showing more apparent and stable peak of density. On the other hand, the long-range order of RDFs of $Ob-H_2O$ is more obvious at the lower water content and higher normal load; while the short-range order and long-range disorder of RDFs are found at low normal load.

(4) The interlayer water could significantly reduce the interaction between montmorillonite layers, especially the system changes from a dry state to a hydrated state. Moreover, the basal spacing of montmorillonite constantly increased with water content, resulting in decreasing the non-bonded interaction between montmorillonite layer.

(5) There are some interesting questions: a) Why is there a stick-slip effect during the shear or friction process of materials? b) Does interlayer water in clay minerals play a role in lubrication or bonding? c) How much interlayer water is needed to stabilize the lubricant? For example, the friction mechanism of water content of 5% and 20% for hydrated montmorillonite was worth further investigating in the future.

Chapter 4

Nanoscale Friction at the Quartz-Quartz and Quartz-Clay Interface

Chapter 4. Nanoscale Friction at the Quartz-Quartz and Quartz-Clay Interface [II]

Abstract

The nanoscale friction behavior of quartz-quartz, quartz-kaolinite, and quartz-montmorillonite interfaces is investigated through Molecular Dynamics simulations. The effects of normal load, sliding velocity, temperature, and hydration on the friction behavior are discussed, and the friction mechanism of quartz-quartz and quartz-clay interface is revealed. The friction coefficients of all systems at different cases are obtained and compared with other experimental results for validation. The simulation results show that the stick-slip effect in all interfaces was found during the friction process, where the higher the sliding velocity and hydration, or the lower the normal load, the weaker the stick-slip effect. The friction load increased with the rising normal load, and the relationship between shear stress and normal load was approximately linear. The friction coefficient and cohesion of the quartz-quartz interface could rise with the increasing sliding velocity or the decreasing temperature. The higher the radius of cation, the lower the friction coefficient, and the higher the cohesion. Moreover, the friction coefficient of quartz-kaolinite was significantly smaller than that of quartz-quartz, indicating that the presence of clay could weaken the frictional strength of quartz. The effect of the interlayer water film on friction behavior was rather complex, showing the lubricating or bonding role, which has been discussed and analyzed in the present study.

Keywords: Quartz; Kaolinite; Montmorillonite; Molecule dynamics; Nanoscale friction; Interface.

4.1 Introduction

Quartz is the main component of igneous, metamorphic, and sedimentary rocks[126], and a better understanding of its mechanical properties is certainly essential for rock engineering. The shear failure process of rock subjected to shear stress could be regarded as the sliding friction process of rock particles, where the interface friction behavior of rock relates significantly to understanding the fault instability and failure in fault zones[127], geotechnical engineering disasters [128], regional seismic dynamics[129], mechanism of rock failure under earthquake[130], etc. For example, quartz particles could be used as a proppant in hydraulic fracturing in oil recovery and mining, and its studies on friction law help understand the motion mechanism of the particles in hydraulic fracturing[131]. Regarding seismic dynamics, the friction characteristics of fault materials could control the mechanism of earthquake nucleation. Thus, the friction studies of quartz and feldspar minerals under different environmental conditions could reveal the mechanism controlling the transition depth under the seismogenic zone[130], and explain the weakening mechanism of quartz rock under sub-seismic conditions[132].

So far, quartz's friction characteristic has been studied through experimental and theoretical derivation methods. In terms of the theoretical derivation field, Barthélémy et al.[133] established a theoretical framework and functions using the mean value technique, and then estimated the friction coefficient of quartz and clay mixed gouge. Aharonov et al.[134] proposed a theoretical model, and found that the sliding velocity and temperature played an essential role in the friction behavior of rock. Hu et al.[135] reported the temperature and pore pressure related significantly to the friction coefficient of rock. On the other hand, in terms of experimental tests, Fall et al.[129] studied the friction behavior of sand under dry and wet conditions, and found that the friction coefficient was closely related to the shear modulus. Kasyap et al.[136] studied the influence of coupling contact time and loading rate on the interface behavior of quartz grains using interface micromechanics experiments, and reported that its average friction coefficient was 0.21. Zhang et al.[137] illustrated that the friction coefficient of quartz sand increased with increasing normal load. Yang et al.[131] discussed the effects of water absorption and surface layer stripping on friction properties of quartz sand through self-made experimental equipment. Kanagawa et al.[132] reported that the temperature controlled the friction strength of quartz rock under sub-

seismic slip velocity. The studies mentioned above indicate that the friction properties of quartz are very complex and are affected by many environmental factors, such as the normal load, pore pressure, sliding velocity, temperature, hydration, surface defects and stiffness, etc. Furthermore, Tembe et al.[74] explored the friction behavior between quartz and clay minerals (containing montmorillonite and illite) using a conventional triaxial shear test, and reported that the friction coefficient of quartz-clay interface decreased with the increase of clay content. Thus, the friction between different material substrates is also worth concern.

In addition, with the rapid development of nanoscience and technology at the end of the 20th century, numerous mechanical phenomena and their mechanism have been explored from macroscale to nanoscale. The development and contribution of nano-tribology[77] are critical in the field of tribology, because more basic mechanisms of friction exist at nanoscale[23]. Plenty of experimental and simulation methods have been well developed in nano-tribology, such as atomic force microscopy[78], friction Force Microscopy[79], optical microscope and Scanning Electron Microscopy (SEM)[80], molecular dynamic (MD) simulation method[14], etc. In nano-tribology, lots of works focused on the friction behavior of graphene[138], carbon[84], muscovite mica[78], nanocomposites[80], etc. Recently, the nanoscale friction behavior of clay and silica was starting to get more attention using MD simulation[14, 20, 86]. At present, the interface friction behavior of quartz particles in experiment test is still limited to the millimeter level, which shows that the nanoscale friction behavior of quartz or quartz-clay mixture interface remains still unclear.

In this work, MD simulation method is performed to study the nanoscale friction behavior of quartz, considering the normal load, sliding velocity, temperature, and hydration. Moreover, the friction properties of quartz-kaolinite and quartz-montmorillonite interface is also discussed, to explore the effect of substrate on friction behavior. This work could give an insight into the nanoscale friction behavior of quartz and quartz-clay, which is to extend the friction properties of quartz from macroscopic scale to nanoscale. Furthermore, the friction coefficient and cohesion are obtained by derivation, which could provide a reference for critical parameter input in discrete element simulation.

4.2 Computational details

4.2.1 System setup and force field

The unit cell of quartz crystal was derived from the model of Levien et al.[139], and its supercell ($10a \times 7b \times 4c$) of $49.16 \times 34.412 \times 21.6216$ Å^3 was established as the sliding block in whole work, and its another supercell ($22a \times 19b \times 4c$) of $108.152 \times 93.404 \times 21.6216$ Å^3 as the substrate, as shown in Figure 4-1(c). Based on the previous experimental findings[140, 141], as shown in Figure 4-1(a), a hydroxyl group is assigned on each surface Si atom in quartz (hydrated form: ≡Si-OH), and it is the most probable form on the fully hydroxylated silica surface[142]. On the other hand, the model of kaolinite used in this work was derived from Bish and his co-workers[143], and its supercell ($21a \times 10b \times 3c$) of $108.213 \times 89.42 \times 22.173$ Å^3 was established as another substrate, as shown in Figure 4-1(d). Moreover, Figure 4-1(a) shows the interlayer water film with a density of around 1 g/cm^3, which is obtained and relaxed in LAMMPS[144], and described by the flexible SPC water model[145]. The initial thickness of the interlayer water film containing 435 water molecules was about 6.6 Å. Figure 4-1(c) and (d) display the four cases used in this work, such as quartz-quartz, quartz-water-quartz, quartz-kaolinite, and quartz-water-kaolinite, where the contact surface of quartz is its (001) crystal plane, and that of kaolinite is the hydroxy-hydrogen plane. Furthermore, the vacuum of over 50 Å in the above four cases was used to avoid the interaction between the neighboring upper and lower boundary atoms of the whole system due to the periodicity of the z-direction.

As shown in Figure 4-1(a), the above four simulation systems contain three kinds of atoms: boundary atoms (orange), thermostat atoms (blue), and Newtonian atoms (colored). 1) The lower and upper boundary atoms (orange) were set as rigid bodies, where the lower boundary atoms was fixed in their position during the whole simulation, and the upper boundary atoms transferred the external normal loads on the whole system. 2) The thermostat atoms (blue) was set as a temperature-controlled layer to keep the whole system at a target temperature. 3) The Newtonian atoms (colored) was free to move. The above simulation setting method was similar to the previous literature [14], which studied the nanoscale friction behavior of clay-water system in steered molecular dynamics (SMD) simulation. CLAYFF force field[52] has been effectively used for clay minerals[55, 95] and quartz-water system[146, 147] in MD simulation, so it is employed

in this work. Furthermore, the building way of quartz-montmorillonite interface is similar to the quartz-quartz and quartz-kaolinite interface, as shown in Figure 4-2.
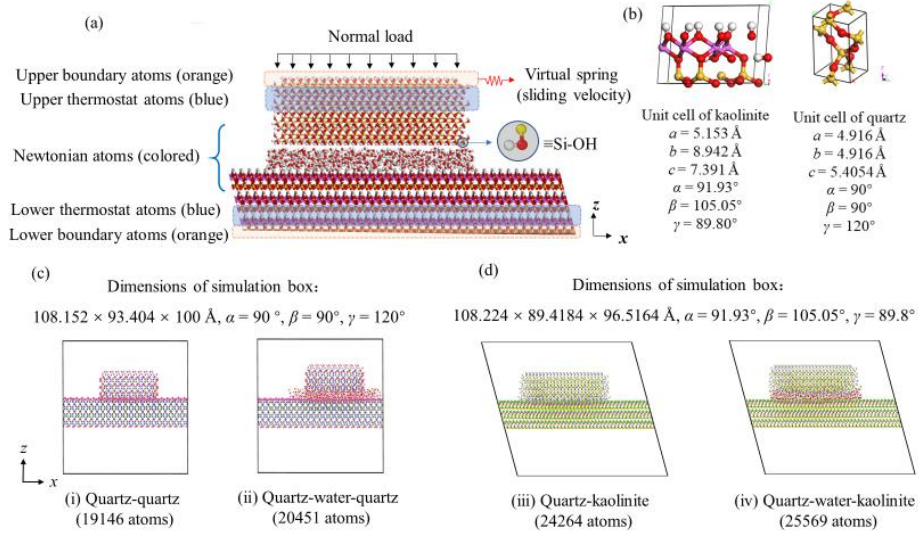

Figure 4-1. (a) The quartz-water-kaolinite interface used in this work under steered molecular dynamics (SMD) friction along *x*-direction. This model contains three kinds of atoms: boundary atoms (orange), thermostat atoms (blue), and Newtonian atoms (colored), where (1) lower boundary atoms (orange) - rigid and fixed position; (2) upper boundary atoms (orange) - rigid and upon applied a normal load and a controlled sliding velocity via a virtual spring along the *x*-direction for SMD friction; (3) thermostat atoms (blue) - temperature-controlled layers; (4) atoms (colored) - free to move. (b) Unit cell of kaolinite and quartz. (c), (d) the four cases used in this work for SMD friction along *x*-direction, such as quartz-quartz, quartz-water-quartz, quartz-kaolinite, and quartz-water-kaolinite.
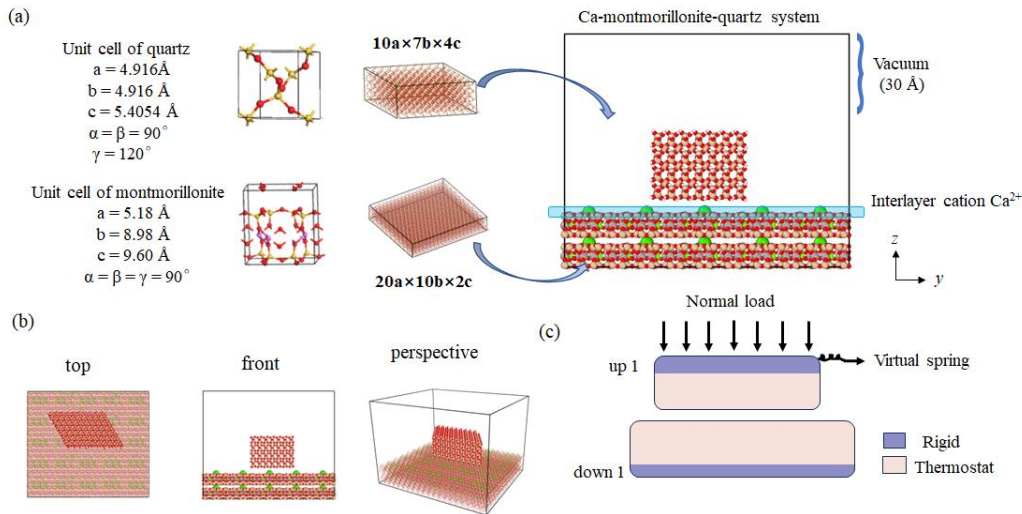

Figure 4-2. Ca-montmorillonite-quartz model used in this work: (a) one quartz

portion with two montmorillonite films placed in the bottom of the simulation box. (b) simulation box in other three angle of view: top, front and perspective. (c) purple portions are rigid in all directions but up1 can move in z-direction when subjected to a normal force, pink layers are used to control temperature. The system operates functionally under normal stress and horizontal spring forces acting on the up1 layer.

Table 4-1. Lennard-Jones parameters of quartz-water-kaolinite system applied in this work.

Species	Symbol	Charge (e)	ε (kcal/mol)	σ (Å)	Ref.
water hydrogen (SPC)	Hw	0.41			a
water oxygen (SPC)	Ow	-0.82	0.1554	3.1655	a
hydroxyl hydrogen	Ho	0.425			b
hydroxyl oxygen	Oh	-0.95	0.1554	3.1655	b
bridging oxygen	Ob	-1.05	0.1554	3.1655	b
tetrahedral silicon	Si	2.1	1.8405×10^{-6}	3.3020	b
octahedral aluminum	Al	1.575	1.3298×10^{-6}	4.2713	b

a:[145]; b:[52].

4.2.2 Simulation details

MD simulations were performed with LAMMPS code[144]. The Ewald's[148] summation method with an accuracy of 1.0e-4 kcal/mol was applied for the long-range electrostatic interactions, and the Velocity Verlet algorithm[97] was used for integrating the motion equations. Periodic boundary condition was used in three directions of the whole system; while the vacuum of over 50 Å in z-direction was equivalent to two-dimensional (x, y) periodicity. The cut-off radius was set as 10 Å, and the time step was 1.0 fs in whole simulations.

The four cases mentioned above were equilibrated according to the following steps. 1) To release all freedom degrees of the system, the conjugate gradient algorithm was conducted for energy minimization. 2) The thermostat atoms (blue) and Newtonian atoms (colored) were equilibrated with micro-canonical (NVE) ensemble for 200 ps, where the boundary atoms (orange) were without ensemble and set as rigid in whole simulations. 3) Thereafter, the temperature of thermostat atoms (blue) was controlled in canonical (NVT) ensemble for 200 ps, and then transferred to the Newtonian atoms (colored), to ensure the temperature of

Newtonian atoms (colored) fluctuated around the target temperature. 4) The different normal loads of 0 ~ 7 GPa were further applied to the upper boundary atoms (orange) for 200 ps, where the setting method of the ensemble remained unchanged. 5) After relaxation for all systems, to explore the effect of normal load on friction behavior of quartz-quartz interface, the upper boundary atoms (orange) was applied by a controlled sliding velocity of 100 m/s (0.001 Å/fs) via a virtual spring along the *x*-direction for SMD friction under different normal loads of 0 ~ 7 GPa (Figure 4-1) at 300 K, where the stiffness coefficient of virtual spring was 200 kcal/mol/Å^2 (about 139 N/m). 6) To understand the effect of sliding velocity on friction behavior, the sliding velocity of 10, 50, 100, 150, and 200 m/s were considered for SMD friction, and the normal load was set as 5 GPa. 7) Moreover, the different temperatures of 200, 300, and 400 K were performed, where the sliding velocity was 100 m/s. 8) Thereafter, the friction behavior of quartz-kaolinite, quart-water-quartz, and quartz-water-kaolinite interfaces was studied to understand the effect of different substrate materials and hydrated conditions. It was noted that a sliding distance of about 100 Å was obtained for all the above simulations.

Similarly, the simulation schemes for quartz-montmorillonite system is shown in Table 4-3.

Table 4-2. MD simulations schemes for quartz-quartz/kaolinite systems in this work.

Step	Equilibrium (Equi.) and steered molecular dynamics (SMD) process	
1	Minimize	Conjugate gradient (CG) algorithm: the energy of 1.0e-14, the force of 1.0e-12 kcal•(mol•Å)-1, and the maximum number of iteration steps of 1000.
2	Equi.1	Thermostat atoms (blue) and Newtonian atoms: NVE, 200 ps
3	Equi.2	Thermostat atoms (blue): NVT + Newtonian atoms: NVE, 200 ps
4	Equi.3 under normal load	Thermostat atoms (blue): NVT + Newtonian atoms: NVE + under different normal loads of 0 ~ 7 GPa, 200 ps
5	SMD friction along x-direction for quartz-quartz interface	Effect of normal load on friction behavior: sliding velocity of 100 m/s, 100 ps; under different normal loads of 0 ~ 7 GPa and 300 K.
6	(Thermostat atoms (blue): NVT + Newtonian atoms:	Effect of sliding velocity on friction behavior: sliding velocity of 10 ~ 200 m/s, 50 ~ 1000 ps (ensuring the sliding distance of about 100 Å); under normal loads of 5 GPa and 300 K.
7	NVE)	Effect of temperature on friction behavior: sliding velocity of 100 m/s, 100 ps; under normal loads of 0 ~ 7 GPa and 200 ~ 400 K.

8	SMD friction along x-direction for quartz-water-quartz, quartz-kaolinite, and quartz-water-kaolinite interfaces	Effect of different substrate materials and hydrated condition: sliding velocity of 100 m/s, 100 ps; Thermostat atoms (blue): NVT + Newtonian atoms: NVE + under different normal loads of 0 ~ 7 GPa and 300 K.

Table 4-3. MD simulation schemes for quartz-montmorillonite system

Steps	Relaxation and Steered molecular dynamics (SMD) simulation process	
1	Energy minimization	Conjugate Gradient (CG.) Algorithm
2	First relaxation	NVT ensemble relaxation for 1000 ps
3	Second relaxation	NVT ensemble, Langevin temperature control (300K), different normal loads: 1 GPa ~8 GPa, relaxation for 400 ps
4	SMD friction simulation	NVT ensemble, Langevin temperature control (300K), different normal loads: 1 GPa ~ 8 GPa, Conduct SMD friction simulation along the y-direction, with a sliding speed of 50 m/s and a simulation time of 200 ps

4.3 Results and discussions

Section 4.3.1 mainly discusses the friction behavior of quartz-quartz interface, where 4.3.1.1 shows the fluctuation regulation of the virtual spring force for a single block of quartz and the friction load of quartz-quartz interface. Sections 4.3.1.2, 4.3.1.3, and 4.3.1.4 show the effect of normal load, sliding velocity, and temperature on the friction behavior of quartz-quartz interface, respectively. Sections 4.3.2 and 4.3.3 consider the case of the different substrate materials and hydrated conditions for quartz-water-quartz, quartz-kaolinite, and quartz-water-kaolinite interfaces. Section 4.3.4 shows the stick-slip effect and relationship of shear stress and normal load. Section 4.3.5 introduces the effect of interlayer cation on friction behavior between quartz-montmorillonite interface.

4.3.1 Friction behavior of quartz-quartz interface

4.3.1.1 Fluctuation regulation of virtual spring force and friction load

To understand the fluctuation regulation of virtual spring force and friction load of quartz, two different cases were considered in this work. The evolution of virtual spring force/friction load with sliding distance for a single block of quartz, and quartz-quartz (containing sliding
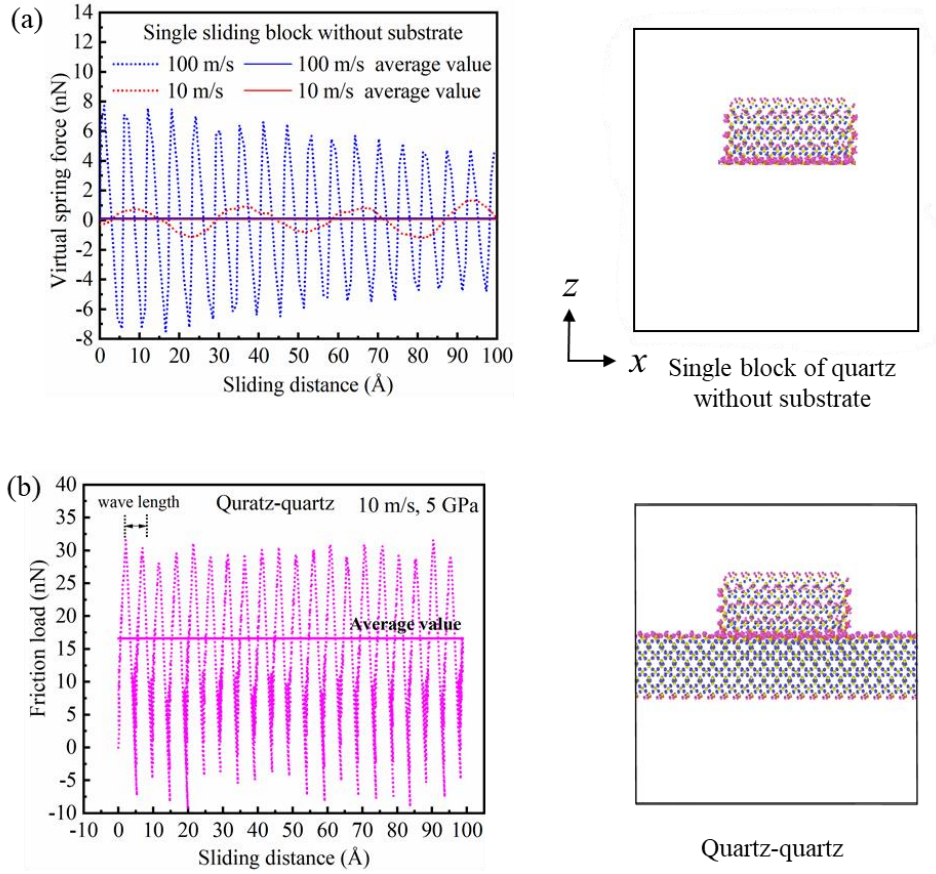
block and substrate) are shown in Figure 4-3.

Figure 4-3. (a) Evolution of virtual spring force with sliding distance for a single block of quartz at sliding velocity of 10 m/s and 100 m/s, as well as normal load of 0 GPa. (b) Evolution of friction load with sliding distance for quartz-quartz interface (containing sliding block and substrate) at sliding velocity of 10 m/s and normal load of 5 GPa. The temperature is fixed at 300 K.

To test the effect of spring tension on the sliding block, in the absence of substrate, Figure 4-3(a) shows the virtual spring force of a single sliding block of quartz without a substrate system at the sliding velocity of 10 and 100 m/s, which fluctuates around 0, and their average value is close to 0. Furthermore, Figure 4-3(b) shows the relationship between friction load and sliding distance for quartz-quartz at a sliding velocity of 10 m/s and a normal load of 5 GPa, where the friction load periodically fluctuated around a stable value (around 17.0 nN), showing the stick-slip effect[149]. Therefore, it could verify that the average value of virtual spring force could be used to reflect the average friction load. The average friction load was used to calculate

the shear stress in this work (equation (2-15)), and then the relationship between shear stress and normal load was obtained.

As shown in Figure 4-3(b), the distance of two wave peaks is about 4.9 Å, which is close to the crystal lattice constant (4.916 Å) in the *x*-direction of quartz. This phenomenon was also found at nanoscale friction of clay in MD simulation[14] and graphite in AFM[149].

4.3.1.2 Effect of normal load on friction behavior

Figure 4-4(a) displays the evolution of friction load with sliding distance, illustrating that the higher the normal load, the higher the friction load. The increment of normal load could affect the periodic variation regulation of friction load, because the interaction between the sliding block and substrate was derived from the intermolecular forces and the normal load applied on the sliding block. The sliding block adhered more closely to the substrate at a higher normal load, causing that lower interlayer spacing and higher intermolecular interaction. Thus, the friction load increased with the increasing normal load.

Figure 4-4(b) shows the relationship between shear stress and normal load, where the shear stress is obtained from the average friction load divided by the shear area (equation (2-15)). The linear relationship between shear stress and normal load was found, where the friction coefficient (i.e., the slope of curve) is 0.27. This value was slightly greater than the previous experimental results, which reported a friction coefficient of 0.21 for quartz particles [136] and a kinetic friction coefficient of 0.093 ~ 0.231 for quartz sand[150]. The dimension of quartz particles used for the microscale experiment was usually micron scale, and the quartz sample in the experiment was constituted of its major mineral quartz, inter-grain cement, and pores[151]. However, the crystalline quartz structure in nanoscale was perfect, and did not contains the inter-grain cement and pores. Consequently, the friction coefficient of quartz in MD simulation was slightly superior to that in the microscale experiment.

Based on the atomic simulation method, Duque-Redondo et al.[125] proposed that the cohesion of clay-water system was derived from the hydrogen-bond interaction between water molecules and clay surface, and the electrostatic interaction between clay and interlayer cations. For dry quartz-quartz interface without water molecules and interlayer cations, the van der Waals and coulomb electrostatic interaction between sliding block and substrate provided mainly the

cohesion of dry quartz-quartz interface. Thus, as shown in Figure 4-4(b), the cohesion of dry quartz-quartz interface is 0.223 GPa. However, as is well known, the cohesion of dry quartz sand is zero at macroscale, which is because macroscale friction mechanism does not consider the van der Waals and coulomb electrostatic interaction. Therefore, the friction mechanism at nanoscale is different from that in macroscale.
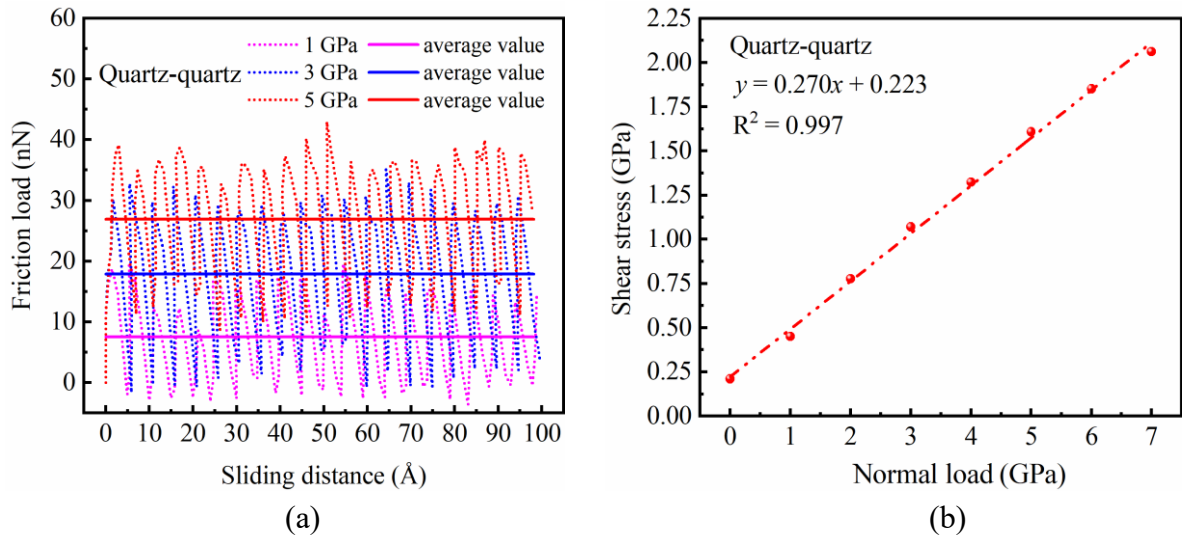

Figure 4-4. (a) Evolution of friction load with sliding distance for quratz-quartz interface under different normal loads; (b) Evolution of shear stress with normal load. The sliding velocity is 100 m/s.

4.3.1.3 Effect of sliding velocity on friction behavior

Figure 4-5(a) shows the evolution of friction load with sliding distance for quratz-quartz interface at sliding velocities of 50, 100, and 200 m/s. The fluctuation amplitude of friction load reduced with the increasing sliding velocity; this phenomenon was also found in previous research for nanoscale friction of clay[14]. In addition, as shown in Figure 4-5(b), the average friction load increased with rising sliding velocity, because the more sliding distance of atomic transition within the same time at the higher velocity, the higher force was required to overcome more interlaminar energy[14].

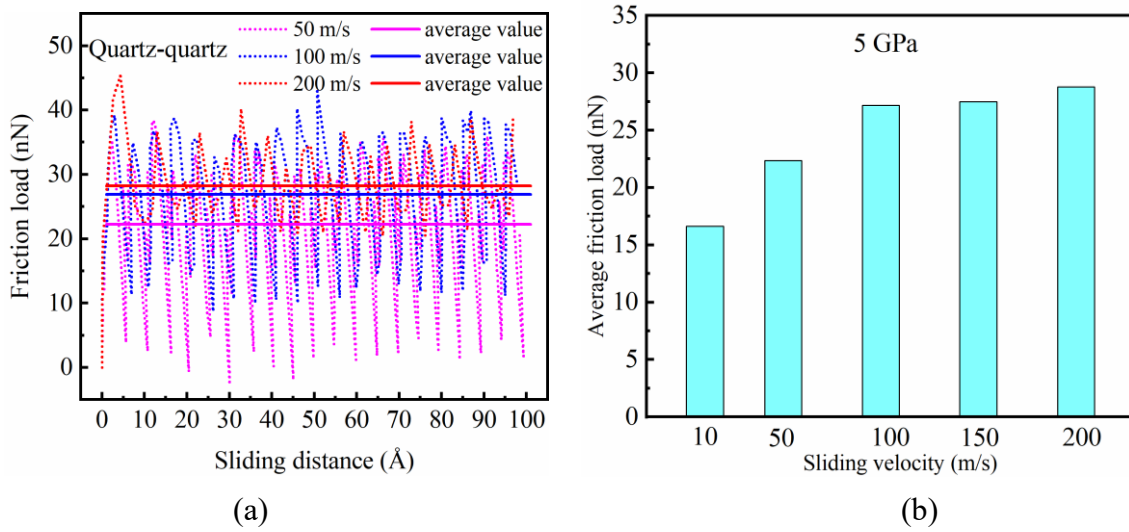(a)   (b)

Figure 4-5. (a) Evolution of friction load with sliding distance for quartz-quartz interface under different sliding velocities; (b) Evolution of average friction load with sliding velocity. The normal load here is 5 GPa.

Besides, the evolution of shear stress with normal load at 300 K and sliding velocity of 50 m/s is shown in Figure 4-6, where the friction coefficient of 0.265 and cohesion of 0.054 GPa are obtained and listed in Table 4-4. It was noted that Table 4-4 collected the friction coefficient and cohesion of various quartz/water/kaolinite interfaces under different conditions in the whole text. As shown in Table 4-4, comparing the sliding velocity of 50 m/s and 100 m/s at 300 K, the friction coefficient of quartz-quartz interface increases slightly with rising sliding velocity, and the cohesion rises significantly. Wei et al.[14] explored the nanoscale friction behavior of montmorillonite in MD simulation, and also found that the friction coefficient and cohesion increased slightly with rising sliding velocity in 10 ~ 500 m/s.
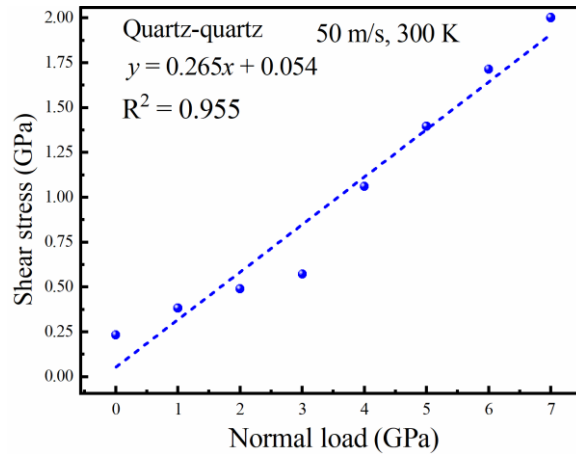

Figure 4-6. Evolution of shear stress with normal load for quartz-quartz interface at

300 K and sliding velocity of 50 m/s.

Table 4-4. The friction coefficient and cohesion of various quartz/water/kaolinite interfaces.

Friction coefficient	Cohesion (GPa)	Condition (Temperature, and siding velocity)	Interface
0.265	0.054	300 K, 50 m/s	Quartz-quartz in this work
0.27	0.223	300 K, 100 m/s	
0.286	0.255	200 K, 100 m/s	
0.266	0.184	400 K, 100 m/s	
0.21	-	300 K	Quartz grains through experiment test[136]
0.093 ~ 0.231	-	300 K	Quartz sand through shear test[150]
0.094	0.215	300 K, 100 m/s	Quartz-water-quartz in this work
0.044	0.402	300 K, 100 m/s	Quartz-kaolinite in this work
0.084	0.263	300 K, 100 m/s	Quartz-water-kaolinite in this work

4.3.1.4 Effect of temperature on friction behavior

To explore the effect of temperature on friction properties of quartz-quartz interface, the relationship of shear stress and normal load under 200 ~ 400 K at a sliding velocity of 100 m/s is shown in Figure 4-7. The friction coefficient and cohesion decreased with rising temperature, which was consistent with the previous research, where Zhao et al.[152] found that the friction load decreased with rising temperature during 140 ~ 400 K for the friction behavior between graphite and silicon nitride through the AFM experiment; while the influence of temperature on friction force reduced at over 400 K. Moreover, based on the Prandtl-Tomlinson (PT) model, Song et al.[153] explained through the energy dissipation aspect why the friction load decreased with rising temperature. As it was well known, the mechanical strength, Young's modulus, and other mechanical indexes of quartz could reduce with increasing temperature[154]. Thus, the decrease of mechanical quantities due to the increasing temperature might be an important factor for friction properties of quartz. On the other hand, the higher temperature, the higher the kinetic energy of quartz-quartz interface, and the easier to accomplish the sliding friction.
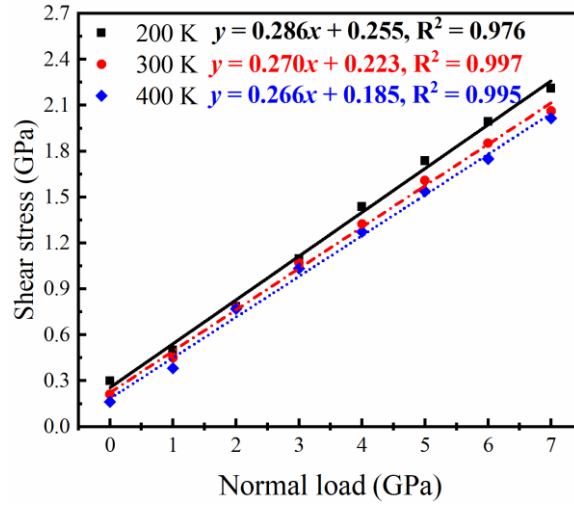
Figure 4-7. Evolution of shear stress with normal load for quartz-quartz interface under different temperatures of 200 ~ 400 K. The sliding velocity is 100 m/s.

4.3.2 Friction behavior of quartz-kaolinite interface

To explore the friction behavior between quartz and clay, Figure 4-8 shows the relationship between friction load and sliding distance for quartz-kaolinite interface at a sliding velocity of 100 m/s, where the kaolinite is set as the substrate. As shown in Figure 4-8(a), the higher the normal load, the higher the friction load.

The relationship between friction load and sliding distance for quartz-quartz and quartz-kaolinite interfaces at a normal load of 5 GPa and 100 m/s is shown in Figure 4-8(b), where the length of two wave peaks in two interfaces are much close. Because the lattice parameter of kaolinite along sliding direction is close to that of quartz. Moreover, the fluctuation amplitude of quartz-quartz interface was greater than that of quartz-kaolinite.

Figure 4-8(c) and Table 4-4 show a friction coefficient of 0.044 for quartz-kaolinite interface, which is significantly less than 0.27 for quartz-quartz interface at 300 K and a sliding velocity of 100 m/s. This finding agreed well with the previous experimental research of Tembe et al.[74], who found that the friction coefficient of the mixed quartz-clay interface could decrease with the increase of clay content. On the other hand, the cohesion of 0.402 GPa for quartz-kaolinite interface is higher than that of quartz-quartz interface (0.223 GPa).
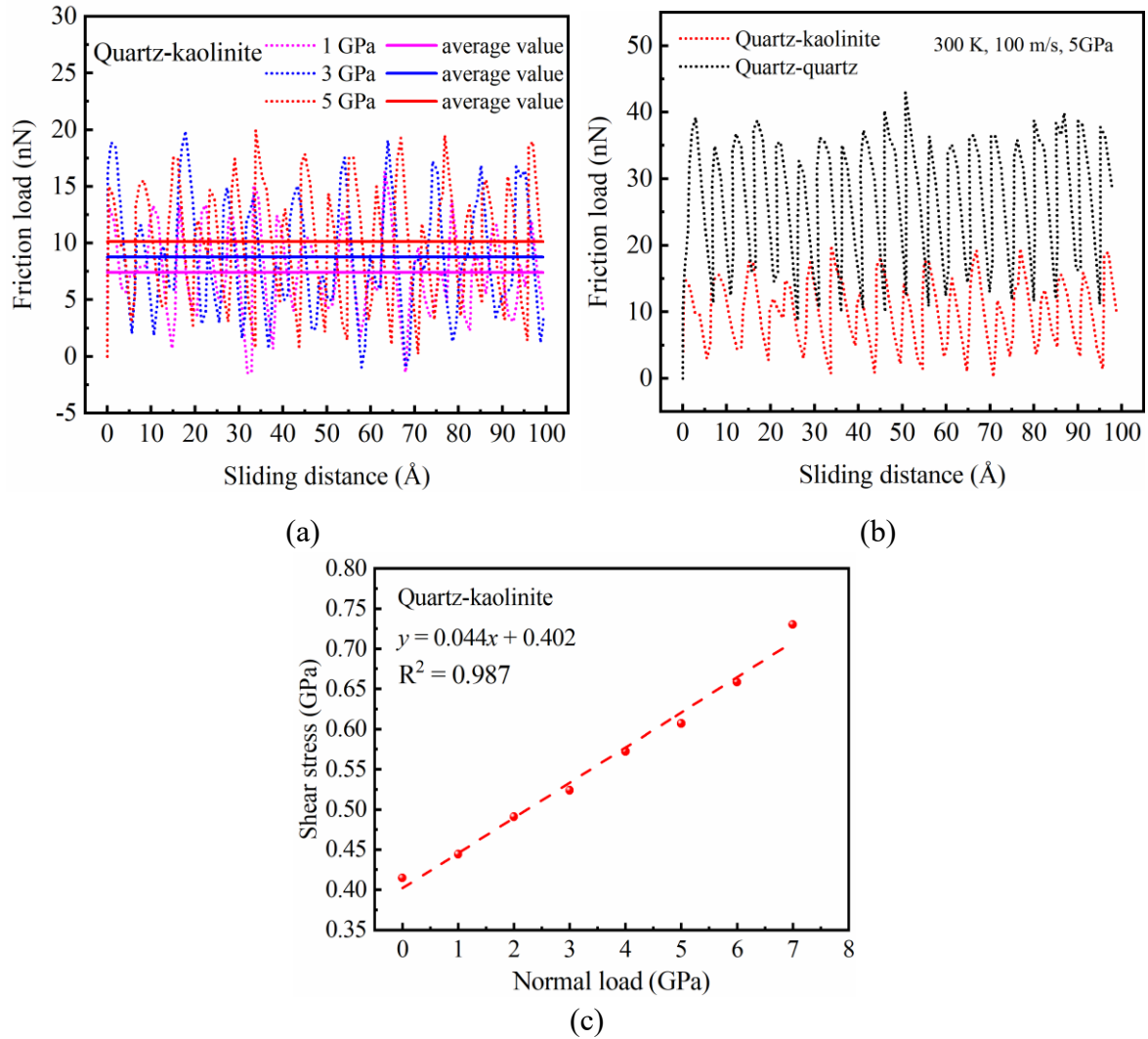
(a)

(b)

(c)

Figure 4-8. (a) Evolution of friction load with sliding distance for quartz-kaolinite interface under different normal loads; (b) Comparison of the relationship between friction load and sliding distance for quartz-quartz and quartz-kaolinite interface, where the normal load is 5 GPa; (c) Evolution of shear stress with normal load for the two interfaces. The sliding velocity corresponds to 100 m/s in this section.

4.3.3 Effect of interlayer water on friction behavior

As shown in Figure 4-9, the interlayer water film in quartz-water-quartz interface is constantly discharged during friction process. At a normal load of 1 GPa, the thickness of the interlayer water film between the sliding block and the substrate decreases till one-layer water molecules (Figure 4-9(a) and (b)). However, at a normal load of 5 GPa, only a few water molecules remained between the sliding block and the substrate (Figure 4-9(c) and (d)), and the rest water molecules were located directly in front of the sliding block along the sliding

direction, which became a part of the sliding block. This could explain why the friction load gradually rose during the friction process (Figure 4-11(a)). A similar evolution was also found for quartz-water-kaolinite interface, as shown in Figure 4-10.
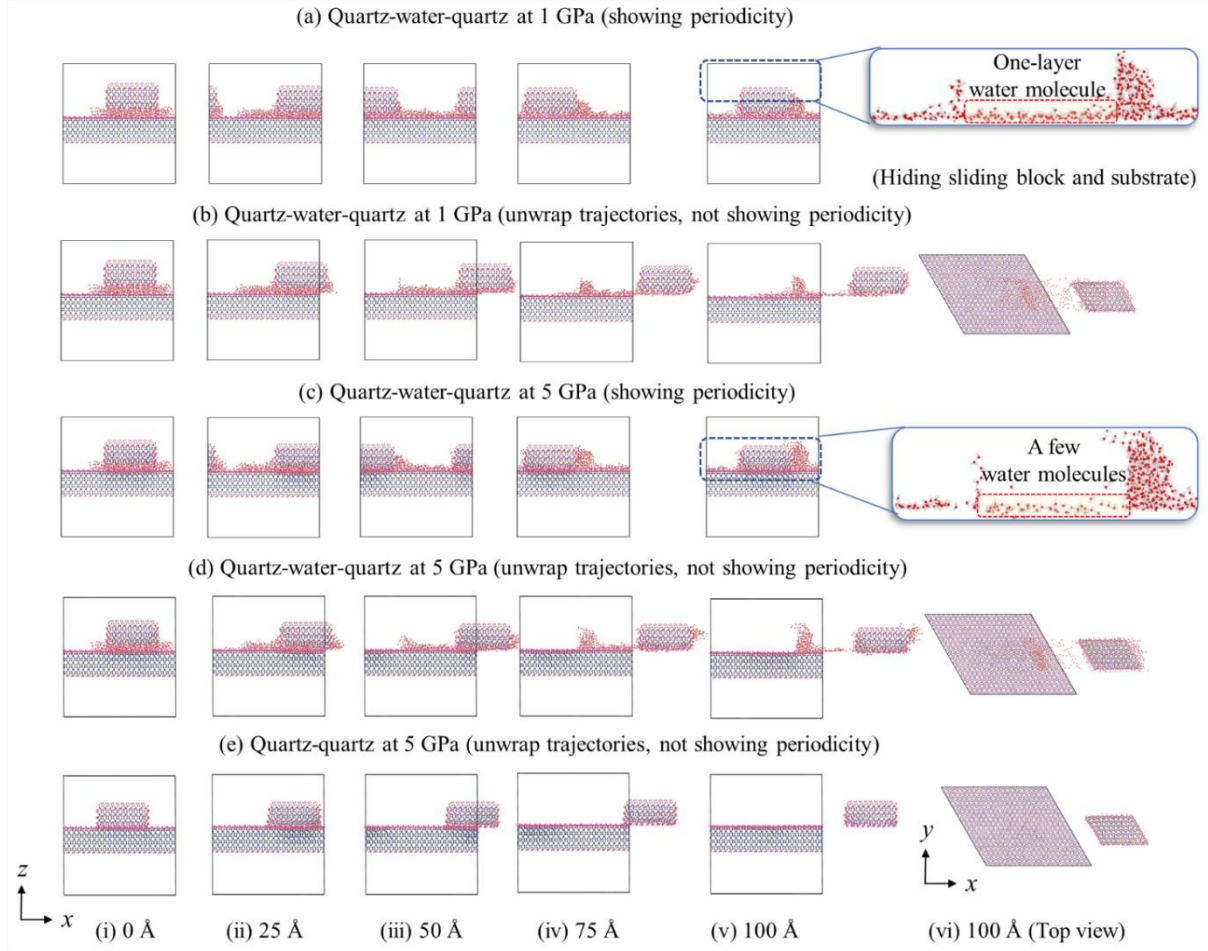

Figure 4-9. Trajectory diagram of quartz-water-quartz and quartz-quartz interface under different sliding distances and different normal loads: (a), (b) 1 GPa; (c), (d), (e) 5 GPa. The sliding velocity is 100 m/s and the temperature is 300 K.

Figure 4-11(a) shows the evolution of friction load with sliding distance for quartz-water-quartz interface under different normal loads, where the friction load increased slowly with rising sliding distance at 1 ~ 3 GPa. However, the friction load increased gradually at over 5 GPa; the higher the normal load, the faster the water film was discharged, causing a more significant increase in friction load.

In Figure 4-10(a) and (c), we compare the case of the normal load of 1 GPa and 5 GPa, a

one-layer water molecule for quartz-water-kaolinite interface, which always exists in the middle of sliding block and substrate during the friction process. Furthermore, compared to the evolution of friction load with sliding distance for quartz-water-quartz interface (Figure 4-11(a)), the increase rate of the friction load for quartz-water-kaolinite interface was relatively slow and stable with the increasing sliding distance, as displayed in Figure 4-11(b).
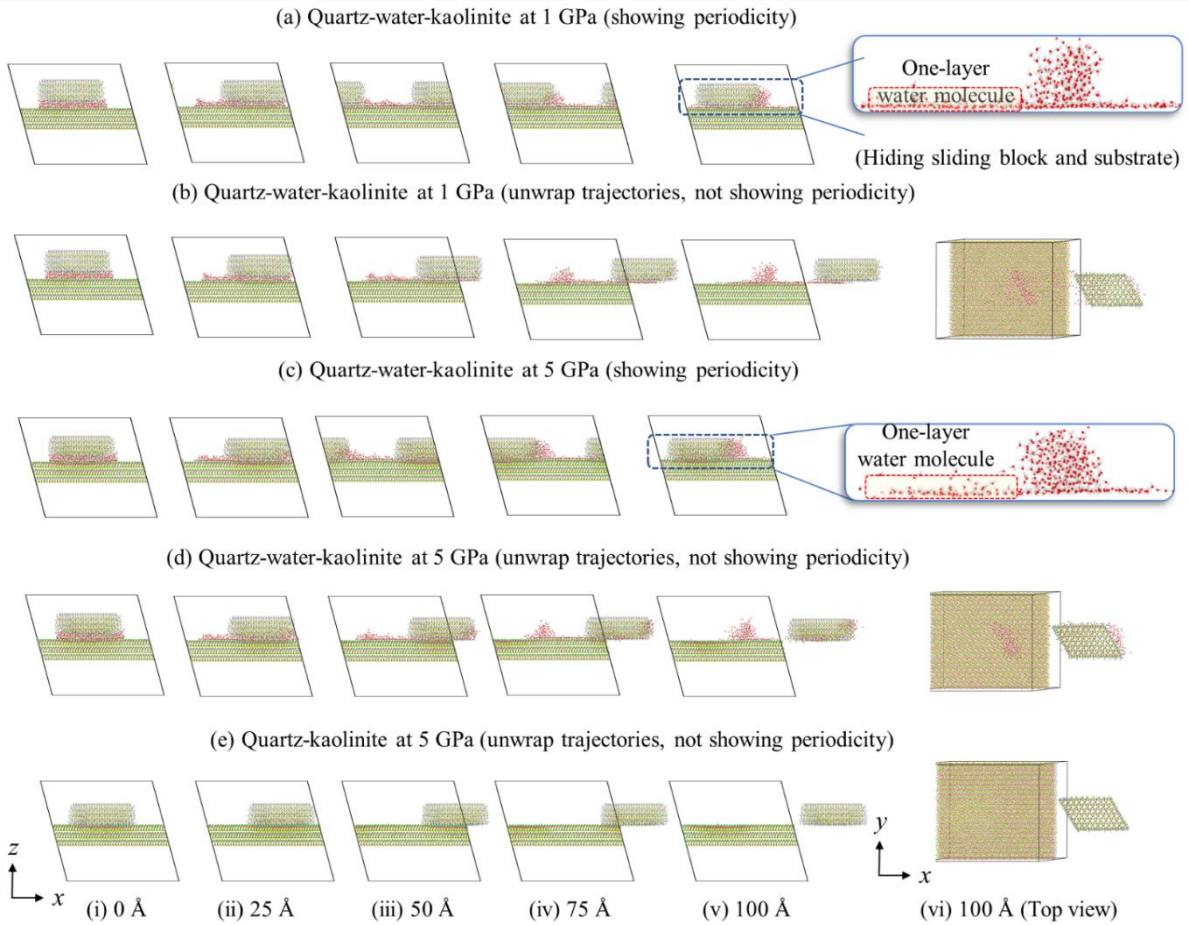

Figure 4-10. Trajectory diagram of quartz-water-kaolinite and quartz-kaolinite under different sliding distances and different normal loads: (a), (b) 1 GPa; (c), (d), (e) 5 GPa. The sliding velocity is 100 m/s and the temperature is 300 K.

As shown in Figure 4-11(d), it is worth noting that the friction coefficient of quartz-kaolinite interface (0.044) is less than that of quartz-water-kaolinite interface (0.084), indicating that interlayer water film for the friction between quartz and kaolinite might play a bonding role rather than a lubricating role. At the normal load of less than 3.8 GPa, the shear stress for quartz-kaolinite interface was superior to that for quartz-water-kaolinite interface. However, it was the

opposite at the normal load greater than 3.8 GPa. This finding was quite different from the friction properties between the quartz-water-quartz interface and quartz-quartz interface, where their friction coefficient was 0.094 and 0.27, respectively (see Figure 4-11(c)). On the other hand, the fluid lubrication at nanoscale was slightly different from that at macroscale, the formation of the ordered structure of the liquid, the increase of viscosity, or the surface tension could increase the friction strength between particles at nanoscale[155].

The friction properties of the solid particle with interlayer water film are complex, and need to be further studied. Based on the obtained results, we suggest that the water film should be spread over the whole substrate surface under a relatively low normal load, which could be better to explore the effect of various water layers on friction behavior.
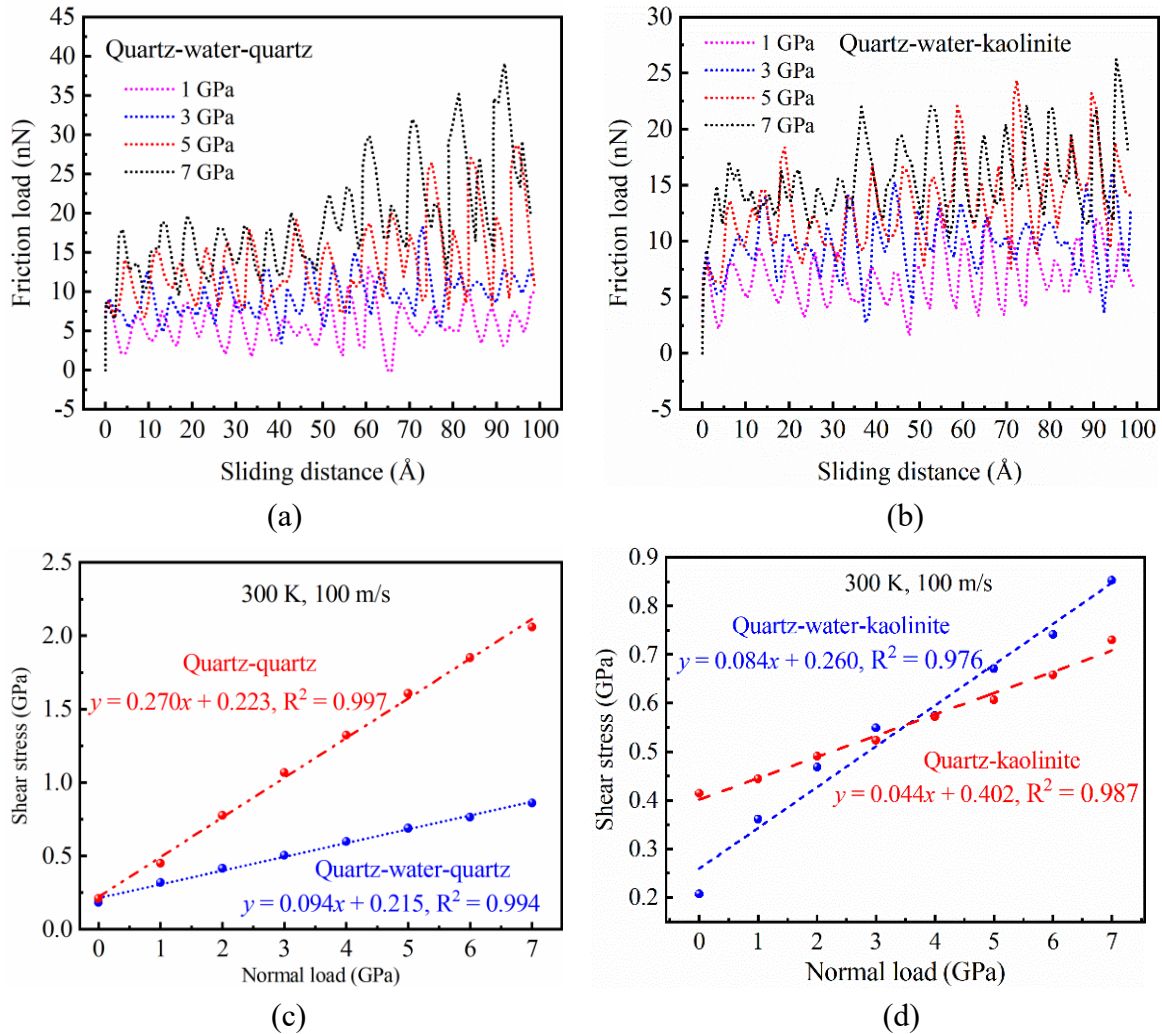

Figure 4-11. Evolution of friction load with sliding distance for (a) quartz-water-quartz interface and (b) quartz-water-kaolinite interface under different normal load. Evolution of shear stress with normal load for (c) quartz-water-quartz and quartz-

quartz interfaces, as well as (d) quartz-water-kaolinite and quartz-kaolinite interfaces. Moreover, the sliding velocity is 100 m/s, and the temperature is 300 K.

4.3.4 Stick-slip effect and relationship of shear stress and normal load

Figure 4-4(a), Figure 4-5(a), and Figure 4-11(a) display the influence of normal load, sliding velocity, and hydration on the stick-slip effect for quartz-(water)-quartz interface, respectively. The higher the sliding velocity and hydration, or the lower the normal load, the smaller the fluctuation amplitude of friction load, indicating the weaker the stick-slip effect. A similar result was also found in previous work [86].

Moreover, as was well known, the relationship between shear stress (or friction load) and the normal load for different materials was rather complex, including linear and nonlinear [14]. However, for nanoscale friction properties of soil or rock, we have found the relationship between normal load and friction load (shear stress) was approximately linear in this work (see Figure 4-4(b), Figure 4-6, Figure 4-7, Figure 4-8(c), Figure 4-11(c-d)) and previous studies [14, 86], where the degree of linear fitting is very high ($R^2 > 0.9$).

4.3.5 Effect of cation on friction behavior between quartz-montmorillonite interface

To investigate the influence of interlayer cations on the friction properties of quartz-montmorillonite system, eight different cations were considered in this work. The evolution of the shear stress with normal loads of all systems is shown in Figure 4-12, where their relationship is approximately linear.

The friction coefficient and cohesion of montmorillonite-quartz system with different interlayer cations are displayed in Figure 4-13 and Table 4-5. As shown in Figure 4-13 and Table 4-5, the order of friction coefficients for montmorillonite-quartz systems with different interlayer cations is $Ca^{2+} > Zn^{2+} > Ni^{2+} > Pb^{2+} > Li^+ > Rb^+ > Cs^+ > K^+$, illustrated that the friction strength of divalent cations system is greater than that of monovalent cations system. Moreover, the radius of divalent cations is generally less than that of monovalent cations. The higher the radius of cation, the lower the friction coefficient, and the higher the cohesion.

This study is focused on the interfacial friction of montmorillonite substrate and quartz slider, but there are inevitable differences between different substrate and slider materials. For example,

Sakuma et al. [20] studied friction behavior between two montmorillonite portions through DFT method, and found that the friction load increase with ionic radius, which was inconsistent with the results of this research. Thus, the nanotribology between two montmorillonite portions with different cations is needed to further study.
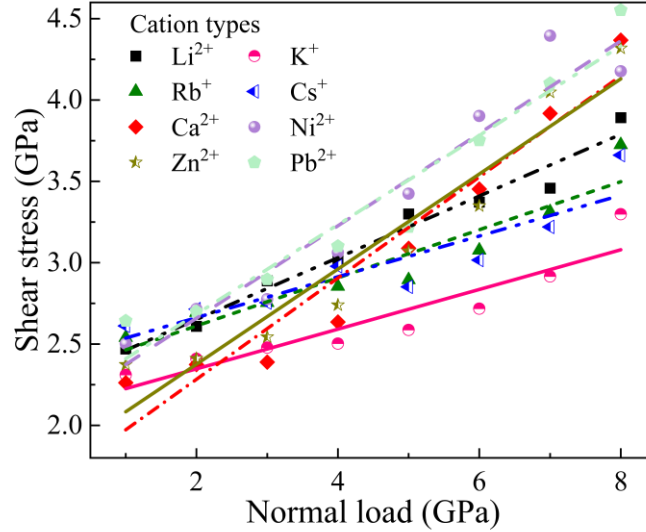

Figure 4-12. Evolution of shear stress with normal load for quartz-montmorillonite with different cations.
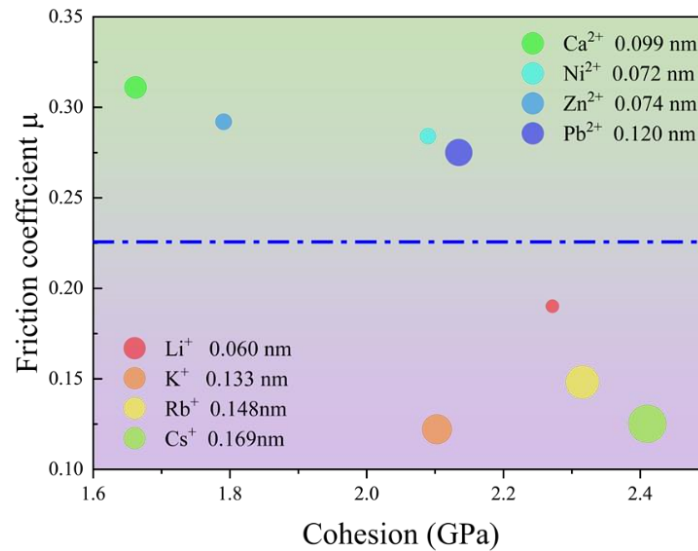

Figure 4-13. The relationship of ionic radius, friction coefficient (μ), and cohesion for quartz-montmorillonite with different cations, where the size of the circle represents the radius size of the corresponding cations.

Table 4-5 Friction properties parameters in terms of various cation genres

Cation type	Friction coefficient μ	Friction angle (°)	Cohesion force (GPa)	Ionic radius (nm)
Li^+	0.190	10.76	2.272	0.060
K^+	0.122	6.96	2.103	0.133
Rb^+	0.148	8.42	2.316	0.148
Cs^+	0.125	7.13	2.411	0.169
Ca^{2+}	0.311	17.28	1.662	0.099
Ni^{2+}	0.284	15.85	2.090	0.072
Zn^{2+}	0.292	16.28	1.791	0.074
Pb^{2+}	0.275	15.38	2.135	0.120

4.4 Conclusions

MD simulations with CLAYFF force field were performed to study the nanoscale friction behavior of quartz-quartz and quartz-kaolinite interface, considering different conditions of the normal load, sliding velocity, temperature, and hydration. The main conclusions were obtained as follows:

(1)　The stick-slip effect was found in the quartz-quartz interface during the friction process. The friction load periodically fluctuated around a stable value, where the wavelength was close to the lattice constant along the sliding direction. Moreover, the higher the sliding velocity and hydration, the lower the normal load, the weaker the stick-slip effect.

(2)　Concerning quartz-quartz interface, the friction load increased with the rising normal load, and the relationship between shear stress and normal load was approximately linear. Moreover, the friction coefficient and cohesion could rise with the increasing sliding velocity or the decreasing temperature.

(3)　The friction coefficient of quartz-kaolinite interface was significantly smaller than that of quartz-quartz interface. This is consistent with the previous experimental studies, where the presence of clay could weaken the frictional strength of quartz.

(4)　The friction coefficient of quartz-quartz interface was significantly greater than that of quartz-water-quartz interface; while one of quartz-kaolinite interface was smaller than quartz-water-kaolinite interface. Whether the interlayer water film plays a lubricating or bonding role

was found interesting, for which it is suggested that the water film should be spread over the whole substrate surface under a relatively low normal load.

(5) The order of friction coefficients for montmorillonite-quartz systems with different interlayer cations is $Ca^{2+} > Zn^{2+} > Ni^{2+} > Pb^{2+} > Li^+ > Rb^+ > Cs^+ > K^+$. Moreover, the higher the radius of cation, the lower the friction coefficient, and the higher the cohesion.

This work provides new fundamental insights into the friction behavior in rock or soil engineering, and extends the friction properties of quartz from macroscopic scale to nanoscale.

Chapter 5

Phase Transformation of Ice-Unfrozen Water on Montmorillonite Surface: A Molecular Dynamics Study

Chapter 5. Phase Transformation of Ice-Unfrozen Water on Montmorillonite Surface: A Molecular Dynamics Study [III]

Abstract

The phase transformation process and composition distribution of unfrozen water and ice on the surface of expansive soil minerals in microscale are still unclear in frozen soil. The phase transformation and composition behavior of ice-water onto montmorillonite interface as well as its surface effect at supercooled temperature (230 ~ 270 K) were investigated for the first time through molecular dynamic (MD) simulation method, considering their interfacial, structural, and dynamic properties. The evolution of unfrozen water content with temperature in MD simulation agreed well with that in the NMR experiment for validation and comparison. The simulation results showed that 1) some ice could transform unfrozen water as the temperature rose due to thermal fluctuations causing the breakage of hydrogen bonds; 2) combining with the simulation results in this work and electrical double layer theory, a new division of microstructure of unfrozen water and ice onto montmorillonite was proposed and determined, which was "montmorillonite-bound water-cubic ice-hexagonal ice-cubic ice-'quasi-liquid' water-air"; 3) the surface effect of montmorillonite was an important reason for the existence of unfrozen water in frozen soil, especially coulomb electrostatic interaction. Furthermore, the structure and dynamic properties of unfrozen water and ice were discussed.

Keywords: Montmorillonite; Unfrozen water; Water-ice phase transformation; Surface effect; Molecular Dynamics

---

[III] This chapter is based on the following paper: Wei, P., Zheng, Y., Zaoui, A., et al. Phase Transformation of Ice-Unfrozen Water on Montmorillonite Surface: a Molecular Dynamics Study. 2023. (Under review).

Wei P., Zheng Y., Liu Y. Molecular dynamics simulation study on the ice water phase transition characteristics at montmorillonite surface [C] The Third Academic Conference on Civil Engineering Calculation and Simulation Technology Nanning, Guangxi, May 14, 2023. (In Chinese)

5.1 Introduction

Expansive soil is mainly composed of strong hydrophilic clay minerals such as montmorillonite, which has significant deformation characteristics of water absorption expansion and water loss shrinkage [156]. In addition, lots of expansive soil in seasonal frozen soil regions in China are subjected to freeze-thaw cycles, in addition to the conventionally encountered drying-wetting cycles [26], easily causing engineering problems such as frost heaving or melting deformation. Expansive soil in seasonal frozen regions is a four-phase system, containing soil particles, ice, unfrozen water, and air. And the transformation between ice and unfrozen water is significantly affected by temperature, resulting in the changing of physical and mechanical properties of frozen soil, and finally causing engineering disaster. Therefore, the complexity of ice-water phase transformation in frozen soil is one of the main reasons for the complexity and particularity of mechanical properties of frozen soil, and needs to be investigated.

The phase transformation of ice-water is related to the temperature, pressure, microstructure and composition of soil particles, and there are coupling relationships between these factors with varying degrees. So far, the unfrozen water content has been used as the primary index to measure the degree of ice-water transformation in soil, considering many other influencing factors. Some scholars studied the freezing characteristics of soil under different saturation [157], and the relationship between unfrozen water content and freezing temperature [28] using Nuclear Magnetic Resonance (NMR). Kozlowski et al. [158] found that ice melting in soil was not a continuous phase transformation through the calorimetry method. Liu et al. [159] determined the calculating formula between the mass and heat absorption of ice, and then calculated the unfrozen water content. To sum up, the experimental methods mentioned above were well employed to measure the unfrozen water content in unsaturated frozen soil, but it was difficult to observe this physical process and reveal the microscopic mechanism of phase transformation of ice-water.

On the other hand, the particle size of clay minerals is very small, and it has a layered

structure and complex surface properties, such as a double electric layer. Thus, it is challenging to directly use physical test methods to study the above microscopic mechanisms of phase transformation of liquid water-ice and the migration of unfrozen water in expansive soil minerals [29]. At the same time, it is difficult to prepare samples and requires special experimental equipment, such as nanoindentation and atomic force microscope experiments, etc. [31]. Therefore, other methods are needed to study the phase transformation process of ice-water onto montmorillonite.

With the rapid development of computer technology, finite element and discrete element methods are commonly used in geotechnical and geological engineering, while they have some limitations when dealing with small-scale (micro- and nano-scale) geotechnical problems and explaining some mechanism problems [34, 35]. However, in the past decades, molecular dynamic (MD) simulation method has become an excellent tool suitable for solving specific problems in materials science, and has been widely used to study the interface characteristics, thermodynamic behavior, and multi-medium interaction of geotechnical materials at microscale [36-38].

The phase transformation of ice-water is a complicated scientific problem. Since the end of 19th century, the solid-flow transformation of water has been studied. Many ice wind tunnel experiments in macroscopic scale [160] have been carried out over the past 100 years, but no breakthrough results have been obtained on the mechanism of ice-water phase transformation. Recently, many scholars explored the phase transformation process of ice-water in microscale through quantum mechanics, MD, Monte Carlo methods, where MD simulation was the most widely employed. For example, Matsumoto et al. [161] successfully simulated the freezing process of pure water for the first time through MD simulation, and found that the nucleation of ice was manifested as enough hydrogen bonds with relatively long existence time spontaneously forming relatively compact initial nuclei in the same position. Sanz et al. [162] simulated the uniform nucleation of ice and calculated the critical cluster size and nucleation rate for the first time. Lupi et al. [163] used mW water model to study heterogeneous nuclei of

ice through MD simulation, and reported the freezing process of water near the ice-water interface, but did not elaborate on the role of interface water in ice nucleation mechanism. Jessica et al. [164] investigated the crystallization process of ice based on mW water model. Benet et al. [165] studied the ice-water interface using TIP4P/2005 water model and obtained the value of directional mean interface free energy. Zhang et al. [166] proposed an effective method to calculate the energy of ice-water mixing system for ice-Ih crystals through MD simulation, which was expected to be used to simulate the phase transformation process of ice crystals. Bai et al. [167] recently studied the ice nucleation process in water droplets of graphene oxide nanosheets, providing experimental information for the existence of critical ice nuclei. The studies mentioned above mainly discussed the phase transformation process of ice-water in a pure water system.in frozen soil engineering, the ice-water phase transformation of expansive soil in frozen soil regions involved soil-unfrozen water-ice-air system. Therefore, the phase transformation of ice-water at the interface of expansive soil minerals should be more concerned.

At present, the theoretical explanations for the existence of unfrozen water in frozen soil included capillary action, surface effect, adsorption force, and double electric layer effect. Jin et al. [168] further demonstrated through theoretical analysis that the surface effect of clay was the main reason for unfrozen water existing in frozen soil. Sosso et al. [169] studied the heterogeneous ice nucleation process on kaolinite surface at 230 K using TIP4P/ICE water model in MD simulation, and pointed out that the surface properties of kaolinite were very sensitive to the ice nucleation process. At the strong supercooling temperature of 230 K, the ice formation rate was 20 orders of magnitude faster than that of homogeneous freezing due to kaolinite [170]. Cox et al. [171] analyzed the ice nucleation process between homogeneous and heterogeneous (kaolinite as ice nucleating agent) using TIP4P/2005 water model at 220 K, and Zielke et al. [172] explored heterogeneous ice nucleation on two different surfaces of kaolinite using TIP4P/ICE water model at 230 K, where they both found that kaolinite could significantly increase the rate of ice nucleation. Moreover, compared to montmorillonite and illite, Mason

[173] verified that kaolinite was the most effective and essential ice-nucleating mineral through experiments. Zhang et al. [27] firstly analyzed the phase composition behavior of frozen soil and phase transformation of water in mineral nanopore using mW model at 100 ~ 260 K in MD simulation; and found that the complex interaction between adsorption and capillary action existed in the soil surface; and reported that the physical mechanism of frozen soil phase composition curve in low temperature region was very complicated.

To sum up, most of the above studies focus on ice nucleation at kaolinite interface at supercooled temperature (220 ~ 230 K) [169-172, 174]. However, the surface effect and structural composition of montmorillonite are very different from that of kaolinite, and the phase transformation behavior of ice-water at the interface of montmorillonite is still unknown. Therefore, in this work, the phase transformation and composition behavior of ice-water onto montmorillonite surface and its surface effect in nanoscale are revealed for the first time. This work provides a theoretical basis for macroscopic characterization of the phase transformation law of ice-water in expansive soil minerals, and establishes the "micro-macro" theoretical connection in frozen soil mechanics.

5.2 Computational details

5.2.1 System setup and force field

The unit model of ice-Ih was derived from Bernal et al. [175], which has a hexagonal symmetry with a space group of $P6\_3cm$, including five water molecules and then forming an open tetrahedral crystal cell [176]. The orthogonal ice-Ih system was built, including 12096 atoms (Figure 5-1(a)). The Wyoming-type montmorillonite model was derived from Viani et al.[91], and its chemical formula was $Na_{0.75}(Si_{7.75}Al_{0.25})(Al_{3.5}Mg_{0.5})O_{20}(OH)_4 \cdot nH_2O$. The supercells of montmorillonite are composed of 112 unit cells ($8a \times 7b \times 2c$), as shown Figure 5-1(b). Finally, the bulk montmorillonite and ice system were merged into montmorillonite-ice (Mt-ice) system (Figure 5-1(c)), where its contact surface was their (001) surface. As shown in Figure 5-1(c), the atoms layer of around 4 Å at the bottom of montmorillonite substrates were fixed as an

immovable fixed layer to ensure the stability of the substrate without displacement. It was worth noting that the ice-vacuum interface could be used to simulate the ice-air interface in MD simulation [177]. Because the number of air molecules in the model system was very little during the simulation, this treatment without considering air molecules in the simulation did not affect the simulation conclusion [178].
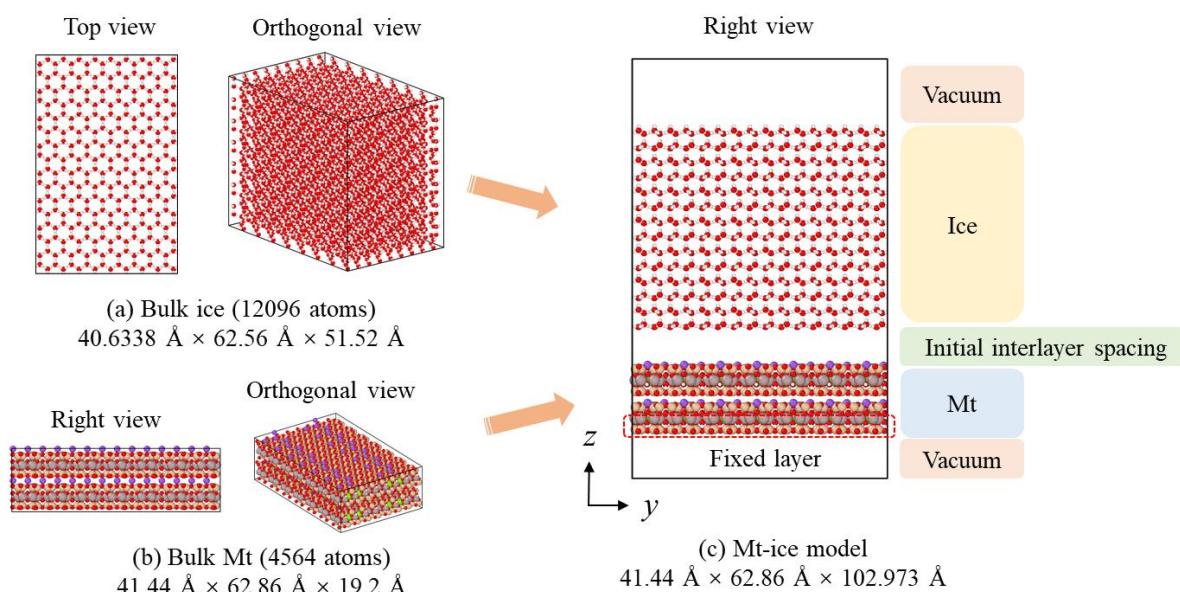

Figure 5-1. Montmorillonite-ice (Mt-ice) model using in this work: (a) Bulk ice model; (b) Bulk montmorillonite (Mt) model; (c) Initial Mt-ice model with initial interlayer spacing of 10 Å.

CLAYFF[52] force field has been widely used to describe the interaction of clay minerals in MD simulation[14, 15, 54, 55], so it was also applied in this work. The non-bonded and bonded interaction parameters of the CLAYFF force field were derived from the literature[52], as shown in Table 2-4. Moreover, TIP4P/ICE [59] water model could reproduce many structural and dynamical properties of different ice phases and liquid water correctly, and has been well employed to explore the ice formation onto kaolinite [169, 170, 172]. Meanwhile, its melting temperature of 270 ± 3 K obtained by previous works [179, 180] was close to the experiment value of 273 K. Therefore, the TIP4P/ICE rigid water model controlled by the SHAKE method was

used to describe the water and ice system in this work, where its potential parameters were shown in Table 2-6. Furthermore, the four-point TIP4P/ICE rigid water model extends the traditional three-point water model (like SPC, SPC/E, TIP3P, etc.) by adding an additional site M, usually massless, where the charge associated with the oxygen atom is placed. This site M is located at a fixed distance away from the oxygen along the bisector of the HOH bond angle[50].

5.2.2 Relaxation and simulation details

All MD simulations were performed in LAMMPS[50] code. Three-dimensional periodic boundary condition was applied in the simulations. The van der Waals forces was calculated using the Lennard-Jones potential model with the cut-off radius set as 10 Å. The Velocity Verlet algorithm was applied to integrate the motion equations. Long-range electrostatic interactions with a cut-off radius of 8.5 Å were calculated using the PPPM/TIP4P method. The time step in whole simulations was set to 1.0 fs.

As shown in Table 5-1, the simulation process in this study was performed as following steps: 1) to obtain a sufficient equilibrium configuration, the conjugate gradient method was used to do the energy minimization for ice and montmorillonite separately, and then merging these two models into Mt-ice system with an initial interlayer spacing of 10 Å. 2) To obtain the most stable model (i.e., the lowest energy model), nine Mt-ice models with different interlayer spacings of 2 ~ 10 Å were established by adjusting its interlayer spacing. 3) the temperature of nine Mt-ice models in the canonical (NVT) ensemble increased from 0 to 270 K for 100 ps, followed by equilibrated in 270 K for 100 ps. As shown in Figure 5-2, the average total energy of Mt-ice system with initial interlayer spacing of 6 Å is the lowest, indicating that this model is the most stable one. Thus, this model was used in this work. 4) The Mt-ice system with initial interlayer spacing of 6 Å was equilibrated with NVT ensemble in 0 K for 1.0 ns, and the initial Mt-ice system gradually translated into montmorillonite-water-ice (Mt-water-ice) system. 5) Thereafter, the temperature of Mt-water-ice system rose from 0 to 270 K for 1.08 ns, where a restart file was saved and printed every 10 K during heating process. 6) Finally, based on step 5, five different Mt-water-ice model under different temperatures (230 ~ 270 K) were further

relaxed in NVT ensemble at their target temperature for 100 ns, where 270 K was in the melting temperature range of TIP4P/ICE water model, and 230 ~ 240 K were its supercooled temperature. 7) To further balance the ice-water phase transformation in whole system, the Mt-water-ice system at 230 ~ 250 K were further relaxed in NVT ensemble for 50 ns.
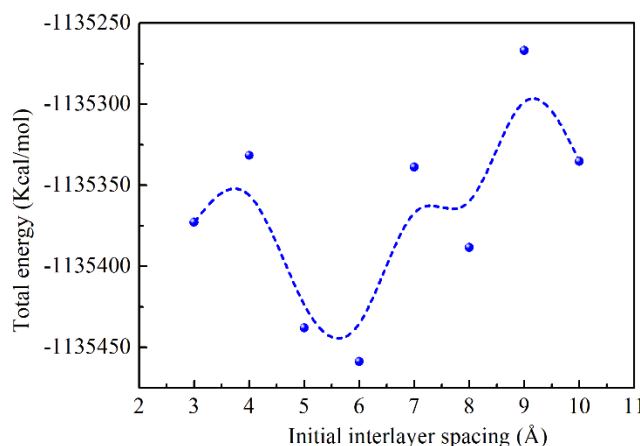

Figure 5-2. Evolution of average total energy of ice-water system with different initial interlayer spacing at 270 K, where the average total energy was obtained over the later 50 ps. Moreover, the initial interlayer spacing was the distance between top surface of clay and bottom surface of ice.

Table 5-1. MD simulations schemes in this work.

Step	Equilibrium (Equi.) and running process	
1	Minimize and merge two models	Minimize with conjugate gradient (CG) algorithm for ice and Mt system, respectively, followed by merging the ice and Mt model into initial Mt-ice model with initial interlayer spacing of 10 Å.
2	Adjusting the interlayer spacing	Adjusting the interlayer spacing of Mt-ice system, so that obtained nine Mt-ice models with different interlayer spacings of 2 ~ 10 Å.
3	Equi.1	(a) NVE + Langevin (rising temperature from 0 to 270 K), 100 ps; (b) NVE + Langevin (270 K), 100 ps. Compared the evolution of total energy with different interlayer spacing to obtain the most stable model.
4	Equi.2	NVE + Langevin (0 K), 1.0 ns (the most stable model with initial interlayer spacing of 6 Å) (Noting: Based on step 2, not step 3. Total process: step 1-2-4)
5	Equi.3 with rising temperature	NVE + Langevin (rising temperature from 0 to 270 K), 1.08 ns

6	Equi.4 at target temperatures	NVE + Langevin (at target temperature of 230, 240, 250, 260, and 270 K), 100 ns
7	Equi.5 at target temperatures	NVE + Langevin (at target temperature of 230, 240, and 250 K), 50 ns

5.2.3 Experiment control group

In our latest experimental research [28], the unfrozen water characteristics of unfrozen soil at ultralow temperatures from 193 ~ 293 K were studied by Newmark cryogenic nuclear magnetic resonance (NMR) (Figure 5-3(a)). The soil sample used in the experiment was clay, where its main component was clay minerals, quartz, feldspar, and potassium feldspar. A cylindrical sample with a water content of 20 % and dry density of 1.7 g/cm^3 was made, and its dimension was 20 mm × 60 mm (diameter × height), shown in Figure 5-3(b).

In this work, to establish the "macroscopic - microscopic" connection of frozen soil, the macroscopic experimental results during 223 ~ 283 K in our previous literature [28] was employed as control group, and discussed with MD simulation results (see Section 3.2.2).
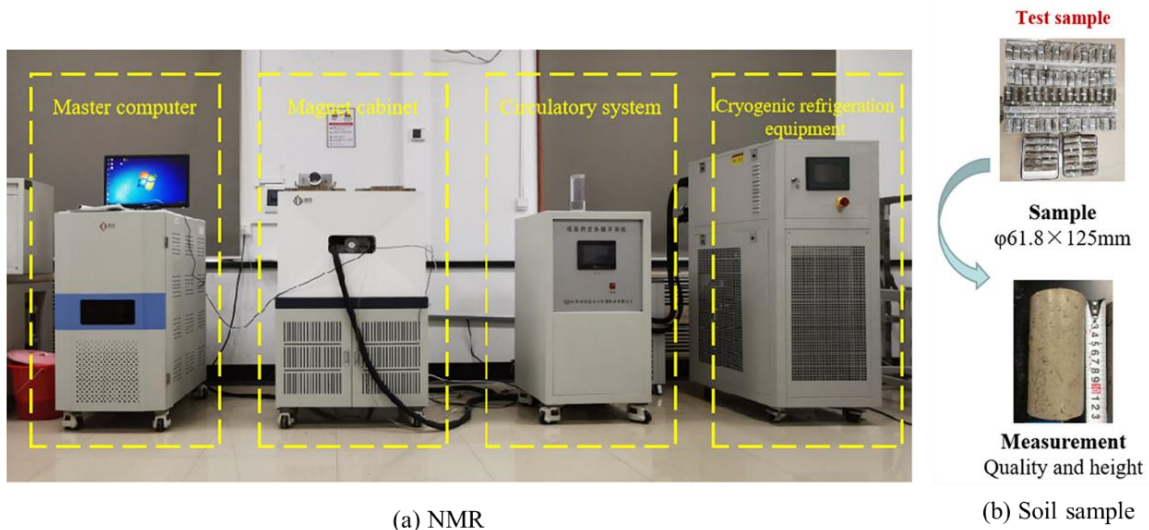

(a) NMR   (b) Soil sample

Figure 5-3. (a) Newmark cryogenic nuclear magnetic resonance (NMR) imaging analyzer and (b) soil sample used in experiments. [28]

5.3 Results and discussions

The simulation results during heating process from 0 to 270 K were presented in section 5.3.1. The simulation results at melting and supercooled temperatures of ice-Ih (230 ~ 270 K) were presented in Section 5.3.2 ~ 5.3.4, including the interfacial properties and phase composition, structural analysis, as well as dynamic properties of Mt-water-ice system.

5.3.1 Evolution of montmorillonite-water-ice system during heating (0 ~ 270 K)

Based on the step 4 and 5 in Table 5-1, the structural evolution of montmorillonite-ice system during heating process (0 ~ 270 K) was illustrated in Figure 5-4. As shown in Figure 5-4(b) and (c), the initial Mt-ice system gradually translating into Mt-water-ice system was developing, where a little ice molecule contacting the clay surface changed into disordered water molecules in 0 K during 0 ~ 1000 ps. Thereafter, more and more hexagonal ice molecules transformed into water molecules in heating stage (0 ~ 270 K) during 1000 ~ 2080 ps, resulting in the increase of F_3 (Figure 5-4(a)). However, it was noted that the number of interfacial ice molecules gradually rose with increasing temperature, and that of cubic ice molecules was unchanged. Moreover, as shown in Figure 5-4(a), during heating process, the total energy of the whole system increased with increasing temperature, illustrating that this is a process of absorbing energy for the transformation of ice to water.

It was worth noting that the ice near the clay surface was the first to transform into disordered water during 0 ~ 6 ps (Figure 5-4(c)), owing to the surface effect of montmorillonite, such as Van der Waals and electrostatic interaction. Therefore, the number of water molecules and order parameter F_3 suddenly rose, while that of hexagonal ice molecules rapidly reduced. On the other hand, the F_3 for initial Mt-ice model was equal to 0.038, not zero, because this bulk ice in Mt-ice system was not on a three-dimensional periodic boundary, where its upper surface was in contact with the vacuum layer, and its lower surface was in contact with the clay mineral layer.
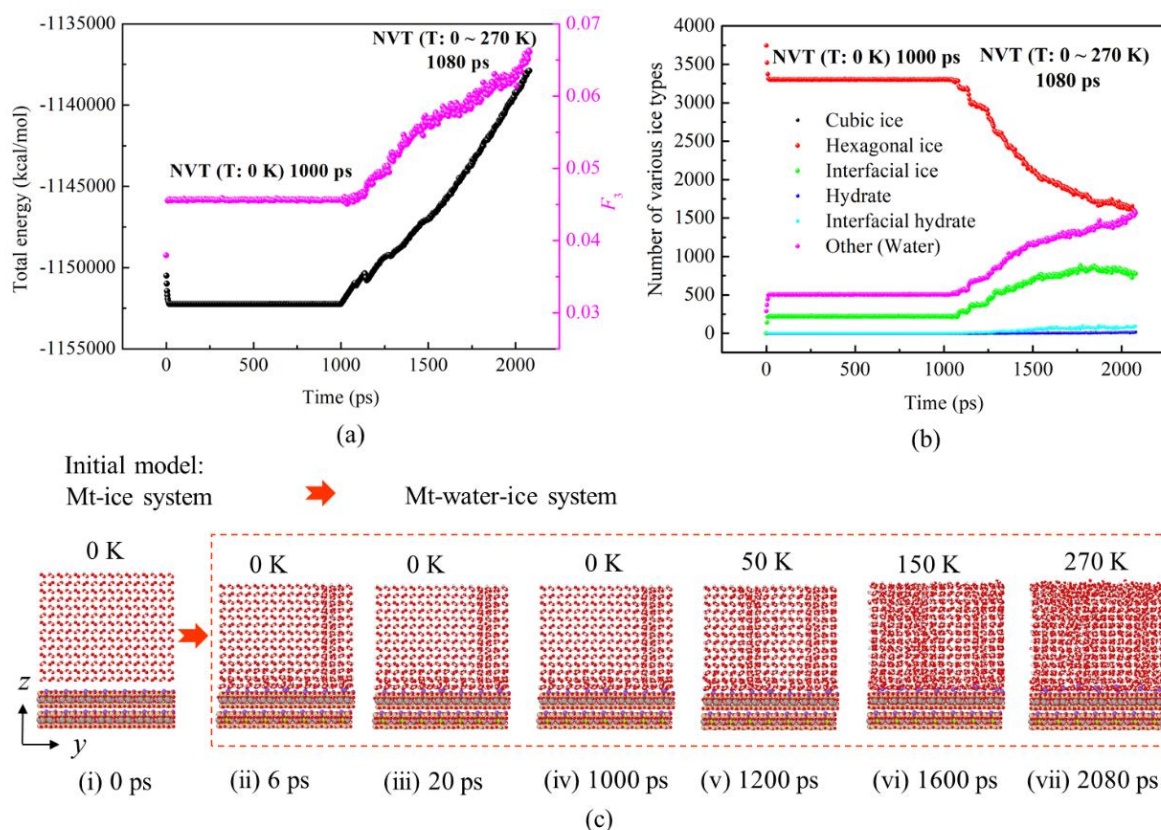
Figure 5-4. Evolution of (a) total energy of whole Mt-(water)-ice system and F_3, (b) number of various ice types, and (c) structural configuration of the whole system with time during heating process (0 ~ 270 K), where the temperature of the whole system is set as 0 K for the first 1000 ps, and then increased from 0 K to 270 K for the latter 1080 ps.

5.3.2 Interfacial properties and phase composition

5.3.2.1 Ice-water phase transformation process

To explore the effect of temperature on the ice-water phase transformation in Mt-water-ice system, Figure 5-5 displays the evolution of the number of various ice types with time under different target temperatures. As shown in Figure 5-5(a-c), at 230 ~ 250 K, the hexagonal ice molecules constantly increase with time, while the case of water and interfacial ice molecules are opposite. It was worth noting that their trend of the transformation of water into ice was still developing after 100 ns, indicating that the liquid water in Mt-water-ice system could further transform into hexagonal ice (Figure 5-6(a-c)). Thus, compared with that cases of 260 and 270 K, the Mt-water-ice system at 230 ~ 250 K was needed to equilibrate for further 50 ns.

As shown in Figure 5-5(d), at 260 K, the number of liquid water increase firstly in 0 ~ 5 ns, followed by constantly decrease in 5 ~ 50 ns, finally keep stable in 50 ~ 100 ns, illustrating that the whole system reaches a relatively stable stage (Figure 5-6(d)). However, the evolution of hexagonal and cubic ice with time was opposite to that of liquid water. Furthermore, the evolution of the transformation of water into hexagonal and cubic ice at 270 K was somewhat similar to the case at 260 K (Figure 5-5(e)).

To explore the ice-water phase transformation process at 270 K during 0 ~ 100 ns, Figure 5-6(e) shows the ice-water structure under different times in 270 K. As shown in Figure 5-5(e) and Figure 5-6(e), plenty of ice molecules near clay and vacuum layers constantly transform into water molecules in 0 ~ 25 ns. Thereafter, the upper and lower portion water gradually translated into hexagonal and cubic ice in 25 ~ 50 ns, and then a little water molecule continued to transform into cubic ice molecules in 50 ~ 100 ns, where the number of the hexagonal ice molecules kept unchanged in 40 ~ 100 ns.
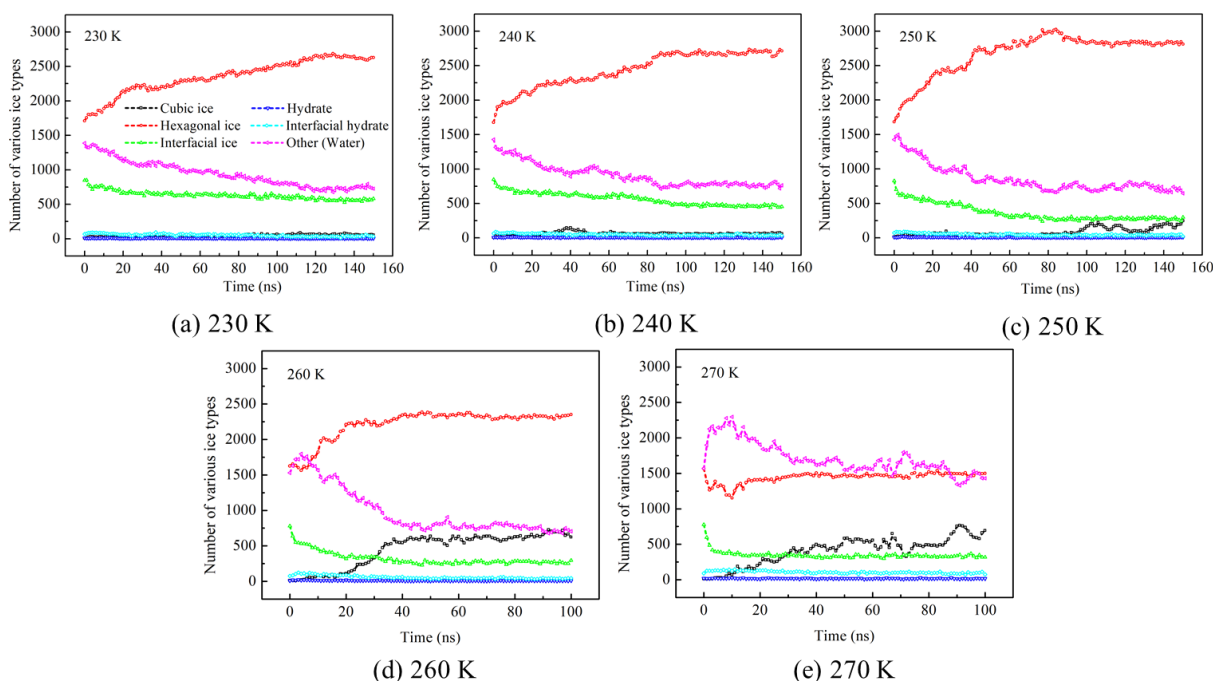

Figure 5-5. Evolution of number of various ice types in montmorillonite-water-ice system with time under different temperatures: (a) 230 K, (b) 240 K, (c) 250 K, (d) 260 K, and (e) 270 K.

On the other hand, as shown in Figure 5-6 and Figure 5-7, the water-ice system onto montmorillonite surface could be mainly divided into three zones: 1) zone i contains liquid water near the clay layer with a certain thickness with 3.0 ~ 6.0 Å. Zhang and Pei [93] studied the thickness of bound water in Na-montmorillonite pore using MD simulation, which was determined as about 6 Å (containing two water layers) regarded as tightly bound water after verifying by experimental data. Wang et al. [181] also reported the thickness of bound water in montmorillonite as 3.1 ~ 10.65 Å corresponding to a relative humidity of 10 % ~ 100% through experimental method. Therefore, the liquid water in zone i was determined as bound water. 2) zone ii mainly includes hexagonal and cubic ice, maintaining the crystal structure. 3) zone iii mainly contains disorder liquid water near the vacuum layer. Moreover, the unfrozen water often mentioned in frozen soil engineering is liquid water in soil-water-ice system, which is made up of bound water in zone i and disorder liquid water in zone iii.
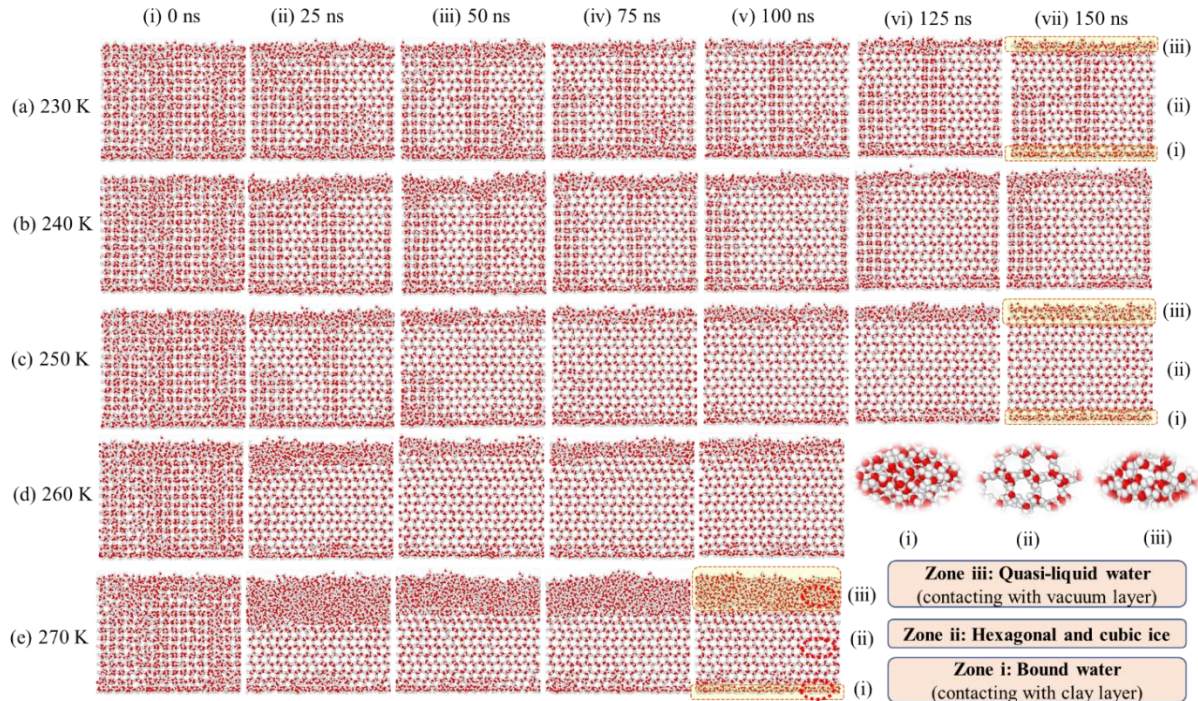

Figure 5-6. Evolution of ice-water structure in montmorillonite-water-ice system with time under different temperatures: (a) 230 K, (b) 240 K, (c) 250 K, (d) 260 K, and (e) 270 K. Note: the montmorillonite system is hidden for better visual clarity.

To understand the proportion of each component in whole system, based on the transformation evolution of ice and water (Figure 5-5), Table 5-2 shows the average number of various types of ice, hydrate, and water at different temperatures in the stable stage. Among these, the stable stage corresponded to the last 20 ns (130 ~ 150 ns) at 230 K, as well as the last 50 ns at 240 ~ 250 K (100 ~ 150 ns) and 260 ~ 270 K (50 ~ 100 ns). Thereafter, the evolution of average number of total ice (containing cubic, hexagonal, and interfacial ice), liquid water, and total hydrate (including hydrate and interfacial hydrate) with temperature could be displayed in Figure 5-7(f). As shown in Figure 5-7, as the temperature rises, the thickness of bound water in zone i and disorder liquid water in zone iii gradually increase, while that of total ice layer decreases. Moreover, as shown in Table 5-2, the total ice and total liquid water number changed slightly at 230 ~ 260 K, where hexagonal and interfacial ice could transform into cubic ice. However, at 260 ~ 270 K, the total ice and total liquid water changed exponentially, where plenty of hexagonal ice and little cubic ice mainly transformed into liquid water.

Table 5-2. Average number of various types of ice, hydrate, and water under different temperatures, where the data of the last 20 ns (130 ~ 150 ns) is averaged at 230 K, and the data of the last 50 ns is averaged at 240 ~ 250 K (100 ~ 150 ns) and 260 ~ 270 K (50 ~ 100 ns).

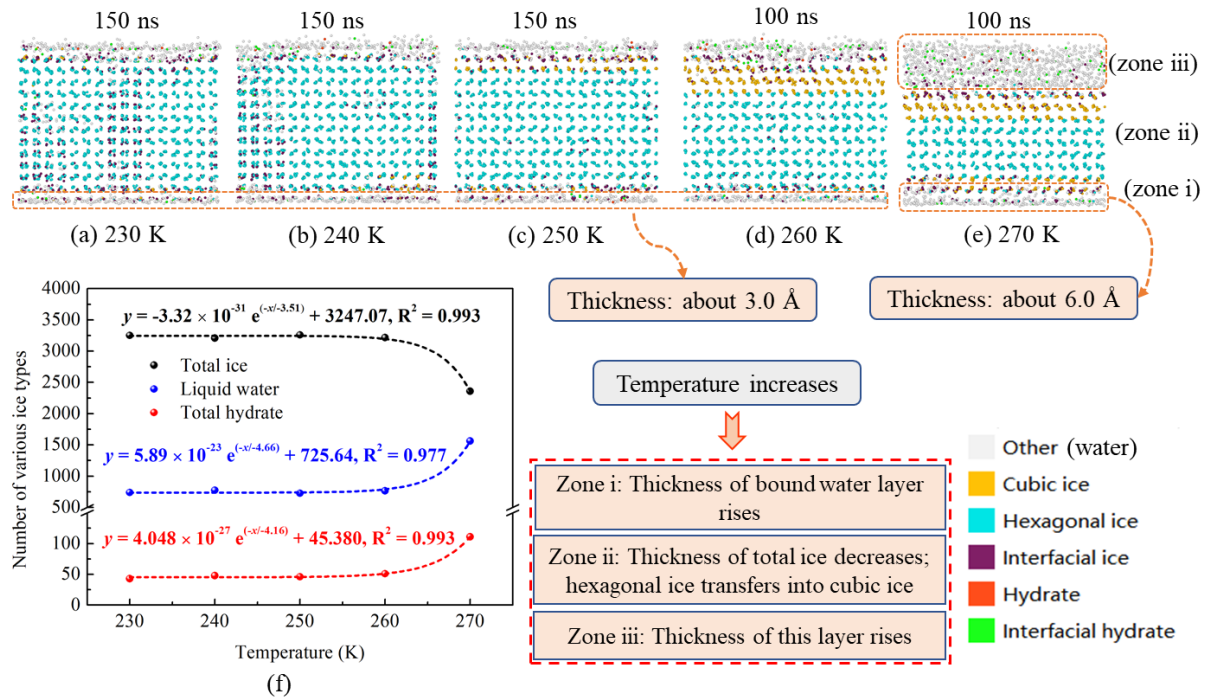| Temperature (K)	Cubic ice	Hexagonal ice	Interfacial ice	Hydrate	Interfacial hydrate	Other (liquid water)
230	59	2630	562	5	37	739
240	58	2684	467	6	42	775
250	154	2828	278	6	40	727
260	622	2327	267	7	44	765
270	547	1479	332	16	95	1563

Figure 5-7. (a-e) Ice-water structure onto montmorillonite surface at the end of simulations under different temperatures (230 ~ 270 K). Moreover, (f) evolution of average number of total ice (containing cubic, hexagonal, and interfacial ice), liquid water, and total hydrate (including hydrate and interfacial hydrate) with temperature, where these data sums are based on the data in Table 5-2. Note: the montmorillonite system is hidden for better visual clarity.

As shown in Figure 5-8(a) and Figure 5-5, we could conclude that the transformation of ice to water is an absorbing energy process, but the transformation of water to ice is a releasing energy process. Matsumoto et al. [182] also verified that this is a releasing energy progress when the water molecules transformed into ice molecules. Moreover, as shown in Figure 5-8(b), the order parameter F_3 gradually reduces with rising time in 230 ~ 250 K; while F_3 increases firstly, followed by decreases in 260 and 270 K. It was consistent with the evolution of water with time (Figure 5-5). Moreover, the value of F_3 during 50 ~ 100 ns in 230 ~ 260 K was much similar, indicating that the number of ice and water molecules of Mt-water-ice system in this stage were very close. However, the F_3 during 40 ~ 100 ns in 270 K was higher than 0.07, and significantly greater than the cases in other supercooled temperatures.
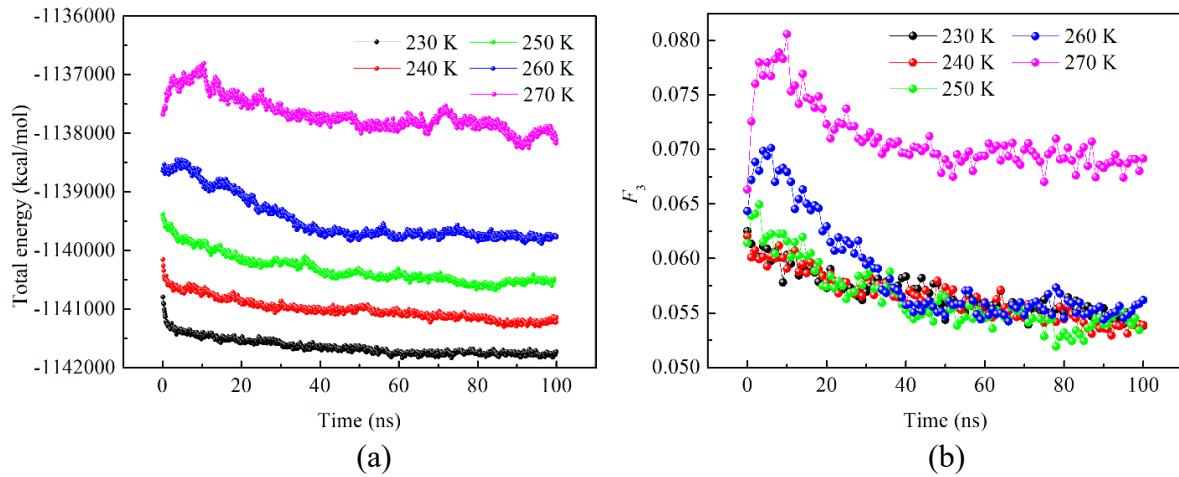
Figure 5-8. Evolution of (a) total energy and (b) F_3 of Mt-water-ice system with time, respectively.

5.3.2.2 Bound water

Why does bound water in zone i (or unfrozen water) exist in frozen soil? Currently, the presence of unfrozen water in frozen soil through theoretical explanations is attributed to capillary action, surface effect, adsorption forces, and the electrical double layer. Based on theoretical derivation, Jin et al. [168] reported that the surface effects of clay was the main influence factors, and adsorption forces acting on the residual unfrozen water close to the clay particle surface are the combination of van der Waals forces, valence forces, and electrostatic forces. However, their respective percentages are unknown. Besides, the work of adhesion is defined as a work required to separate two phases from each other, and used to analyze the contribution ratio of each component to work of adhesion in this work. As shown in Table 5-3, the contribution of coulomb electrostatic force in the surface effect is the largest, followed by van der Waals force, and the last is bond interaction. Therefore, it could be concluded that the presence of unfrozen water in frozen soil was mainly due to the surface effect of clay, including coulomb electrostatic and van der Waals interaction, where coulomb electrostatic interaction was the main influencing factor.

97

Table 5-3. Obtained contributions to the work of adhesion (mJ/m^2) deduced from the energy differences between Mt-water-ice system and water-ice film in 270 K.

Time (ns)	VDW	Coulomb (short-range)	Coulomb (long-range)	Bond	Total
0	-8.098	-1621.078	2111.593	0.284	482.700
5	-4.442	-1564.181	2168.330	0.728	600.435
10	-15.453	-1574.021	2193.231	1.149	604.906
20	-36.524	-1545.680	2165.778	1.335	584.909
50	-8.530	-1632.559	2118.189	1.403	478.504
75	-51.338	-1591.957	2135.247	-3.098	488.854
100	-44.598	-1598.816	2136.521	-0.110	492.997

As shown in Figure 5-7(a-e), the thickness of unfrozen water (containing zone i and zone iii) increases with rising temperature, such as the bound water layer only contained one water layer with a thickness of about 3 Å at 230 ~ 260 K (Figure 5-7(a-d)), but two water layer with one of about 6.0 Å at 270 K (Figure 5-7(e)). Furthermore, Figure 5-9(a) is T_2 relaxation curve, where the value of T_2 reflects the occurrence of pore water and pore size in the unfrozen state. The higher the T_2 (signal strength), the higher the unfrozen water content. The peak area and signal peak value increased with rising temperature, meaning the unfrozen water content also rose. On the other hand, based on the NMR signal, the unfrozen water could be measured through the Tize method [183], and displayed in Figure 5-9(b). As shown in Figure 5-9(b), the unfrozen water content in MD simulation is equal to the ratio of water molecules number to the total water-ice molecules number, where the values of unfrozen water content between MD simulation and NMR were not comparable, owing to complex composition of frozen soil in experiment and scale effect between macroscale and nanoscale. However, the type of fitting function evolution in MD simulation agreed well with that in NMR experiment [28], indicating the accuracy of the using force field and established model. For example, there are three main phase-change zones in frozen soil [28, 184]: severe phase-change zone (269 ~ 272 K), transitional phase-change zone (258 ~ 268 K), and freezing stable zone (< 258 K). Figure 5-9(b) shows that the unfrozen water content in MD simulation changes very little in freezing stable zone (230 ~ 260 K), while

increases exponentially in severe phase-change and transitional phase-change zone (260 ~ 270 K).
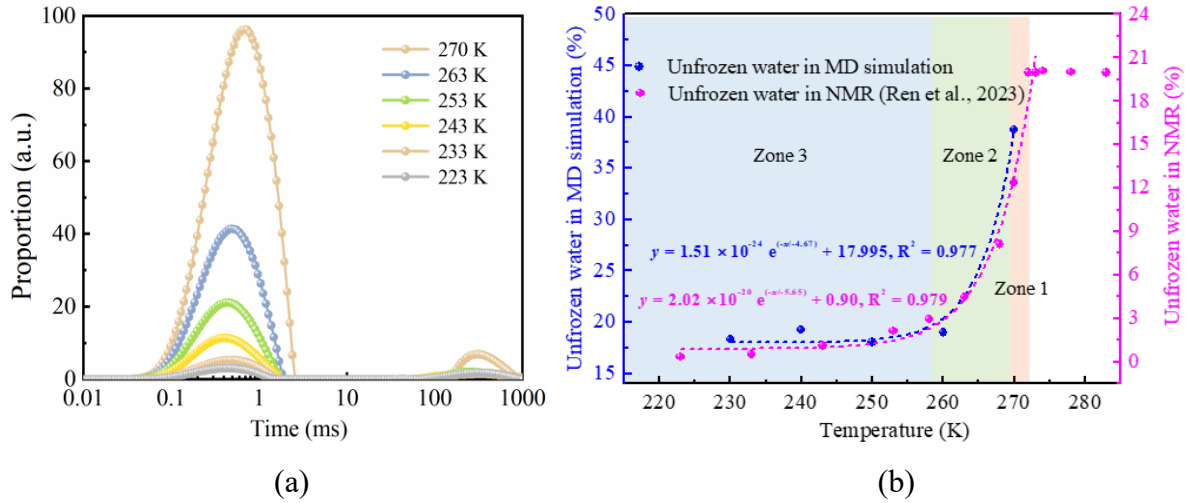

(a)   (b)

Figure 5-9. (a) T_2 relaxation curve of frozen soil from NMR [28]. (b) Evolution of content of unfrozen water in NMR experiment from Ren et al. [28] and MD simulation with temperature, where the fitting curve in NRM is based on the temperature range of 223 ~ 273 K. Moreover, there are three main phase-change zones in frozen soil [28, 184], such as severe phase-change zone (zone 1), transitional phase-change zone (zone 2), and freezing stable zone (zone 3), which correspond to the temperature range of 269 ~ 272 K, 258 ~ 268 K, and < 258 K, respectively.

5.3.2.3 Quasi-liquid water

Why is there disorder liquid water in zone iii (Figure 5-7(g)) on the surface of ice? Many scientists have verified that the disorder liquid water layer (so-called quasi-liquid water) existed on the surface of ice at temperature below melting temperature of ice through experiments[185, 186], where its thickness ranges from 1 to 94 nm at -1 °C[185]. On the other hand, based on the number of hydrogen bonds (HBonds) a water molecule donates (D) or accepts (A), Smit et al. [187] classified water molecules into four categories: such as, DAA water molecules: water molecules donating one and accepting two HBonds, in the same notation, DDA, DDAA, and DA water molecules (Figure 5-10(b)). They also reported that the number of free O-H groups originated from DAA and DA water molecules rose with rising temperature during 200 ~ 250 K, owing to thermal fluctuations causing the breaking of HBonds [187]. Moreover, Weber et al.

99

[177] found the "quasi-liquid water" layer onto ice surface through MD simulation (Figure 5-10(c)), where the HBonds in this topmost ice layer gradually broken with increasing temperature at over -70 °C, causing the transformation of DAA water molecules into highly mobile DA water molecules, and then increasing the ice surface mobility. This is the main reason why the ice surface is so slippery.

In this work, as shown in Figure 5-6 and Figure 5-7(g), the "quasi-liquid water" layer is also presented in the topmost ice layer at 230 ~ 270 K, and its thickness gradually increases with rising temperature, showing the ice changing into liquid water, which is consistent with the previous work from Smit and Bakker[186], who illustrated that the content of quasi-liquid water increased with rising temperature during 245 ~ 270 K (Figure 5-10(a)).
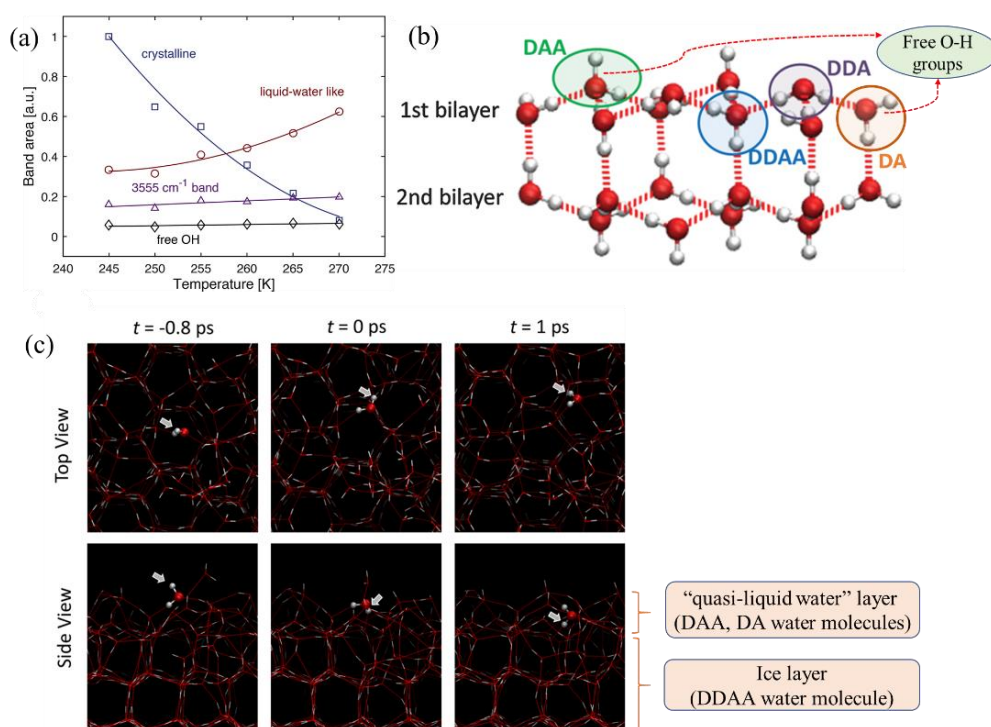

Figure 5-10. (a) Areas of the crystalline ice band (ca. 3230 cm^{-1}), the liquid-water-like band (ca. 3400 cm^{-1}), the 3555 cm^{-1} band, and the free OH band (ca. 3700 cm cm^{-1}) [186]. (b) Schematic of the DAA, DDA, DDAA, and DA water molecules at the basal ice-air interface with its perfect form [187]. (c) Snapshots of the MD trajectory of the ice-air interface at -43 °C, where top and bottom panels show the top and side views of the interface. Moreover, the water molecule with the free OH group that forms the new hydrogen bond at positive t is highlighted [177].

On the other hand, for montmorillonite-water system, Wei et al. [14] reported that there were two types of HBonds in Mt-water-ice system, where (1) the W-W HBonds (Water-Water) is established between water molecules; (2) the C-W HBonds (Clay-Water) is established between water molecules and the acceptor oxygen atoms (Ob) of montmorillonite surface. Similarly, as shown in Figure 5-11(a), Mt-water-ice system in this work also contains the two HBonds mention above. Figure 5-11(d) shows that the number of W-W HBonds decreases approximately linearly with increasing temperature, illustrating that the increasing temperature could cause the breaking of HBonds in water-ice system. Moreover, the number of C-W HBonds remained unchanged at $230 \sim 250$ K, followed by decreased with rising temperature at $250 \sim 270$ K, indicating that the ice near clay surface transformed into bound water was also due to the breakage of some HBonds.
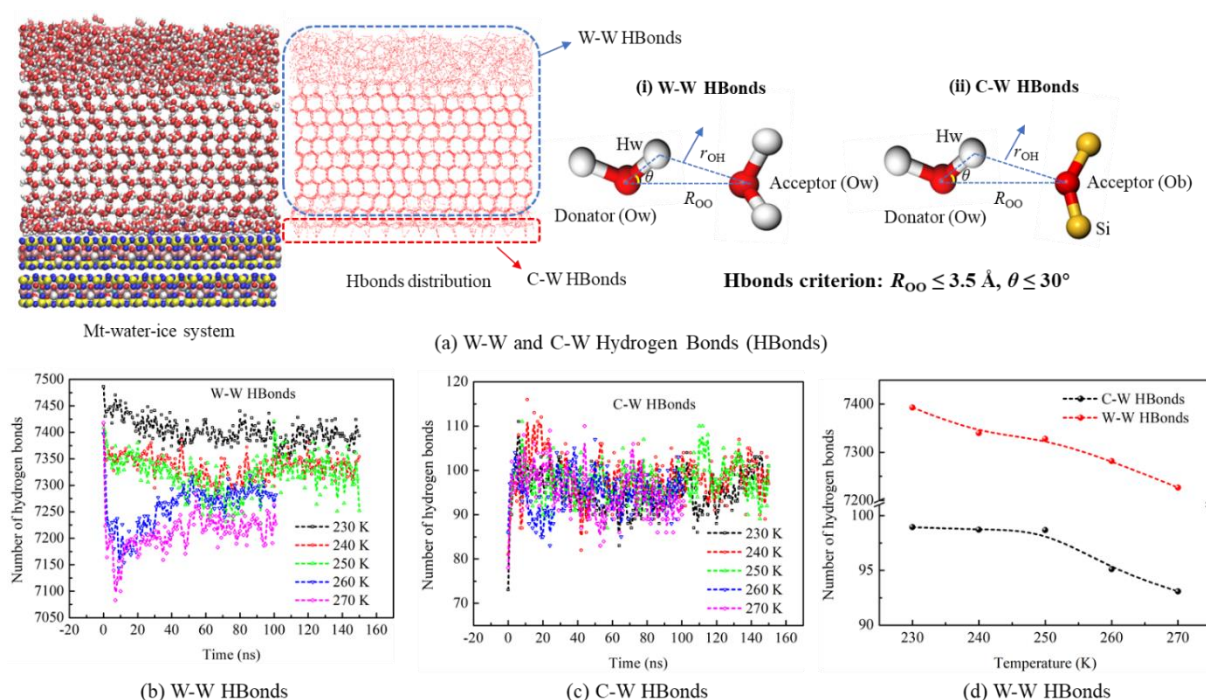

Figure 5-11. (a) Schematic diagram of W-W and C-W hydrogen bonds (HBonds), and (b-c) evolution of two HBonds number with time. Moreover, (d) the evolution of average number of W-W and C-W HBonds with temperature, where the data of the last 20 ns (130 ~ 150 ns) is averaged at 230 K, and the data of the last 50 ns is averaged at 240 ~ 250 K (100 ~ 150 ns) and 260 ~ 270 K (50 ~ 100 ns).
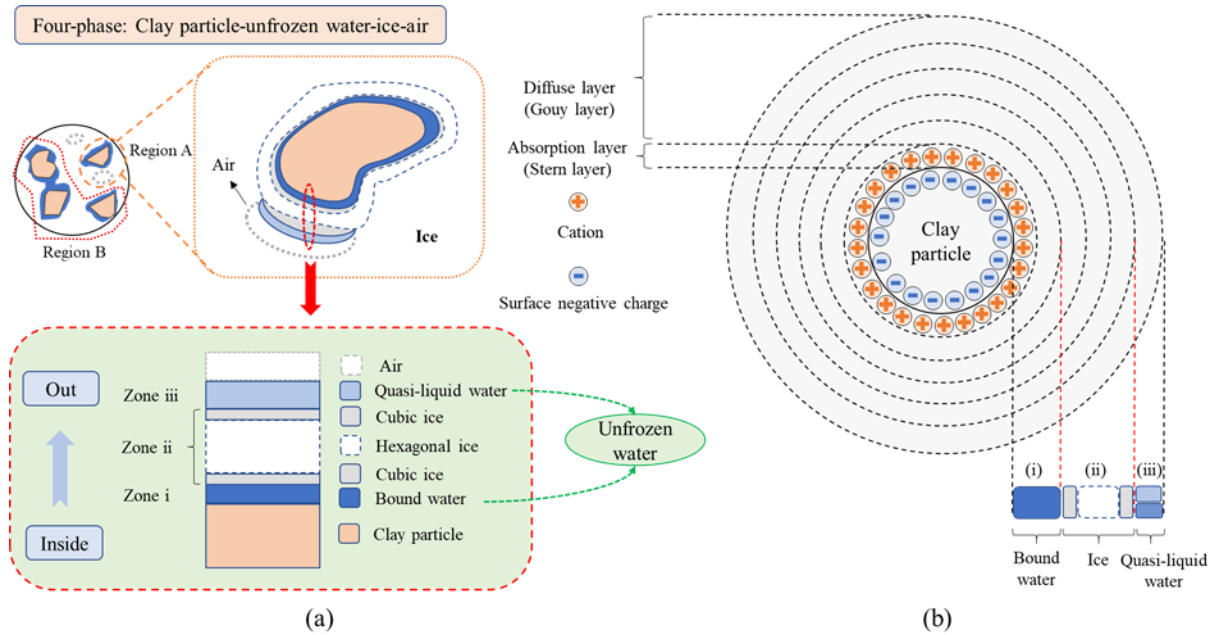
Figure 5-12. Division and distribution of microstructure of unfrozen water and ice onto clay particle at temperature below melting temperature: (a) from inside to out, and (b) base on the electrical double layer.

Based on an actual frozen soil environment, frozen soil usually was a four-phase system (containing soil, water, ice, and air). Combining with the above simulation results, the structure of water-ice onto montmorillonite could be strictly divided from inside to out as "montmorillonite-bound water-cubic ice-hexagonal ice-cubic ice-'quasi-liquid' water-air", as shown in Figure 5-12(a). For areas with air (Region A, corresponding to four-phase system), the appearance of quasi-liquid water was due to the ice-vacuum interface in whole system, which was used to simulate the ice-air interface mentioned in Section 2.1. However, for area without air (Region B, corresponding to three-phase system), we think that the zone iii did not exist, so the phase transformation evolution of water-ice in clay nanopores without air will also be worth exploring in the future.

In addition, Jin et al. [168] divided the microstructure of unfrozen water onto clay particles according to the electrical double layer, but they did not consider the subdivision of ice types, quasi-liquid water, and air in the soil. Therefore, based on previous work, we proposed a new division of microstructure of unfrozen water and ice onto clay particles, as shown in Figure

5-12(b). With the increasing temperature, the thickness of unfrozen water (containing bound and quasi-liquid water) gradually increased, while that of ice reduced, which was due to thermal fluctuations causing the breaking of HBonds in water-ice system.

5.3.3 Structure analysis

5.3.3.1 During 230 ~ 270 K

Figure 5-13 displays the RDF of various atom pairs in Mt-water-ice system at 230 ~ 270 K at final moment (230 ~ 250 K: 150 ns; 260 ~ 270 K: 100 ns) and initial Mt-ice model (Figure 5-1(c)), where the $O_{TIP4P/ICE}$-Na, $O_{TIP4P/ICE}$-Ob, $O_{TIP4P/ICE}$-Si, and Ob-$H_{TIP4P/ICE}$ atom pairs are not considered in initial Mt-ice model due to the existence of initial interlayer spacing of 10 Å. As shown in Figure 5-13(a) and (b), the RDF of $O_{TIP4P/ICE}$-$H_{TIP4P/ICE}$ and $O_{TIP4P/ICE}$-$O_{TIP4P/ICE}$ atom pairs in initial Mt-ice model still have lots of apparent peaks even at relatively long distance, showing its short- and long-range order properties and indicating a significant spatial correlation between these atom pairs. However, this certain spatial correlation of $O_{TIP4P/ICE}$-$H_{TIP4P/ICE}$ and $O_{TIP4P/ICE}$-$O_{TIP4P/ICE}$ atom pairs in Mt-water-ice system at 230 ~ 270 K significantly decreased, it was worth noting that there were still some peaks at a long distance. Because some ice molecules gradually transformed into water molecules as the temperature rose. On the other hand, as shown in Figure 5-13(c-h), RDF of the other six atom pairs in Mt-water-ice under different temperatures are very similar, so we need to analyze further their position of the first peak in RDF and CN, displayed in Table 5-4 and Table 5-5, respectively.

As shown in Table 5-4, there are obvious first peak of RDF at a certain position between $O_{TIP4P/ICE}$-Na, $O_{TIP4P/ICE}$-Ob, $O_{TIP4P/ICE}$-Si, and Ob-$H_{TIP4P/ICE}$, indicating an interaction between water-ice and montmorillonite system, including a H bond interaction between them (Ob-$H_{TIP4P/ICE}$). Moreover, the distance of interaction between $O_{TIP4P/ICE}$-Si was relatively higher than that between $O_{TIP4P/ICE}$-Na, $O_{TIP4P/ICE}$-Ob, and Ob-$H_{TIP4P/ICE}$. There was not obvious pattern for the position of first peak in RDF of these four atom pairs under different temperatures, but their respective value was close. Similarly, there was an obvious interaction between $O_{TIP4P/ICE}$-

$H_{TIP4P/ICE}$ and $O_{TIP4P/ICE}$-$O_{TIP4P/ICE}$ in water-ice system, as well as between Si-Ob and Al-Ob in montmorillonite system.

To understand the coordination environment and interaction strength of Mt-water-ice system, the CN of various atom pairs was obtained through equation (2-21), as shown in Table 5-5. With increasing temperature, the CN of $O_{TIP4P/ICE}$-$O_{TIP4P/ICE}$ increased due to the transformation of ice into water (Figure 5-7(a-e)), reflecting that their interaction effect rose. On the contrary, the CN of $O_{TIP4P/ICE}$-Na, $O_{TIP4P/ICE}$-Ob, $O_{TIP4P/ICE}$-Si, and Ob-$H_{TIP4P/ICE}$ decreased with rising temperature, illustrating that the interaction effect between water-ice and montmorillonite system gradually reduced. Moreover, the CN of Si-Ob and Al-Ob and their position of the first peak in RDF were the same with increasing temperature, illustrating that the structure of montmorillonite system was very stable and was not affected by this short temperature interval (230 ~ 270 K) and water-ice system.
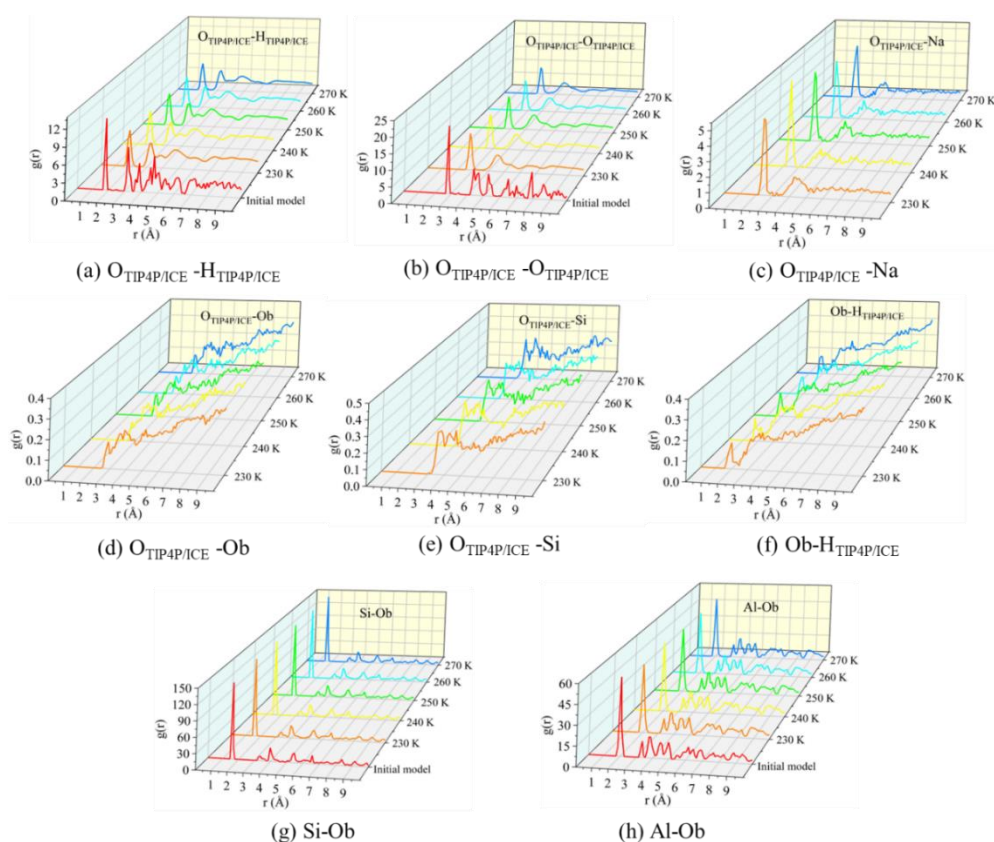

Figure 5-13. Radial distribution function (RDF) of various atom pairs in Mt-water-ice system under 230 ~ 270 K at the end of simulations (230 ~ 250 K: 150 ns; 260 ~

270 K: 100 ns) and initial Mt-ice model: (a) $O_{TIP4P/ICE}$-$H_{TIP4P/ICE}$; (b) $O_{TIP4P/ICE}$-$O_{TIP4P/ICE}$; (c) $O_{TIP4P/ICE}$-Na; (d) $O_{TIP4P/ICE}$-Ob; (e) $O_{TIP4P/ICE}$-Si; (f) Ob-$H_{TIP4P/ICE}$; (g) Si-Ob; (h) Al-Ob atom pairs. Moreover, the initial model mentioned in Figure 5-13 corresponds to the Mt-ice model in Figure 5-1(c).

Table 5-4. Position of the first peak in RDF of various atom pairs under different temperatures at the end of simulations.

System	Conditions	$O_{TIP4P/ICE}$-$H_{TIP4P/ICE}$	$O_{TIP4P/ICE}$-$O_{TIP4P/ICE}$	$O_{TIP4P/ICE}$-Na	$O_{TIP4P/ICE}$-Ob	$O_{TIP4P/ICE}$-Si	Ob-$H_{TIP4P/ICE}$	Si-Ob	Al-Ob
Mt-ice	Initial model	1.75		-	-	-	-		
	230 K			2.35	2.85	3.75	1.95		
Mt-water-ice	240 K		2.75	2.35	2.75	3.65	1.75	1.55	1.95
	250 K	1.85		2.35	2.85	3.75	1.85		
	260 K			2.45	2.75	3.55	1.95		
	270 K			2.45	2.75	3.65	1.85		

Table 5-5. Coordination number (CN) of various atom pairs under different temperatures at the end of simulations, where the distance (r) is equal to the position corresponding to the first valley of RDF curve.

System	Conditions	$O_{TIP4P/ICE}$-$H_{TIP4P/ICE}$ (r = 2.45 Å)	$O_{TIP4P/ICE}$-$O_{TIP4P/ICE}$ (r = 3.35 Å)	$O_{TIP4P/ICE}$-Na (r = 3.05 Å)	$O_{TIP4P/ICE}$-Ob (r = 3.05 Å)	$O_{TIP4P/ICE}$-Si (r = 3.95 Å)	Ob-$H_{TIP4P/ICE}$ (r = 2.55 Å)	Si-Ob (r = 1.95 Å)	Al-Ob (r = 2.65 Å)
Mt-ice	Initial model	1.942	3.817	-	-	-	-		
	230 K	1.952	3.956	0.030	0.028	0.066	0.069		
Mt-water-ice	240 K	1.953	3.966	0.030	0.027	0.065	0.071	3.677	3.429
	250 K	1.950	3.958	0.029	0.025	0.065	0.069		
	260 K	1.950	3.972	0.028	0.023	0.063	0.067		
	270 K	1.947	4.038	0.026	0.025	0.057	0.062		

5.3.3.2 Different zones in melting temperature (270 K)

To explore the structure properties of three different zones in water-ice system (Figure 5-12),

Figure 5-14 shows the RDF and CN of $O_{TIP4P/ICE}$-$O_{TIP4P/ICE}$, $O_{TIP4P/ICE}$-$H_{TIP4P/ICE}$, $O_{TIP4P/ICE}$-Na, $O_{TIP4P/ICE}$-Ob, and $O_{TIP4P/ICE}$-Si atom pairs of different zones (zone i, ii, and iii) in Mt-water-ice system at 270 K. Comparing to other temperatures (230 ~ 260 K), the distribution of three zones at 270K was more obvious (Figure 5-7).
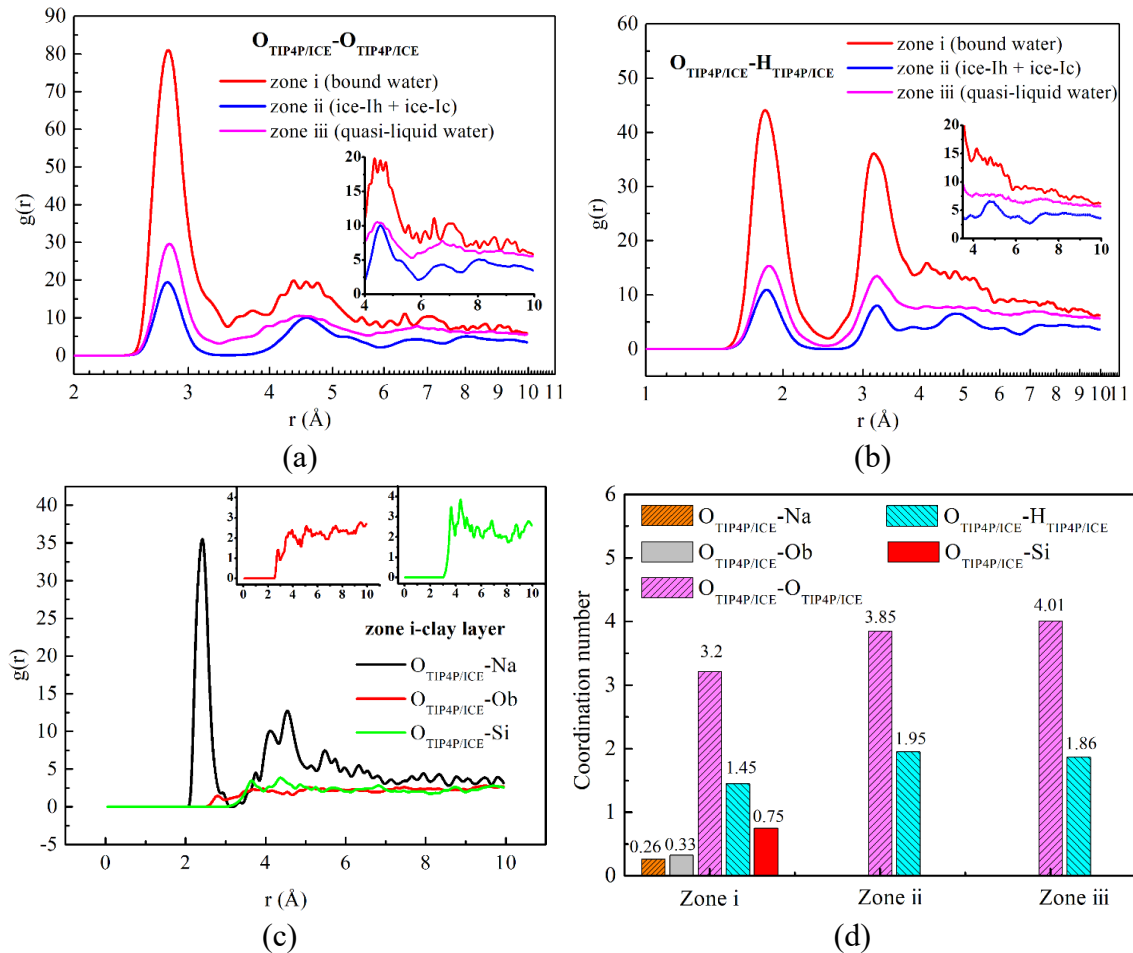

Figure 5-14. RDF of (a) $O_{TIP4P/ICE}$-$O_{TIP4P/ICE}$ and (b) $O_{TIP4P/ICE}$-$H_{TIP4P/ICE}$ in different zones, such as zone i (bound water), zone ii (hexagonal and cubic ice, i.e. ice-Ih and ice-Ic), and zone iii (quasi-liquid water), as well as (c) $O_{TIP4P/ICE}$-Na, $O_{TIP4P/ICE}$-Ob, $O_{TIP4P/ICE}$-Si atom pairs in zone i-clay layer at 270 K. Moreover, (d) the coordination number of $O_{TIP4P/ICE}$-$O_{TIP4P/ICE}$, $O_{TIP4P/ICE}$-$H_{TIP4P/ICE}$, $O_{TIP4P/ICE}$-Na, $O_{TIP4P/ICE}$-Ob, and $O_{TIP4P/ICE}$-Si atom pairs, where their position corresponding to the first valley of RDF curve are equal to 3.35, 2.45, 3.05, 3.05, and 3.95 Å, respectively.

As shown in Figure 5-14(a) and (b), the RDF of $O_{TIP4P/ICE}$-$O_{TIP4P/ICE}$ and $O_{TIP4P/ICE}$-$H_{TIP4P/ICE}$ in zone i and ii still have some obvious peaks at a longer distance, and their peak number are

higher than that in zone iii. Comparing to RDF of O-O and O-H in bulk water system at 300 K from Wei et al.[176] (Figure 6-4), the structure properties of zone iii was somewhat similar to that of bulk water, while the peak number of $O_{TIP4P/ICE}$-$O_{TIP4P/ICE}$ in zone iii was slightly higher than bulk water, illustrating that the structure of this quasi-liquid water is intermediate between liquid free water and ice.

For the oxygen atom ($O_{TIP4P/ICE}$) in zone i, it coordinated not only with itself and hydrogen atom ($H_{TIP4P/ICE}$), but also with other atoms in clay layer, such as Na, Ob, and Si atom. Figure 5-14(c) shows the RDF of $O_{TIP4P/ICE}$-Na, $O_{TIP4P/ICE}$-Ob, $O_{TIP4P/ICE}$-Si in zone i-clay layer. Furthermore, CN of the five atom pairs mentioned above was displayed in Figure 5-14(d), where five different atoms coordinating with oxygen atoms ($O_{TIP4P/ICE}$) are sorted according to the size of the coordination number: $O_{TIP4P/ICE}$ > $H_{TIP4P/ICE}$ > Si > Ob > Na. On the other hand, the order of CN of $O_{TIP4P/ICE}$-$O_{TIP4P/ICE}$ in three zones was zone iii > zone ii > zone i, indicating the higher coordination of $O_{TIP4P/ICE}$-$O_{TIP4P/ICE}$ in quasi-liquid water, and the lower one in bound water owing to coordinating with other atoms in clay layer.

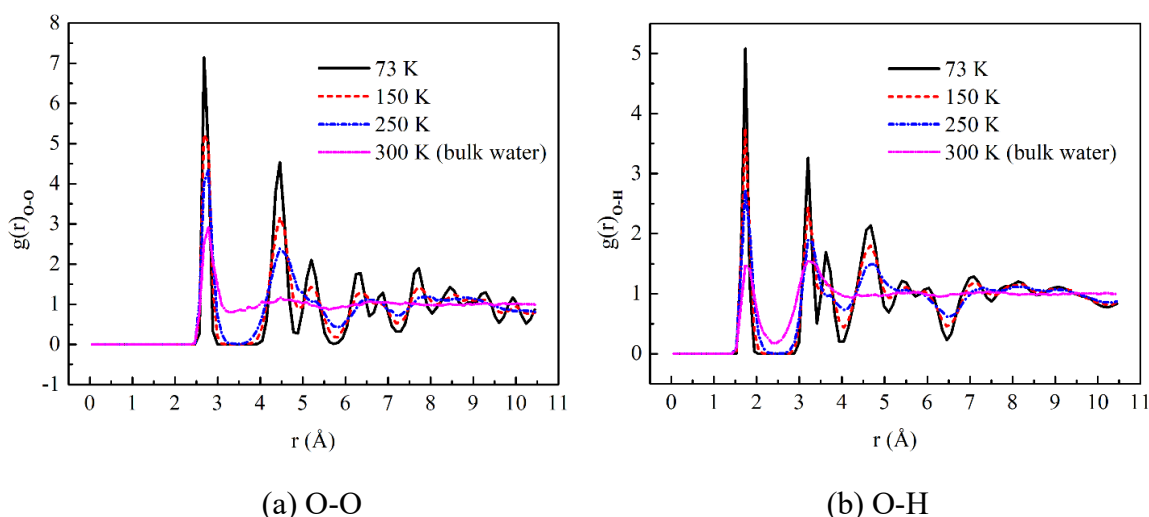(a) O-O   (b) O-H

Figure 5-15. Effect of temperature on RDFs of ice-Ih (73, 150, and 250 K) and bulk water system (300 K) using SPC/E water model: (a) O-O and (b) O-H atom pair. [176]

5.3.4 Dynamic properties

Figure 5-16 shows the velocity and density distribution of oxygen atom ($O_{TIP4P/ICE}$) in Mt-

water-ice system at the end of simulations under different temperatures. As shown in Figure 5-16(a-d), at 230 ~ 260 K, the density distribution of oxygen atom in water-ice system was relatively uniform and close, it is due to the small thickness of quasi-liquid water and bound water layer. On the other hand, for the case in 270 K with more obvious distribution of three zones, as shown in Figure 5-16(e), the uppermost layer in quasi-liquid water contacting with vacuum has the most high mobility, and the density of quasi-liquid water zone fluctuates around 1.0 g/cm^3, which was close to that of free water. Moreover, the bound water with low velocity and relatively high density was due to the adsorbed effect by montmorillonite layer.
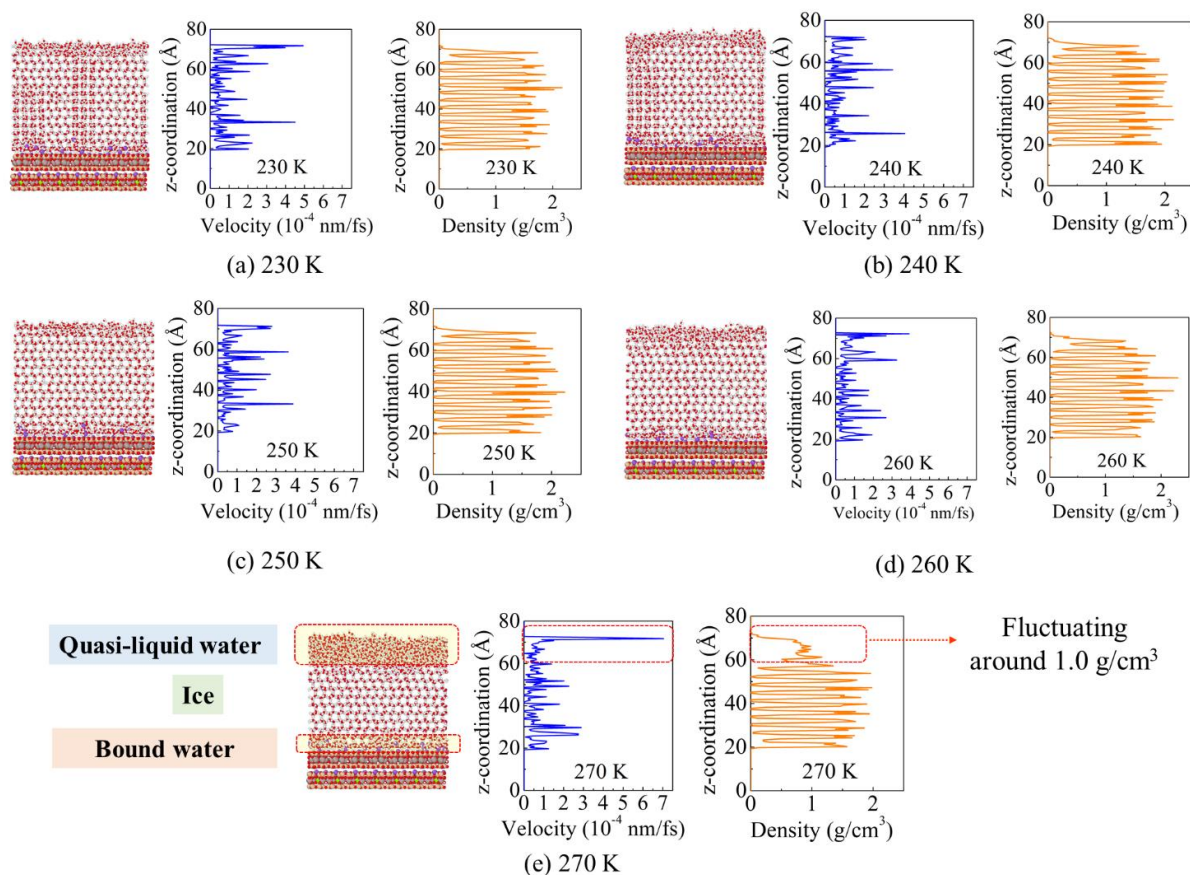

Figure 5-16. Structure, velocity, and density distribution of oxygen atom (O$_{TIP4P/ICE}$) in water-ice system at the end of simulations under different temperatures: (a) 230 K, (b) 240 K, (c) 250 K, (d) 260 K, and (e) 270 K.

To explore the motion path and dynamic strength of atom, the representative atoms trajectory

lines in three different zones during 50 ~ 100 ns at 260 and 270 K are displayed in Figure 5-17. As shown in Figure 5-17(a), at 260 K, the atoms in bound water and ice zones basically vibrate in their own position, while ate atoms in quasi-liquid water zone has a certain fluidity. At 270 K, the fluidity of atom in bound water and quasi-liquid water zones increased, while that of ice zone was close to 0 (Figure 5-17(b)).
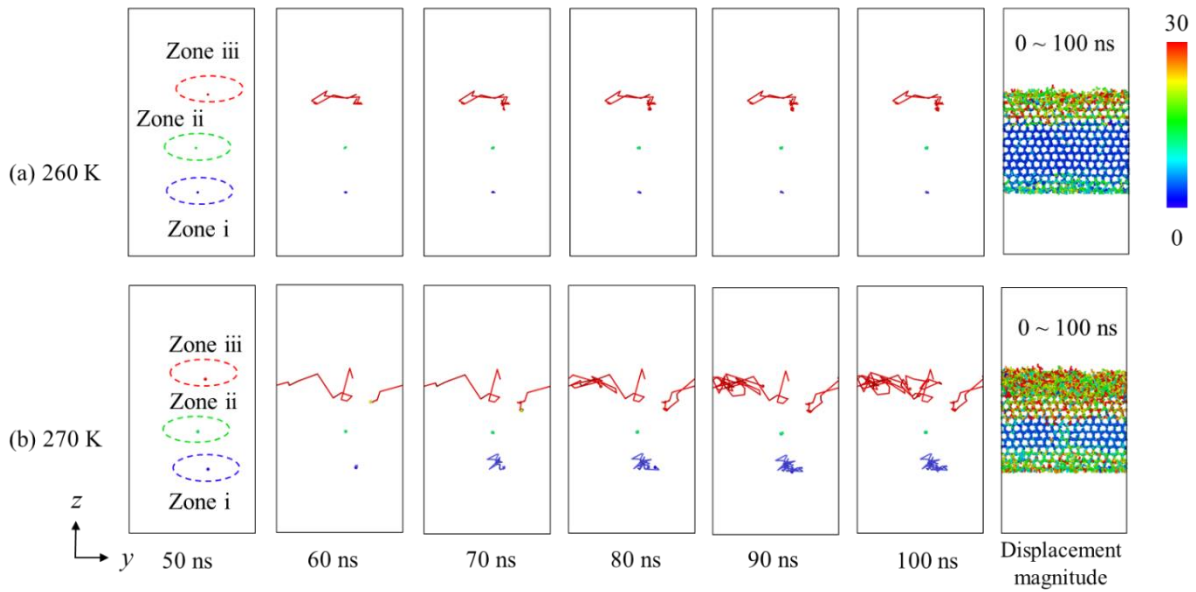

Figure 5-17. Atom trajectory lines in three different zones during 50 ~ 100 ns (a) 260 and (b) 270 K, where zone i (bound water), zone ii (hexagonal and cubic ice), and zone iii (quasi-liquid water) are corresponding to blue, green, and red line.

Figure 5-18 shows MSD and diffusion coefficient of oxygen atom ($O_{TIP4P/ICE}$) in water-ice system, which are used to describe its dynamic properties. As shown in Figure 5-18(a), the relationship of MSD in 270 K is approximately linear, especially in 50 ~ 100 ns, while the MSD along z-direction rapidly increases with time in 0 ~ 30 ns, which is due to the unstable of ice-water phase transformation in Mt-water-ice system. Thus, the diffusion coefficient of $O_{TIP4P/ICE}$ atom was calculated from the slope of MSD and time in stable stage through eq. (6), displayed in Figure 5-18(b).

As shown in Figure 5-18(b), the higher the temperature is, the more violent the thermal fluctuations of the atoms is. Thus, the overall diffusion coefficient rose exponentially with

increasing temperature. Moreover, the maximum overall diffusion coefficient of 0.658×10^{-10} m^2/s in 270 K was significantly less than that of bulk water (23×10^{-10} m^2/s) at room temperature obtained from experiment [188], which was due to the existence of ice molecules with low liquidity and adsorption effect of clay to bound water in Mt-water-ice system. Furthermore, the diffusion coefficient along x- and y-direction was very close, and was greatly superior to that along z-direction. It meant that the liquidity along z-direction of $O_{TIP4P/ICE}$ in water-ice system was the lowest, owing to the absorption effect of montmorillonite to water-ice system.
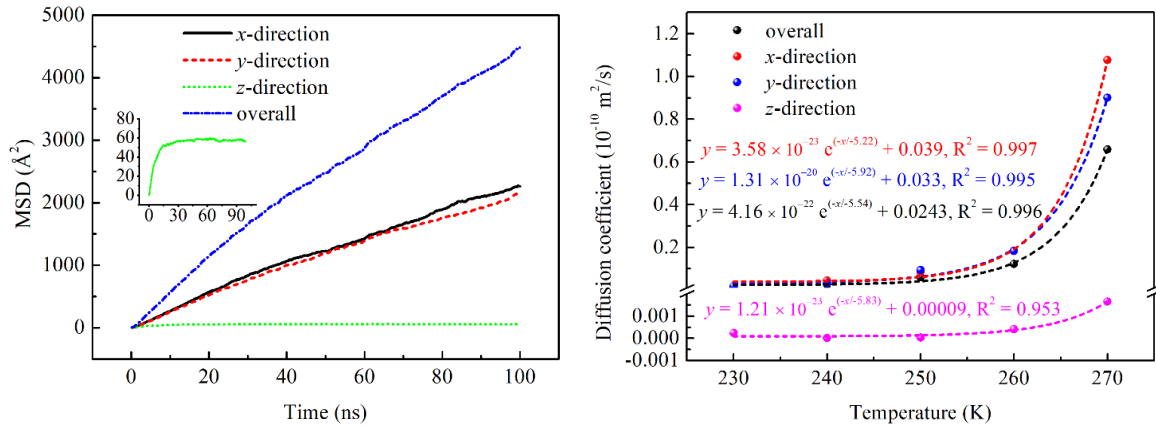
(a) x-, y-, z-, and overall-MSD in 270 K   (b) Diffusion coefficient

Figure 5-18. Evolution of (a) MSD in 270 K and (b) diffusion coefficient (10^{-10} m^2/s) in $230 \sim 270$ K of oxygen atom ($O_{TIP4P/ICE}$) in water-ice system with time. Among them, the diffusion coefficient is obtained in stable stage through eq. (6), where the stable stage corresponded to the last 20 ns ($130 \sim 150$ ns) at 230 K, as well as the last 50 ns at $240 \sim 250$ K ($100 \sim 150$ ns) and $260 \sim 270$ K ($50 \sim 100$ ns). Moreover, the diffusion coefficient of bulk water is 23×10^{-10} m^2/s in room temperature [188].

5.4 Conclusions

Molecular Dynamics simulations have been performed to investigate the interfacial, structure, and dynamics properties of unfrozen water-ice onto montmorillonite surface, further revealing their phase transformation and composition behavior. This work could provide a new insight into the understanding of interaction between clay interface and unfrozen water-ice, clarifying the phase transformation process of unfrozen water-ice system onto montmorillonite interface

and structure evolution of whole system. The conclusions are obtained as follows:

(1) Based on the simulation results and electrical double layer theory, a new division of microstructure of unfrozen water and ice onto clay particle was proposed and determined, which was "montmorillonite-bound water-cubic ice-hexagonal ice-cubic ice-'quasi-liquid' water-air".

(2) The presence of unfrozen water in frozen soil was mainly due to surface effect of clay, including coulomb electrostatic and van der Waals interaction, where coulomb electrostatic interaction was the main influencing factor.

(3) With the increasing temperature, Hydrogen bonds in water-ice system could be broken due to thermal fluctuations, resulting in ice transforming into unfrozen water (containing bound and quasi-liquid water). Moreover, the transformation degree of ice into unfrozen water was relatively slow in 230 ~ 260 K, while exponentially rose in 260 ~ 270 K.

(4) The structure property of this quasi-liquid water is intermediate between liquid free water and ice.

Chapter 6

Phase Transformation Evolution and Mechanical Properties of Bulk Ice under Tension at Nanoscale

Chapter 6. Phase Transformation Evolution and Mechanical Properties of Bulk Ice under Tension at Nanoscale [IV]

Abstract

The mechanical behavior of ice is complex, especially with the effect of temperature and pressure, which may significantly affect the safety in various engineering, where slow deformation of ice may bring more hidden, sudden, and severe damage. The mechanical behavior of ice-Ih under a low strain rate with the effect of temperature and confining pressure is still unclear, especially at the nanoscale. In this work, the tensile behavior of ice-Ih is investigated using Molecular Dynamics simulation method. The tensile test of ice-Ih was all performed along the *y*-direction ([0 1 0] crystal orientation) with a constant strain rate of 1×10^8 s^{-1}. The effect of temperature (73 to 270K with 1 atm), as well as the confining pressure (1 atm to 200 MPa, combined with 100 K, 150K, 200K, and 250 K) on the tensile behavior of ice-Ih, was studied, respectively. The tensile stress-strain response under different temperatures was obtained, and the linear relationship of temperature and Young's modulus was consistent with other previous studies. The tensile strength of ice-Ih decreased linearly with increasing temperature under low strain rate, which is quite different from the cases under high strain rate. The solid-solid phase transformation was observed at 73 ~ 140 K, and the solid-liquid phase

transformation at 150 ~ 270 K, where more energy is required in completely solid-liquid phase transformation at 250 ~ 270 K than solid-solid phase transformation at 73 ~ 140 K. The evolution of total potential energy increment and structural failure with strain significantly depended on the phase transformation of ice-Ih. Moreover, the ice-Ih is earlier and more likely to be melted at higher confining pressure.

Keywords: Ice-Ih; Molecular Dynamics; Temperature and pressure; Tensile failure mechanism; Phase transformation.

6.1 Introduction

Ice is the second-largest massive solid in the lithosphere, and is an essential factor influencing the water cycle [189]. Recently, there has been a lot of exploration, development, and construction in areas dominated by ice. These activities provide various challenging engineering problems concerning ice [190], such as: (a) How to estimate the maximum force of ice that could withstand a structure? (b) How about the effect of human activity, temperature changes, and external loading on the stability of ice bodies, etc.? All these problems may be related to the deformation and strength of ice under external environmental factors. On the other hand, over 15 different solid-state crystal structures of ice have been identified depending on different temperatures and pressure conditions [191, 192], which causes the complexity of its mechanical behavior. Therefore, the dynamic mechanical behavior of ice has its scientific and engineering importance in plenty of diverse aspects, such as ice blasting, glaciology, global climate, geophysics, permafrost engineering, etc. [189, 193-195] Furthermore, the damage caused by the slow deformation of ice is more hidden, sudden, and severe. Thus, a better understanding of the mechanical properties of ice with a low strain rate is beneficial for disaster evaluation and mitigation of ice-shelves collapsing [196], permafrost engineering [197] accidents, the prediction of movement and breakup of glaciers [193].

The mechanical properties of ice have been studied under different conditions via experiments, such as split Hopkinson pressure bar (SHPB) [195, 198-201] and Ground Penetrating Radar (GPR) [202], as well as computational simulations, such as finite element method (FEM) [203, 204]. Shazly et al. [199] studied the high strain-rate behavior of ice under uniaxial compression using a modified SHPB at 243 ~ 263 K with the strain rate in the range of 60 ~ 1400 s^{-1}, and found that the compressive strength of ice rose when the strain rate increased or temperature decreased, which is similar to the experimental result described by Kim and Keune [198]. An anomalous temperature effect was found from a compressive experiment with high strain rates of 100 s^{-1} to 1350 s^{-1} [200], which obtained that the compressive strength of ice increased with decreasing the temperature at 148 ~ 258 K, and remained nearly unchanged at 100 ~ 148 K.

Elvin [203] reported Young's modulus of ice without grain boundary is superior to that with grain boundary using FEM. Godio and Rege [202] focused on deriving the density and the bulk/shear modulus of snow through GPR, P-wave seismic data, and dispersive seismic surface waves. Although lots of works have focused on understanding the mechanical properties of ice at the macroscopic scale, the deformation and failure mechanisms of ice at the nanoscale are still very limited [193].

Molecular Dynamics (MD) simulation method is a good tool to study the microstructural evolution and mechanical mechanism of ice. Up to now, plenty of research has been devoted to studying nucleation and phase transformation [162, 167, 182], as well as adhesion [205, 206] of ice in the past few decades. In recent years, MD simulation method has been performed to investigate the microstructural evolution and mechanical mechanism of ice under different temperatures and external loading [189, 193, 207, 208]. Cao et al. [193] had studied the effect of grain size, grain boundary, and various loading modes on mechanical properties of bi- and poly-crystalline ice. Yin et al. [208] have investigated temperature-dependent phase transformation of ice-Ih under ultrafast uniaxial compression at 163 ~ 242 K, which showed the ice strength increasing with the decrease of temperature, and solid-solid/solid-liquid phase transformations depending on temperature. Chen et al. [189] explored the temperature effect on tensile strength of ice under shock loading with a high strain rate, and found the anomalous temperature effect, which is similar to the results found by Wu and Prakash [200]. Numerous MD simulations have been performed to study the mechanical behavior of ice under different temperatures and high strain rates, as well as its freezing/melting mechanism. However, the mechanical properties under uniaxial tensile and compression with confining pressure are more important for practical engineering. To the best of our knowledge, the effect of temperature and confining pressure on the tensile dynamic mechanical behavior of ice at a low strain rate is still unclear. Thus, some interesting questions arise: under tensile loading with a low strain rate, could the anomalous temperature effect still be found? Does the water-ice phase transformation depend on temperature, like the study of Chen et al. [189]? How does the confining pressure affect the

microstructure and failure path of ice?

In this study, MD simulations have been performed to study the effect of temperature and confining pressures on the tensile mechanical behavior of hexagonal ice (ice-Ih), the most 'ordinary' ice crystal on earth [201, 209]. The evolutions of Young's modulus, the ultimate tensile strength, microstructure, and the phase transformation of ice-Ih with temperature have been studied. The confining pressure effect on the microstructure and mechanical strength of ice-Ih is also analyzed.

6.2 Computational details

6.2.1 System setup

The SPC/E water model [210] has been used for efficiently describing the properties of bulk water [211, 212] and the mechanical properties of ice under different loads [189, 208], which was applied in this work. The SPC/E water model has a rigid geometry with an angle of 109.47º and a bond length of 1.0 Å controlled by the SHAKE method [213]. The orthogonal ice-Ih system was built, with the dimension of the ice-Ih supercell set as 40.6 Å × 39.1 Å × 36.8 Å (Figure 6-1(a)), including 1800 water molecules. The unit of ice-Ih model from Bernal et al. [175] is conducted in this study, which has a hexagonal symmetry with a space group of *P6_3cm*, including five water molecules and then forming an open tetrahedral crystal cell.
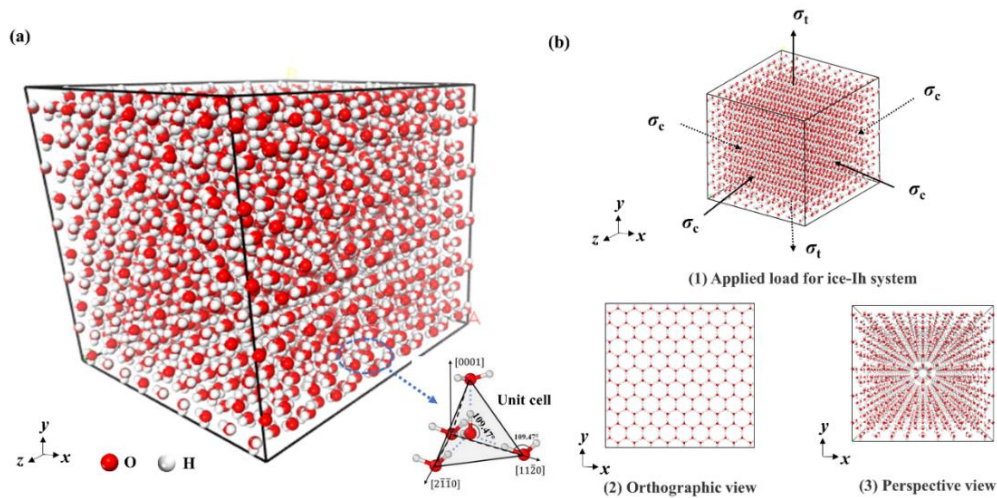

Figure 6-1. Atomic structures of the ice-Ih model: (a) supercell structure; (b) applied

load for ice-Ih system, as well as Orthographic and Perspective view of ice-Ih, where σ_t and σ_c are tensile load and confining pressure, respectively.

6.2.2 Relaxation and simulation details

MD simulations in this study were performed with LAMMPS [50] code. Three-dimensional periodic boundary conditions, Lennard-Jones potential with a cut-off radius of 10.5 Å, and the Verlet algorithm [97] for the integral of motion equation were applied in the simulations. The Ewald method [98] with an accuracy of 1.0e-6 kcal/mol and a cut-off radius of 8.0 Å were conducted for long-range electrostatic interactions. The total potential energy was calculated by eq. (6-1).

$$E_{total} = E_{bond\ stretch} + E_{angle\ bend} + E_{Coulomb} + E_{VDW}$$

$$= k_1 \left(r_{ij} - r_0 \right)^2 + k_2 \left(\theta_{ijk} - \theta_0 \right)^2 + \frac{e^2 q_i q_j}{4\pi\varepsilon_0 r_{ij}} + 4\varepsilon_{ij} \left[\left(\frac{\sigma_{ij}}{r_{ij}} \right)^{12} - \left(\frac{\sigma_{ij}}{r_{ij}} \right)^6 \right] \qquad (6-1)$$

where $E_{bond\ stretch}$, $E_{angle\ bend}$, $E_{Coulomb}$, and E_{VDW} are bond stretch energy, angle bend energy, Coulombic energy, and Van der Waals energy, respectively. k_1 and k_2 are the force constants, and r_0 represents the equilibrium bond length; r_{ij} is the distance between atoms i and j; θ_{ijk} is the bond angle of hydrogen-oxygen-hydrogen, and θ_0 represents the equilibrium bond angle; q_i and q_j are the charges of atoms i and j, respectively; ε_0 is the dielectric constant; σ and ε are the size and energy parameters, respectively. Moreover, σ_{ij} and ε_{ij} can be obtained by Mixing Lorentz-Berthelot's law [48].

During thermo-relaxation, the Nosé-Hoover method [214] was employed to control the temperature and pressure. The isothermal-isobaric (NPT) ensemble with the pressure of 1 atm was used during the thermo-relaxation process, where the time step was 1.0 fs. The ice-Ih system was firstly equilibrated for 200 ps, where the temperature rose from 1 K to 200 K. Thereafter, the system was relaxed for another 200 ps with 200 K and 1 atm. Afterward, the ice-Ih system was heated or cooled to 11 different temperatures (73 ~ 270 K) for 100 ps. Finally, these systems were further equilibrated at their defined temperatures for 200 ps before loading.

It was sufficiently long for the ice-Ih system to reach equilibrium.

After relaxation, the tensile test was divided into two series: (1) To explore the effect of temperature on mechanical properties of ice-Ih, the tensile loading was applied for ice-Ih system at 11 different temperatures along the y-direction ([0 1 0] crystal orientation) under tensile strain rate 1×10^8 s^{-1} for 3 ns, so the total tensile strain was 0.3. During this tensile loading, the pressure in the x- and z-direction ([1 0 0] and [0 0 1] crystal orientation, respectively) remained unchanged, as 1 atm, as shown in Figure 6-1(b). (2) To investigate the coupling effect of temperature and confining pressure on the failure and deformation mechanism of ice-Ih, the temperature of 100, 150, 200, and 250 K, as well as confining pressure of 1 atm, 50, 100, 200 MPa were combined to carry out the tensile tests along the y-direction under tensile strain rate of 1×10^8 s^{-1} for 3 ns.
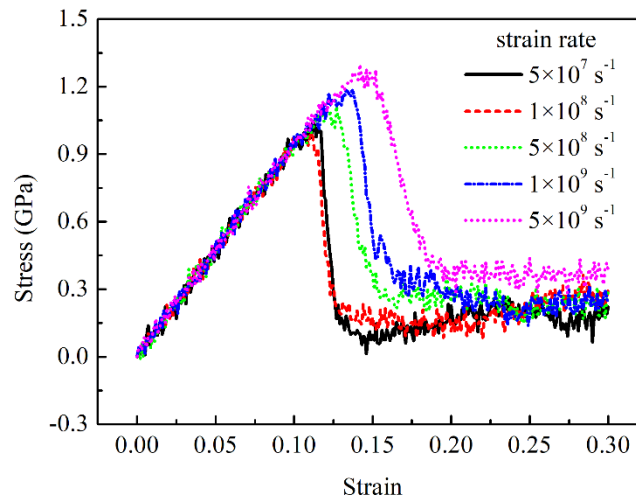
Figure 6-2. Evolution of tensile stress with strain for ice-Ih at 200 K under different strain rates.

According to previous studies, the strain rate plays a significant role in the mechanical properties of ice [189, 199, 208]. The convergence test of tensile strain rate is first carried out in this work, where the relationship of tensile stress-strain at 200 K under different strain rates is shown in Figure 6-2. The higher the strain rate, the greater the mechanical strength of the ice-Ih, which agrees well with Yin et al. [208] and Shazly et al. [199]. Furthermore, the stress-strain curves

between strain rates of $5\times10^7\,s^{-1}$ and $1\times10^8\,s^{-1}$ are very close, which means that the tensile strain rate less than $1\times10^8\,s^{-1}$ has little influence on the tensile stress-strain relationship. To ensure the reliability of simulations and save the computation time, the tensile rate of $1\times10^8\,s^{-1}$ was selected in this work, the same as the strain rate applied to study the mechanical properties of bi- and poly-crystalline ice by Cao et al. [193].

6.3 Results and discussions

6.3.1 Effect of temperature on atomic structure of ice-Ih

The atomic structure of ice is significantly affected by temperature [208]. The atomic structure of ice-Ih after relaxation is studied in this section under different temperatures by calculating the side length, volume, density, radial distribution function (RDF), and order parameter (F_3).

As shown in Figure 6-3(a), the side length of three directions and the volume of the ice-Ih system could increase almost linearly with temperature. The order of the expansion rate of side length is z- > y- > x-direction. Moreover, as shown in Figure 6-3(b), the density of ice-Ih decreases with increasing temperature, which is in good agreement with the "thermal expansion and contraction" phenomenon [215].
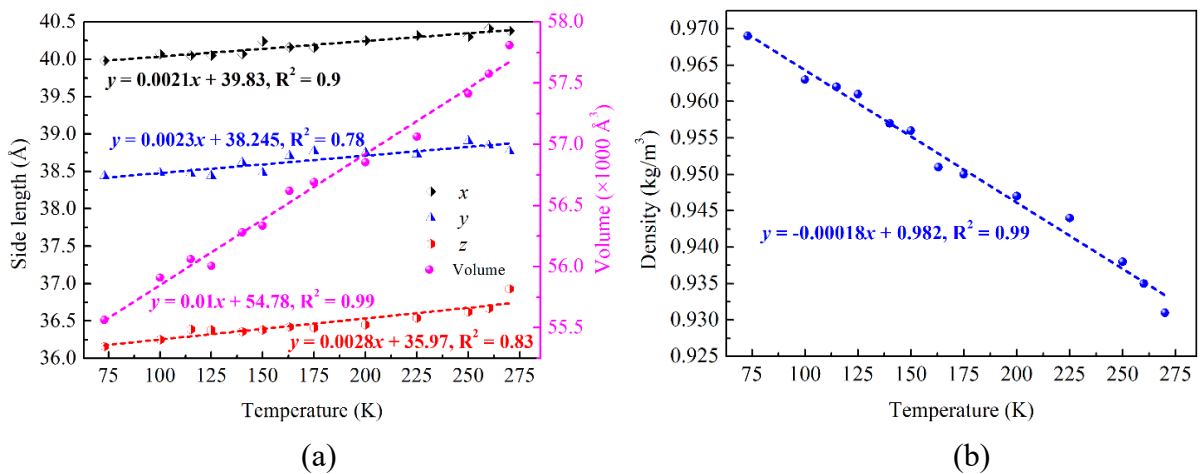
Figure 6-3. Evolution of (a) the side length and the volume, as well as (b) the density of ice-Ih with temperature.

Figure 6-4. Effect of temperature on RDFs of ice-Ih: (a) Global RDF; (b) Partial RDF of O-H; (c) H-H; (d) O-O atom pair, where RDF of bulk water acts as a comparison group; (e) evolution of the first peak of RDF of atom pair with temperature.

The global, O-H, H-H, and O-O RDF of ice-Ih and bulk water under different temperatures are shown in Figure 6-4 (a) ~ (d), where the RDF of bulk water acts as a comparison group.

The peak number in the global, O-H, H-H, and O-O RDF curves decreases with increasing temperature. Especially, numerous peaks of RDF at 73 K are recognizable. As shown in Figure 6-4 (a), although the long-range order of ice-Ih was still found at 250K, its degree of long-range order decreased with increasing temperature. It could indicate that the structure of ice-Ih before loading remained a solid phase.

Moreover, as shown in Figure 6-4(e), in all these cases, the first peak of RDF decreases constantly with increasing temperature, which is consistent with the global RDF of ice in the range 73 ~ 200 K found by Chen et al. [189]. The dist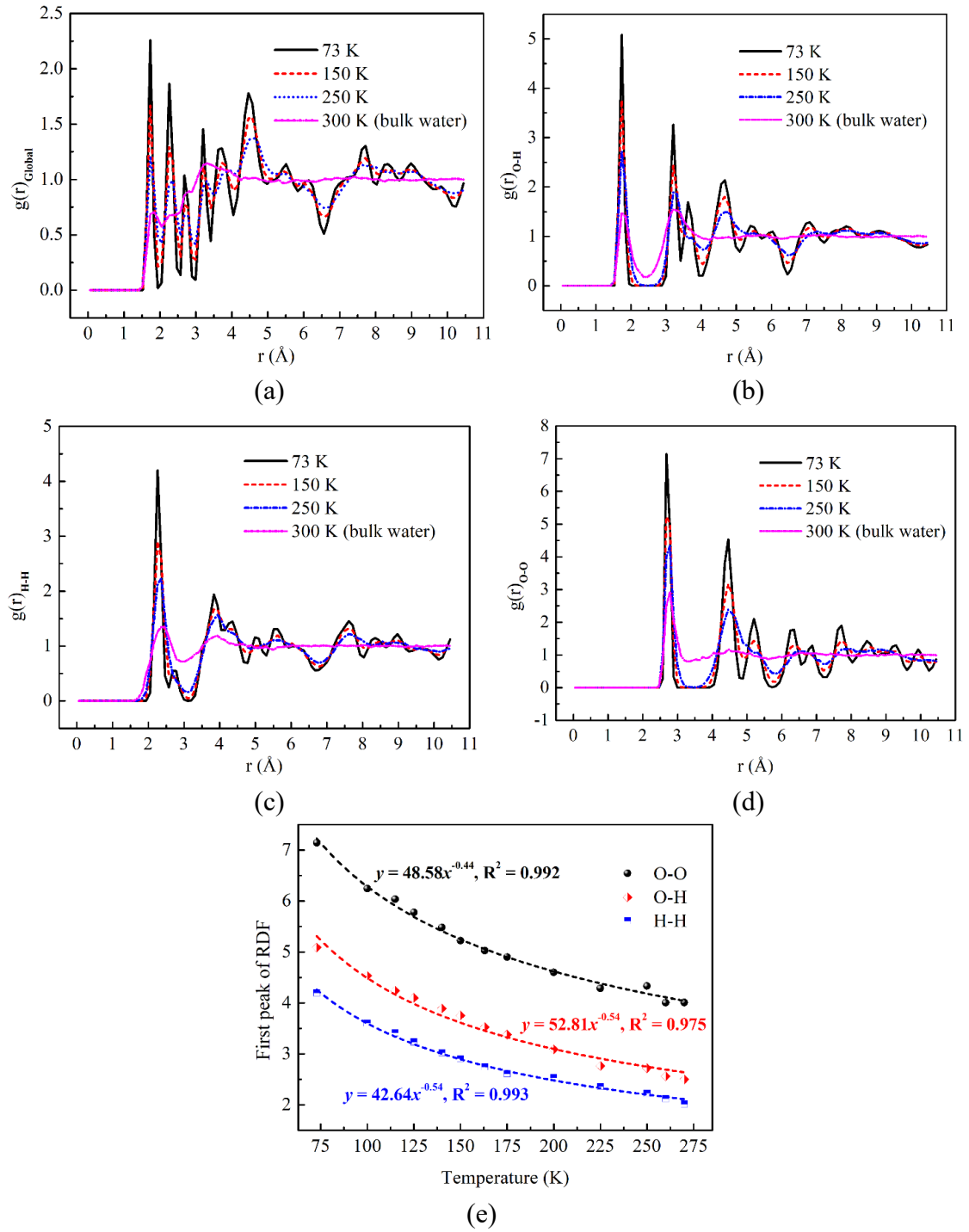ance of the first peak of RDF for O-O atom pair is 2.68 Å at 73 ~ 225 K, and rise to be 2.78 Å at 250 ~ 270K; but that of O-H and H-H remain unchanged, as 1.73 Å and 2.26 Å, respectively (See Figure 6-4(e)). No deformation can be found in the atomic structure of single water molecular, but the distance between water molecules increases with elevating temperature. Consequently, the atomic structure of ice generally becomes loose with increasing temperature, and then the ice expands.

The F_3 is used to describe the deformation of the atomic structure of ice-Ih in this study. As shown in Figure 6-5, the F_3 increases with temperature for ice-Ih, but it is far inferior to 0.1 in all cases. The higher temperature, the greater the deformation of the lattice structure for ice-Ih. At 100 K, all lattice structure of ice-Ih remains essentially unchanged, showing as regular hexagon. Just a few ice-Ih structures could change, from regular hexagon to oblique hexagon, with increasing temperature from 100 K to 200 K. At 270 K, F_3 rises to 0.015, much more important than other cases, because a little ice-Ih structure significantly changed from regular hexagon to heptagon, pentagon, and oblique hexagon. This is due to the degree of long-range order of ice-Ih decreasing with increasing temperature (Figure 6-4 (a)).
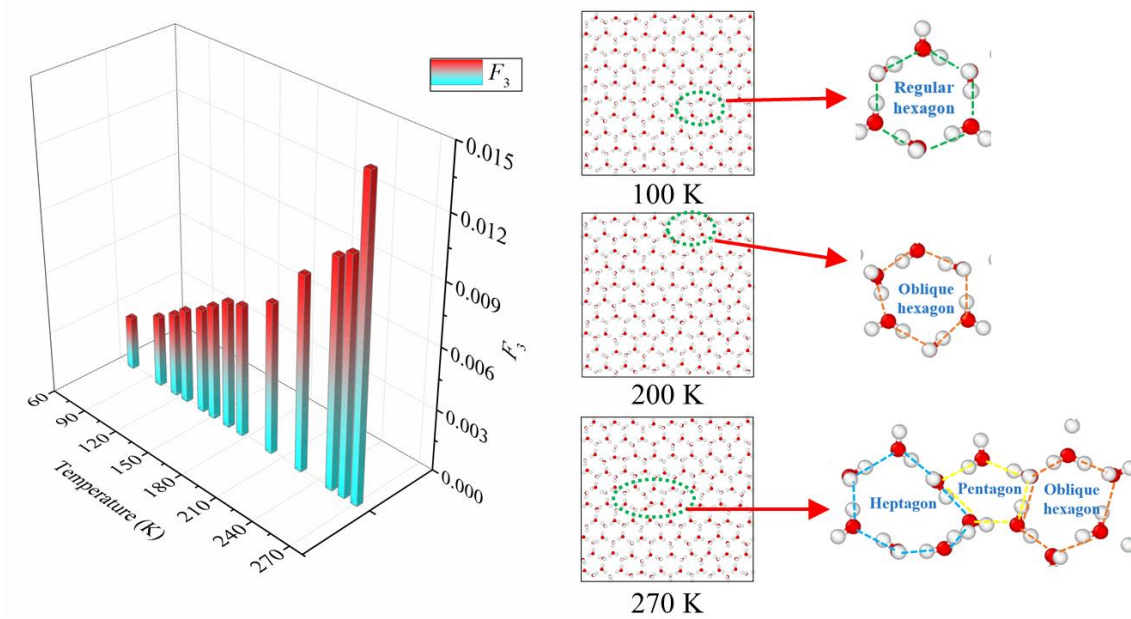
Figure 6-5. Evolution of order parameter (F_3) with temperature for the ice-Ih after relaxation.

6.3.1 Effect of temperature on tensile mechanical properties

6.3.1.1 Tensile stress-strain response

The stress-strain relationship under different temperatures is shown in Figure 6-6(a). As temperature increases, both the ultimate tensile strength and the ultimate tensile strain decline, indicating that the tensile mechanical properties of ice-Ih decrease with temperature. This phenomenon was also found in some previous researches, such as ice under compressive loading [208] and tensile loading [195], kaolinite under tensile load [216], as well as montmorillonite under complex conditions [217]. It illustrated that temperature plays a vital role in the mechanical behavior of ice, reducing the stability of the atomic structure. Moreover, the stress-strain curve was divided into three stages for better analysis, where the point O corresponds to the initial system without strain, and the point A, B, and C correspond to the tensile stage of ultimate tensile strength, under failure, and residual strength, respectively (Figure 6-6(a)).

On the other hand, the total potential energy of ice-Ih rises due to an external tensile force acting on the system, as shown in Figure 6-6(b). The changing trend of total potential energy

increment was nearly similar to one of the stress-strain curves (Figure 6-6(a)) at 73 ~ 200 K. It generally rose in OA stage, and then rapidly decreased in AB stage, finally remaining stable in BC stage. However, at the temperature range of 225 K to 270 K, it is noted that the changing trend of total potential energy increment was significantly different: 1) at 225 K, it increased firstly in OA stage and then slightly declined in AB stage, following by constantly rose in BC stage; 2) at 250 ~ 270 K, it rapidly increased with tensile strain to a maximum value in OA stage, and then floating around the maximum value in AB and BC stage. This evolution is related to the structural failure of ice-Ih under the tensile process, which will be discussed in the next section.

(a)   (b)
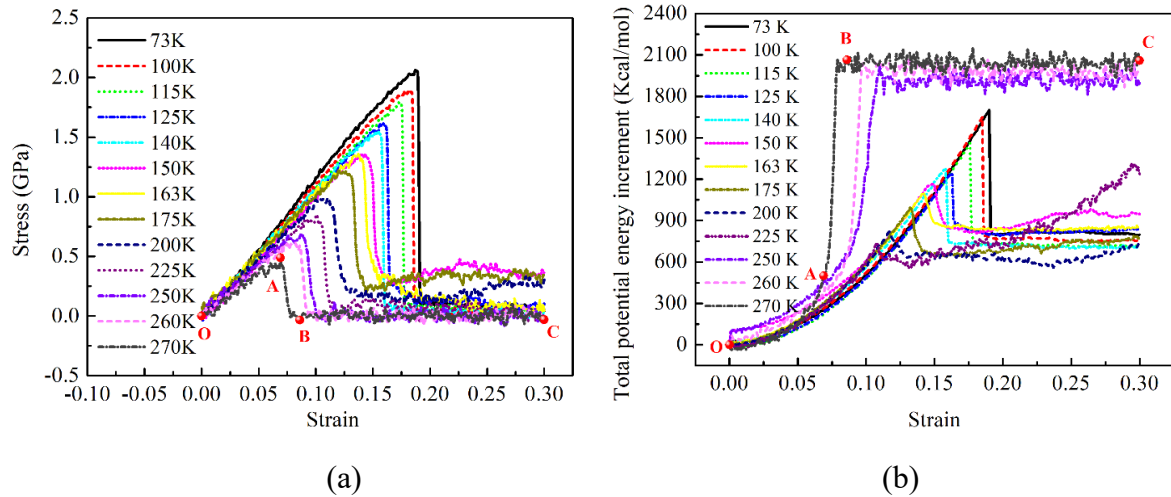
Figure 6-6. Evolution of (a) tensile stress and (b) total potential energy increment with strain for ice-Ih under different temperatures.

Young's modulus is obtained from the slope of the stress-strain curve (Figure 6-6(a)) at the strain of 0 ~ 0.05 in the elastic deformation stage. The Young's modulus of ice-Ih decreases linearly with temperature, as shown in Figure 6-7(a). Moreover, as shown in Table 6-1, Young's modulus in this work at 225 ~ 270 K are consistent with some previous simulation and experimental results, which were obtained by ultrasonic test [218], ground-penetrating radar (GPR) and seismic surveys [202, 219], MD simulation [193], finite element simulation (FEM) [203]. It could further validate the accuracy of the applied force field and established model.

124

As shown in Figure 6-7(b), the ultimate tensile strength declined linearly with increasing temperature, different from the previous result from Chen et al. [189], who found that the dynamic tensile strength of ice showed anomalous temperature effects (Pink dot in Figure 6-7(b)) under shock load with a high shock velocity. Although the evolution trend of ultimate tensile strength with temperature in this work is different from that of Chen et al. [189], its value is close, likely due to different loading modes and deformation rates. Moreover, at 225 K, the ultimate tensile strength of monocrystalline ice-Ih in this work is slightly superior to that of bicrystalline ice, and greatly more important than that of polycrystalline ice from Cao et al. [193]. It indicated that grain boundary reduced the mechanical properties of ice, which was consistent with Elvin [203], who found Young's modulus of ice without grain boundary superior to that of grain boundary using FEM. On the other hand, the negative relationship between ultimate tensile strain and temperature is nearly linear, implying that the higher temperature, the earlier the ice system may be melted.

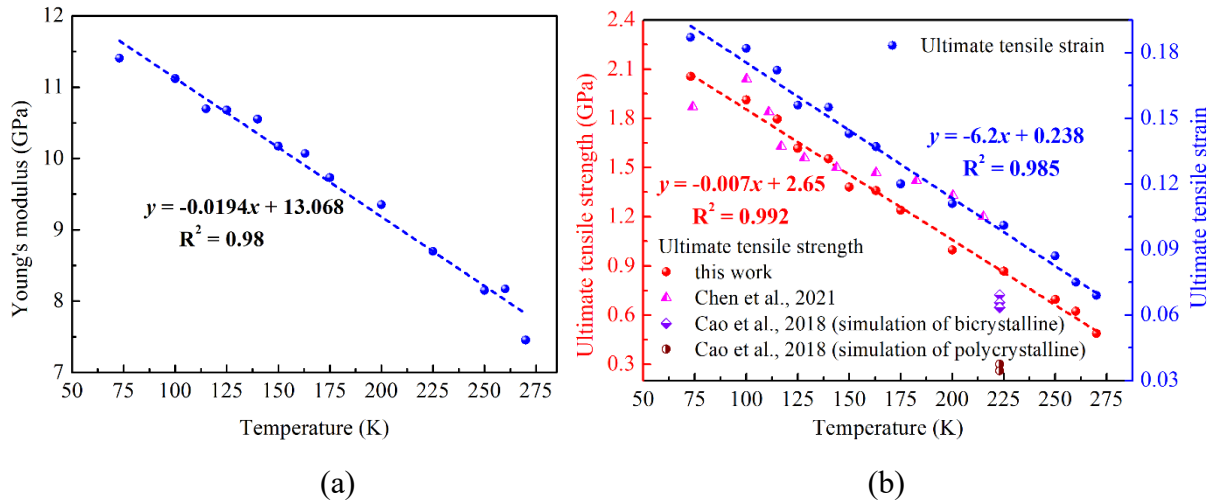(a)   (b)

Figure 6-7. Effect of temperature on (a) Young's modulus and (b) ultimate tensile strength as well as ultimate tensile strain of ice-Ih, where the "Chen et al., 2021" and "Cao et al., 2018" are corresponding to the literature [189] and [193], respectively.

Table 6-1. Young's modulus of ice at different temperatures compared to previous experimental and simulation results.

Young's modulus (GPa)	Notes
8.70, 8.16, 8.17, 7.46	MD simulation results in this work, at 225, 250, 260, and 270 K, respectively.
8.91 ~ 8.58 [218]	Through the ultrasonic test, at 234 ~ 263 K.
8.6 ~ 12 [202, 219]	Through ground penetrating radar (GPR) and seismic surveys for monocrystalline ice, at a temperature near the melting point.
7.6 ~ 9.1 [193]	Using MD simulation method for bicrystalline ice under both tensile and compression with a strain rate of $1 \times 10^8 \, s^{-1}$, at 223.15 K.
7.83, 9.58 [203]	Using finite element simulation (FEM) for polycrystalline ice, at 257.15 K, considering with/without grain boundary, respectively.
6.0 ~ 12.0 [220]	Measurements for the 0.5 and 1.2 m diameter plates for polycrystalline ice, at -7 ~ -37 ℃ (236 ~ 266 K), considering different temperatures, structural types, and grain sizes.
3.0 ~ 9.0 [190]	Young's modulus of polycrystalline ice, at 263 K.
9.1 ~ 9.5 [221]	Through pulse-transmission method for polycrystalline ice, at 260 K

6.3.1.2 Structural analysis of failure process

Figure 6-8 shows the structural failure and F_3 of ice-Ih at a tensile strain of 0.3 under different temperatures. Three failure forms could be observably divided. The solid phase exists at 73 ~ 140 K, as shown in Figure 6-8(a), where the structure of ice-Ih illustrated delamination damage, divided into the upper- and lower- portions, which is significantly similar to the failure form of some solid material, such as dry clay minerals [95, 216]. Moreover, the F_3 is less than 0.02 (Figure 6-8(d)), and more complete ice-Ih crystal structure still exists in the non-fractured zone. The solid-liquid phase coexisted at 150 ~ 225 K, where local ice-Ih atoms were melted under tensile loading, showing the coexistence of liquid water and ice phase. Moreover, the evolution of the melted area and F_3 of ice-Ih with temperature are close at 150 ~ 200 K, but those of 225 K rapidly increased, indicating that plenty of ice-Ih molecules is melted to liquid phase (Figure 6-8(b)). The liquid phase exists at 250 ~ 270 K, where the ice-Ih system was melted completely, and F_3 is nearly equal to 0.1, shown as liquid water phase (Figure 6-8(c)).

The solid-solid phase transformation at 73 ~ 140 K and solid-liquid phase transformation at 150 ~ 270 K were observed. This finding agrees well with the finding of Yin et al. [208], that ultrafast uniaxial compression was carried out using MD simulation. In this work, the ice-Ih system was close to solid-like brittle material at 73 ~ 140 K and solid-like plastic material at 150 ~ 225 K, showing brittle and plastic failure under tensile load, respectively. When the temperature was superior to 250 K, the ice-Ih system was easier to melt, indicating that the structural stability of ice-Ih was significantly affected by temperature.
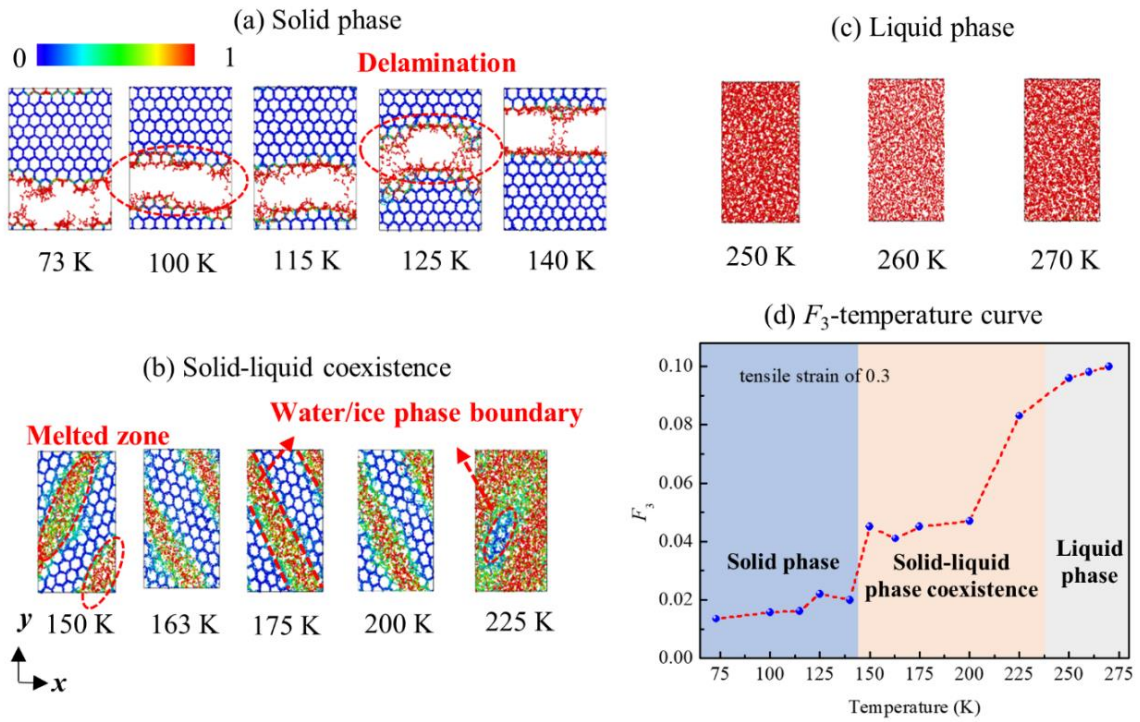
Figure 6-8. Structural failure diagram and order parameter (F_3) of ice-Ih at a tensile strain of 0.3: (a) Solid phase, from 73 to 140 K; (b) Solid-liquid coexistence, from 150 to 225 K; (c) Liquid phase, from 250 to 270 K; (d) F_3-temperature curve. In Figures (a ~d), atoms are colored according to the the normalized spatial distribution of the local strain, with less deformation as blue and more deformation as red. The strain tensor was computed using OVITO [222], considering the neighboring atoms within a distance of 4.5 Å.

On the other hand, there is a doubt whether the size effect affected the structural failure process of ice at 250 ~ 270 K. To this end, two established bigger ice-Ih models were conducted

for a tensile test at 260 K, including 5376 and 9720 water molecules, respectively. As shown in Figure 6-9 and Figure 6-10, the evolution of F_3 with strain for three different size of ice-Ih models and their structural failure diagram are close, which could indicate that the size effect does not affect the structural failure process of ice-Ih.

Figure 6-9. Evolution of F_3 with strain for three different size of ice-Ih models at 260 K.

Figure 6-10. Structural failure diagram for three different size of ice-Ih models at 260 K, corresponding to different tensile strains, including 0.05, 0.1, 0.2, and 0.3.

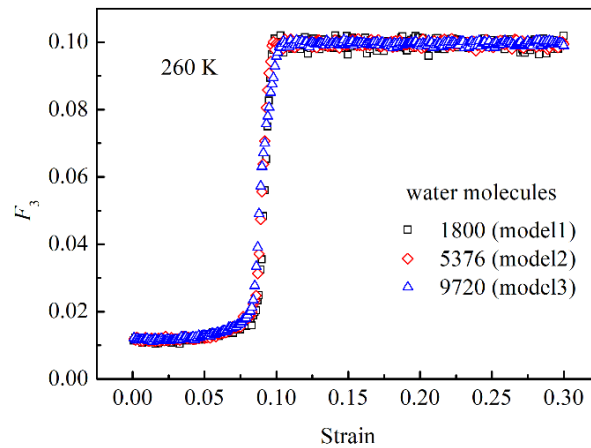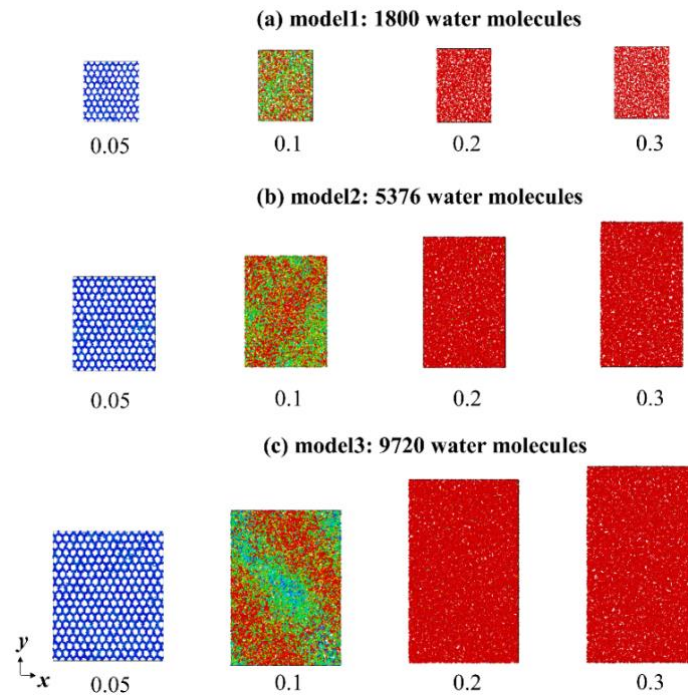To further explore the failure process of the atomic structure of ice-Ih under different tensile strains, the system under four different temperatures is studied, as shown in Figure 6-11. In OA stage, the crystal structure of ice-Ih was slightly stretched, from orthohexagonal ice into ice-variant. Afterward, in AB stage, the atomic structure of ice-Ih could be destroyed, showing different phase transformations under different temperatures.

As shown in Figure 6-11(a), at 73 K, the delamination of ice-Ih crystal structure was suddenly apparent with strain from 0.19 to 0.191, showing hydrogen bond-breakage and a large crack in AB and BC stage. Moreover, Figure 6-11(e) shows the F_3 less than 0.02 all the time. It showed brittle failure and solid-solid phase transformation, causing a loss of resistance to deformation. Thus, the residual strength was close to 0, corresponding to point C (Figure 6-6(a)).

At 150 and 225 K (Figure 6-11(b) and (c)), local ice-Ih molecules could generally melt with increasing tensile strain. And the solid-liquid phase transformation constantly developed, where the melting migration direction of ice-Ih moved along its unmelted zone. It is noted that the angle of inclination of the water-ice phase boundary was similar to a shear angle of rock or soil material under shear load [223-225].

At 250 K (see Figure 6-11(d)), ice-Ih molecules of over 50% were melted, and F_3 is about 0.05 at point B. When the strain is superior to 0.106, the F_3 is close to 0.1 (Figure 6-11(e)), indicating almost completely melting for ice-Ih system. The solid-liquid phase transformation was earlier and more complete to occur at this temperature. It is why total potential energy increment rapidly increased, and then kept stable at 250 ~ 270 K (see Figure 6-6(b)). On the other hand, the process of completely solid-liquid phase transformation at 250 ~ 270 K needed more energy than solid-solid phase transformation at 73 ~ 140 K, as shown in Figure 6-6(b).

Based on Figure 6-11(e) and Figure 6-6(b), the consistent evolution trend of total potential energy increment and F_3 with tensile strain is found, indicating the changing energy depending on the deformation of atomic structure. Moreover, these failure forms of ice-Ih structure in this work differed from previous results [189, 208], which considered different loading types and strain rates. It implies that the load type and strain rate played a significant role in the failure form of

atomic structure.
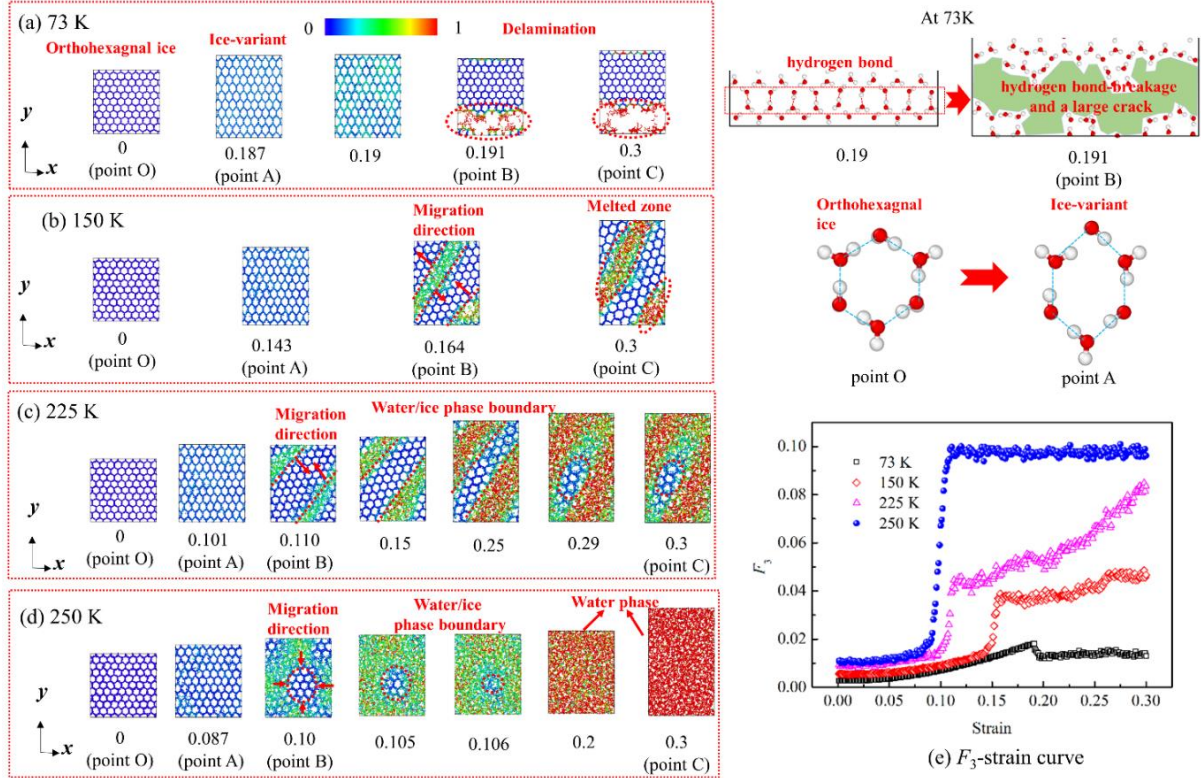
Figure 6-11. Evolution of atomic structure and order parameter (F_3) with strain for different temperatures: (a) 73 K; (b) 150 K; (c) 225 K; (d) 250 K; (e) F_3-strain curve.

6.3.2 Effect of confining pressure on tensile mechanical properties

6.3.2.1 Confining pressure effect on the stress-strain response

The confining pressure is a significant factor in the mechanical properties of ice in practical engineering, such as excavating tunnels and underground caverns in the cold area. In this work, the confining pressure is applied to the ice-Ih system along the *x*- and *z*-direction, and tensile load for the *y*-direction. As shown in Figure 6-12, the ultimate tensile strength and the ultimate tensile strain of ice-Ih declined with increasing confining pressure. The higher the confining pressure, the earlier and easier the ice-Ih structure is to be melted.

To precisely explore the effect of confining pressure and temperature on tensile mechanical

properties, the attenuation rate of the ultimate tensile strength of ice-Ih can be obtained by following equation. In this work, σ_i is the ultimate tensile strength at confining pressure of 1 atm, and one of 50 ~ 200 MPa set as σ_j. As shown in Table 6-2, the higher confining pressure or temperature, the more attenuation rate of ultimate tensile strength of ice-Ih. It indicated that temperature and confining pressure are critical factors for influencing the tensile mechanical properties of ice-Ih.

$$D_s = \frac{\sigma_i - \sigma_j}{\sigma_i} \times 100\% \tag{6-2}$$

where D_s represents the attenuation rate, σ_i and σ_j are the ultimate tensile strength at different conditions.

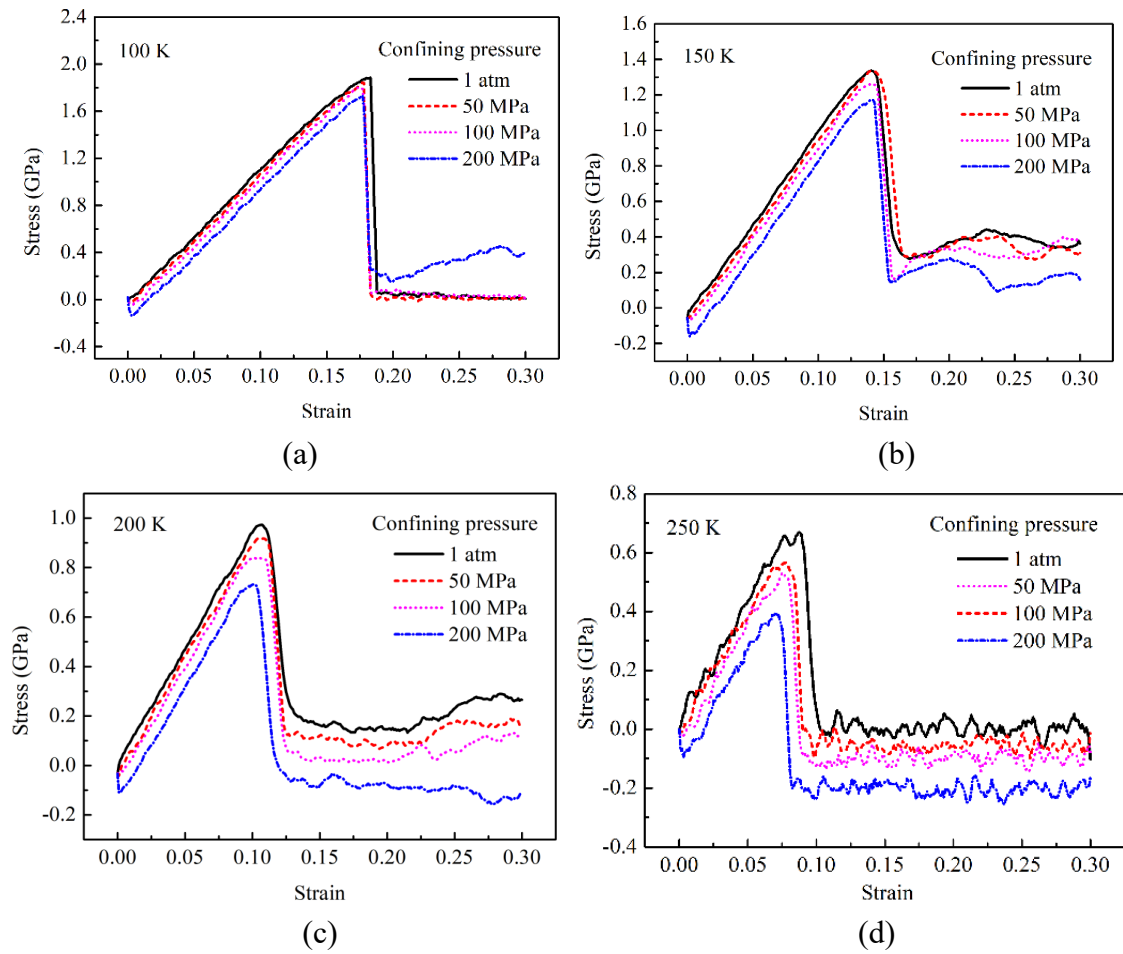Figure 6-12. Evolution stress with strain under different confining pressures and temperatures: (a) 100K; (b) 150K; (c) 200 K; (d) 250 K.

Table 6-2. Attenuation rate D_s (%) of ultimate tensile strength of ice, σ_i is the ultimate tensile strength at the confining pressure of 1 atm, and one of 50 ~ 200 MPa set as σ_j.

Confining pressure (MPa)	Temperature (K)			
	100	150	200	250
50	1.412%	-0.589%	5.115%	14.943%
100	4.812%	4.934%	11.635%	22.414%
200	8.159%	10.383%	21.866%	37.931%

6.3.2.2 Confining pressure effect on microstructure during failure process

To analyze the effect of confining pressure combined with temperature on the microstructure of ice-Ih, the structural failure diagram at a tensile strain of 0.3 and F_3-strain curve is shown in Figure 6-13. The solid-solid phase transformation was observed at 1 atm ~ 100 MPa and 100 K, but the solid-liquid phase transformation was shown in other cases. In Figure 6-13(a), at confining pressure of 1 atm ~ 100 MPa and 100 K, the whole layer delamination is found, so that the ice-Ih system loses its resistance to deformation in the z-direction. This is why the residual strength of ice-Ih is close to 0 in BC stage (Figure 6-12(a)).

As shown in Figure 6-13(a) ~ (c), at 200 MPa and 100 K, and all confining pressure and 150 K, as well as 1 atm ~ 100 MPa and 200 K, the residual strength of all above conditions are superior to 0 (Figure 6-12(a) ~ (c)), indicating that these ice-Ih systems still can resist deformation. It is due to the F_3 less than 0.06, that some ice-Ih atoms remained relatively intact in the unmelted zone. Furthermore, as shown in Figure 6-13(a), the high confining pressure promoting the solid-solid phase into the solid-liquid phase transformation is found at 100 K and confining pressure from 100 to 200 MPa.

As shown in Figure 6-13(c) ~ (d), at 200 MPa and 200 K, as well as all confining pressure and 250 K, their residual strengths are less than 0 (Figure 6-12(c) and (d)). At all confining pressure and 250 K (Figure 6-13(d)), the ice-Ih system is quickly melted from solid to liquid phase, and F_3 increases rapidly to around 0.1, resulting in losing the ability to resist deformation. On the other hand, at 200 MPa and 200 K, it is noted that the ice-Ih system did not melt entirely

into liquid phase, but the upper- and lower- melted zones in the ice-Ih system have been already connected (Figure 6-13(c)), resulting in becoming a mostly failure system. Thus, the F_3 increased again with a higher rate when the tensile strain was greater than 0.125.
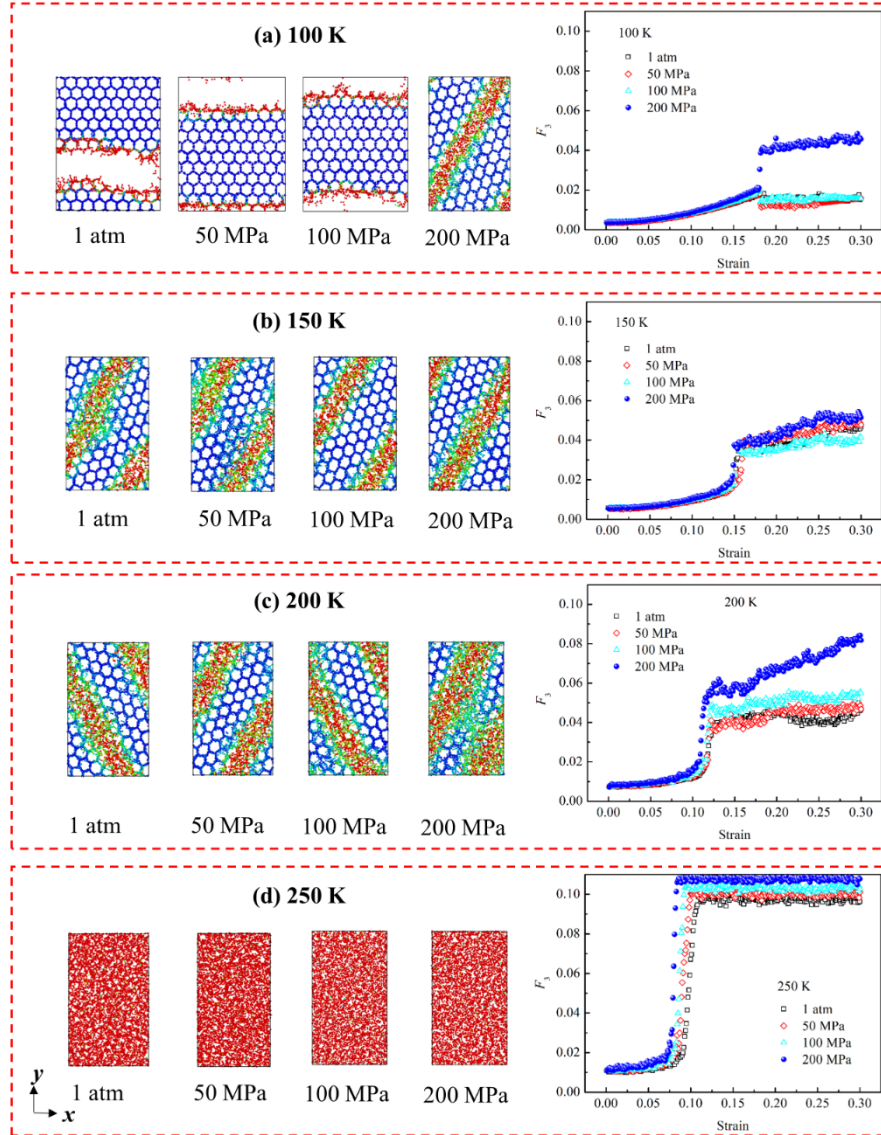
Figure 6-13. Structural failure diagram of ice-Ih at a tensile strain of 0.3 and the evolution of order parameter (F_3) with strain under different confining pressures (1 atm ~ 200 MPa) at temperatures: (a) 100 K; (b) 150 K; (c) 200 K; (d) 250 K.

Figure 6-14 shows the relationship between volumetric and axial strain under different temperatures and confining pressures. As shown in Figure 6-14(a), at solid-solid phase

transformation (corresponding to 100 K and 1 atm ~ 100 MPa), the volumetric strain slowly increased with axial strain from 0 to 0.18 in OA stage, followed by rapidly increased in AB stage, finally rose under a certain speed in BC stage (marked in Figure 6). This failure process of ice-Ih structure was similar to one of solid-like material, so that the simulation box in *x*- and *z*-direction remained unchanged, but that of *y*-direction could significantly change with tensile load (see Figure 6-13(a)).
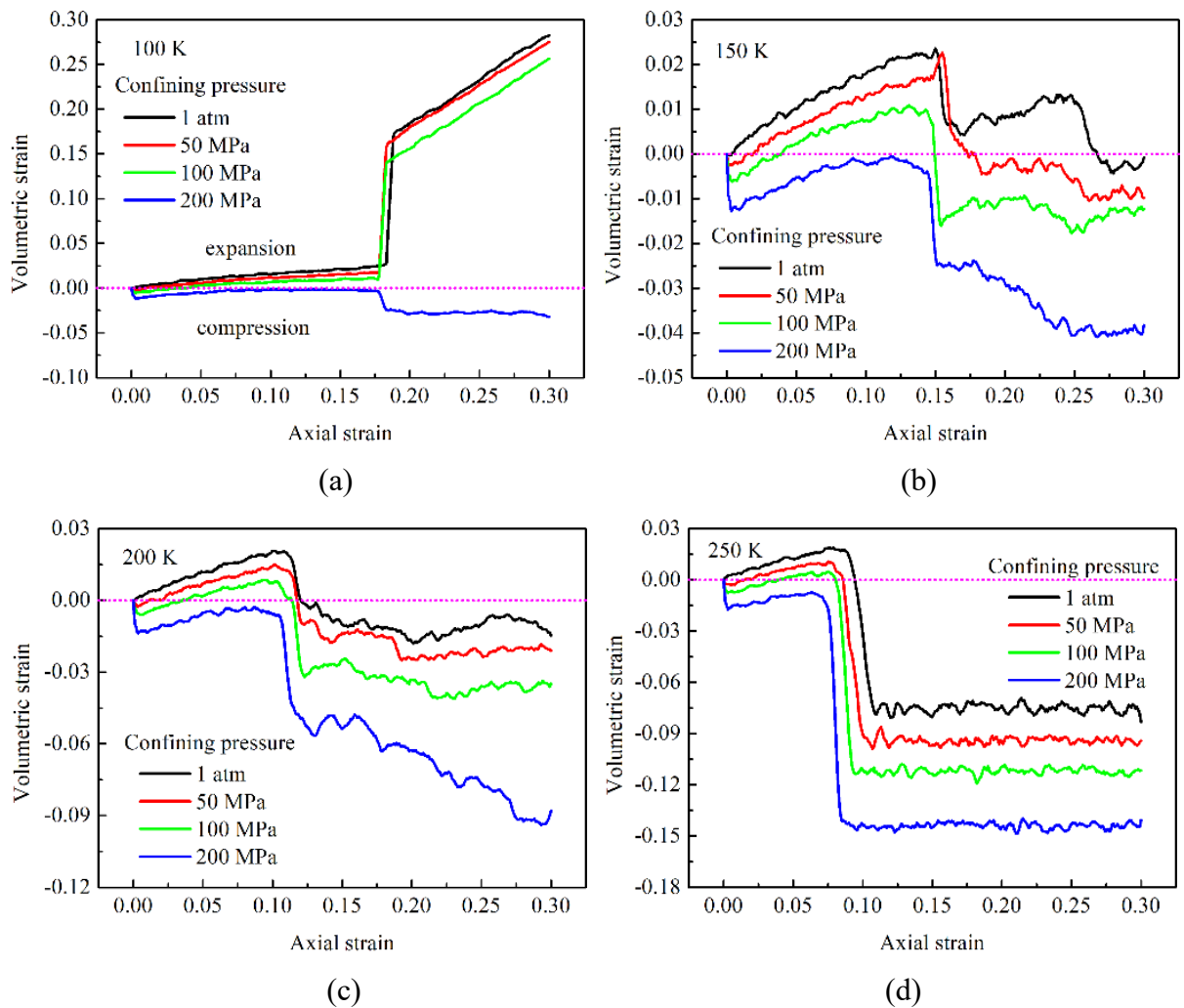
Figure 6-14. Evolution of volumetric strain with axial strain under different confining pressures and temperatures: (a) 100K; (b) 150K; (c) 200 K; (d) 250 K.

However, for other cases, the volumetric strain slowly rose in OA stage (see Figure 6), indicating the simulation box expanded along the tensile direction. And then, with increasing

axial strain, some ice-Ih crystal could be melted as liquid water, leading to more shrinkage of simulation box in x- and z-direction. Thus, the ice-Ih system was constantly shrinking after OA stage (Figure 6-14), where the AB stage was the most obvious, followed by BC stage. It could conclude that the higher confining pressure or temperature, the more significant shrinking of the ice-Ih system.

6.4 Conclusions

Molecular Dynamics simulations have been performed to investigate the tensile mechanical behavior of ice-Ih described by SPC/E model under different temperatures and confining pressures. This work could provide an insight into the understanding of ice science under low strain rates. The conclusions are obtained as follows:

(1) The Young's modulus, ultimate tensile strength, and ultimate tensile strain of ice-Ih decrease linearly with increasing temperature, indicating that temperature reduces the mechanical stability of the atomic structure. Moreover, the number of RDF peaks for global, O-H, H-H, and O-O atom pairs decrease with increasing temperature. It indicates that the higher temperature, the looser the atomic structure of ice-Ih, and the earlier and easier the ice-Ih system is melted.

(2) The strain rate plays an essential role in the relationship between mechanical strength and temperature. The temperature effect under tensile loading with a low strain rate is different from the previous result of Chen et al. [189] and Wu et al. [200], who found an anomalous temperature effect under shock- and compressive-load with a high strain rate, respectively.

(3) The solid-solid phase transformation of ice-Ih is observed at $73 \sim 140$ K, and the ice-Ih system is close to solid-like brittle material, showing brittle failure under tensile loading. The solid-liquid phase transformation is shown at $150 \sim 270$ K, and the ice-Ih is similar to solid-like plastic material, where the ice-Ih system was easier to melt at temperature superior to 250 K.

(4) The evolution of total potential energy increment with strain is significantly related to the phase transformation of ice-Ih under the failure process. The evolution of total potential energy

increment with strain for ice-Ih is mostly similar to that of the stress-strain curve at 73 ~ 200 K, due to solid-solid phase transformation or slight solid-liquid phase transformation. However, its anomalous change is observed at 225 ~ 270 K due to the earlier and more complete solid-liquid phase transformation.

(5) The confining pressure could reduce the mechanical properties of ice-Ih: the higher confining pressure, the earlier and more likely to be damaged for the ice-Ih structure. Moreover, the higher confining pressure could easily promote the solid-solid phase transformation into solid-liquid phase transformation at 100 K. Furthermore, at 100 K and confining pressure of 1 atm ~ 100 MPa, the volumetric strain of ice-Ih increased with strain. However, at other higher temperatures and confining pressure, the higher confining pressure or temperature, the more significant shrinking for ice-Ih.

Chapter 7. Summary and perspectives

7.1 Summary

This PhD dissertation is devoted to investigating the interfacial and frictional properties of expansive soil minerals and the deformation mechanism of bulk ice system through molecular dynamics (MD) simulation method. The main conclusions are obtained as following:

(1) The friction models of hydrated montmorillonite and quartz-quartz/clay-(water) interface were established, to reveal their friction mechanism in nanoscale and explore the nanotribology of geotechnical materials: (a) The low friction coefficient of 0 ~ 30% hydrated montmorillonite was 0.058 ~ 0.17, which was consistent with the previous simulation and experimental results, verifying the weak friction properties of montmorillonite. (b) The stick-slip effect existed during the friction process between soil/rock particles at nanoscale, it also was affected by normal load, sliding velocity, hydration, etc. (c) The increase of clay content could reduce the frictional strength of the mixture of quartz-clay. Similarly, the interlayer water could greatly weaken the interaction between clay layers. (d) The relationship between shear load and normal load for hydrated montmorillonite and quartz-quartz/clay-(water) interface was approximatively linear in nanoscale friction. (e) For quartz-montmorillonite system with different interlayer cations, the higher the radius of cation, the lower the friction coefficient, and the higher the cohesion.

(2) The Montmorillonite-unfrozen water-ice system was constructed to clarify the phase transformation process and structure changing of unfrozen water and ice on montmorillonite interface in microscale: (a) For the microstructure of unfrozen water and ice on clay particles, the division of "montmorillonite-bound water-cubic ice-hexagonal ice-cubic ice-'quasi-liquid' water-air" was determined. (b) The surface effect of clay is the main reason for the presence of unfrozen water in frozen soil, mainly including coulomb electrostatic and van der Waals interactions, where coulomb electrostatic interactions dominated. (c) With the increase in temperature, hydrogen bonds in ice system were broken due to thermal fluctuations, leading to the gradual transformation of ice into liquid water.

(3) The deformation and failure mechanism and phase transformation process of bulk ice system was studied, considering the coupling effect of temperature and pressure: (a) For bulk ice system, the solid-solid phase transformation was found at 73 ~ 140 K, and solid-liquid at 150 ~ 270 K. (b) The higher temperature, the looser the atomic structure of ice-Ih, and

the earlier and easier the ice-Ih system was melted. (c) The higher confining pressure, the earlier and more likely to be damaged for the ice-Ih structure.

7.2 Main innovation points

(1) MD simulation methods was applied to study geotechnical engineering problems, aiming to: a) elucidate the fundamental mechanism, b) explain experimental phenomena or data, and c) predict the behavior of materials. This work provided atomic/molecular level theoretical basis for studying the friction mechanism between expansive soil mineral particles and their interface properties.

(2) The friction models of hydrated montmorillonite and clay-quartz at microscale were proposed, and the relationships between their friction and normal load, sliding velocity, water content were determined. The friction mechanism of their interface in nanoscale was revealed, and the nano-tribology of geotechnical engineering materials was developed.

(3) The phase transformation process and structure composition of unfrozen water and ice on montmorillonite interface at microscale were clarified, and the deformation mechanism of bulk ice was revealed. This study provided a theoretical basis for the macroscale characterization of ice-water phase transformation in expansive soil minerals to establish the "micro-macro" theoretical relationship in frozen soil mechanics.

7.3 Prospect

The classical MD simulation method was used to study the interfacial and frictional properties of expansive soil minerals, as well as the deformation mechanism of bulk ice system, revealing the nanoscale friction and ice-water phase transformation mechanism on its interface. However, there are still some shortcomings in the work. Therefore, the following perspectives are proposed:

(1) This PhD dissertation lacked some relevant experimental data due to time constraints. Currently, more comparative analyses were based on previous research results to verify the accuracy of the established model.

(2) Expensive soil contained various minerals, not only montmorillonite, kaolinite, quartz, etc. At present, most of the studies were conducted for one or two mineral systems, which cannot objectively reflect the actual soil conditions. Moreover, the heterogeneity and complexity of geotechnical materials are a big challenge for atomic models in nanoscale, so it is necessary to develop appropriate multi-scale research methods.

(3) Developing multi-scale research methods: (a) developing coarse-grained molecular

dynamics and near-field dynamics, and establishing coarse-grained models of geotechnical materials to develop towards a larger scale. (b) Developing a new ReaxFF force field suitable for montmorillonite system: At present, CLAYFF force field was more used to describe the interaction of clay minerals, but it cannot reflect the process of bond fracture and rearrangement. If the chemical reaction between different substances (i.e., bond fracture and formation) is to be considered, the ReaxFF force field must be employed. However, the current ReaxFF force field could only be used to describe kaolinite or montmorillonite without isomorphic substitution (i.e., pyrophyllite). Therefore, it is necessary to develop a new ReaxFF force field suitable for the montmorillonite system after isomorphic substitution.

(4) Continuing to explore the nano-tribology of geotechnical materials: the research on the friction behavior of clay minerals in microscale is a new field that needs to be developed urgently. The primary analysis is the interface friction of hydrated montmorillonite and clay-quartz-(water) system, and the friction characteristics between clay minerals with weak friction properties and other minerals (e.g., quartz) are also worth exploring. This is of great significance for understanding the properties of seismic fault zones or the creep of natural faults.

(5) Exploring the issue of ice water phase transition between clay nanopores: In actual frozen soil, there is still interaction between soil particles. Therefore, it is necessary to study the ice-water phase transition process and the distribution of unfrozen water and ice between clay nanopores, and establish a system - "clay-unfrozen water-ice-unfrozen water-clay".

References

[1]   YAO H, LU J, BIAN H, et al. Influence of microwave heating on the swelling properties of expansive soil in Hefei[J]. Case Studies in Thermal Engineering, 2022,39: 102466.

[2]   Pei Xincheng Study on the Effects of Acid Rain on the Physical and Mechanical Properties and Microstructure of Expansive Soil in the Danjiangkou Reservoir Area [D] Guilin University of Technology, 2022

[3]   Leng Ting, Tang Chaosheng, Xu Dan, etc Research progress on engineering geological characteristics of expansive soil [J] Journal of Engineering Geology, 2018,26 (01): 112-128

[4]   Yin Zongze, Yuan Junping, Wei Jie, et al On the influence of cracks on the stability of expansive soil slopes [J] Journal of Geotechnical Engineering, 2012,34 (12): 2155-2161

[5]   Yang Wenqi, Zhou Cheng, Wang Lin, et al Stability analysis of expansive soil slopes considering expansion thrust under rainfall [J] Journal of Disaster Prevention and Reduction Engineering, 2018,38 (05): 874-880

[6]   WANG Y, ZHANG A, REN W, et al. Study on the soil water characteristic curve and its fitting model of Ili loess with high level of soluble salts[J]. Journal of Hydrology, 2019,578: 124067.

[7]   IDIART A, LAVINA M, COCHEPIN B, et al. Hydro-chemo-mechanical modelling of long-term evolution of bentonite swelling[J]. Applied clay science, 2020,195: 105717.

[8]   ZHAN J, WANG Q, ZHANG W, et al. Soil-engineering properties and failure mechanisms of shallow landslides in soft-rock materials[J]. Catena (Giessen), 2019,181: 104093.

[9]   HONG W, MENG J, LI C, et al. Effects of Temperature on Structural Properties of Hydrated Montmorillonite: Experimental Study and Molecular Dynamics Simulation[J]. Advances in Civil Engineering, 2020,2020: 1-11.

[10]   ZHU L, SHEN W, SHAO J, et al. Insight of molecular simulation to better assess deformation and failure of clay-rich rocks in compression and extension[J]. International Journal of Rock Mechanics and Mining Sciences, 2021,138: 104589.

[11]   ZHANG F, XIE S Y, HU D W, et al. Effect of water content and structural anisotropy on mechanical property of claystone[J]. Applied Clay Science, 2012,69: 79-86.

[12]   LIU Z, SHAO J, XIE S, et al. Mechanical Behavior of Claystone in Lateral Decompression Test and Thermal Effect[J]. Rock Mechanics and Rock Engineering, 2019,52(2): 321-334.

[13]   LIU Z B, XIE S Y, SHAO J F, et al. Effects of deviatoric stress and structural anisotropy on compressive creep behavior of a clayey rock[J]. Applied Clay Science, 2015,114: 491-496.

[14]   WEI P, ZHANG L, ZHENG Y, et al. Nanoscale friction characteristics of hydrated montmorillonites using molecular dynamics[J]. Applied Clay Science, 2021,210: 106155.

[15]   ZHENG Y, ZAOUI A. Mechanical behavior in hydrated Na-montmorillonite clay[J]. Physica A: Statistical Mechanics and its Applications, 2018,505: 582-590.

[16]   ZHENG Y, ZAOUI A. How water and counterions diffuse into the hydrated montmorillonite[J]. Solid State Ionics, 2011,203(1): 80-85.

[17]   SHIMAMOTO T, LOGAN J M. Effects of simulated clay gouges on the sliding behavior of Tennessee

Sandstone[J]. Tectonophysics, 1981,75(3-4): 243-255.

[18]   SUMMERS R, BYERLEE J. A note on the effect of fault gouge composition on the stability of frictional sliding[J]. International Journal of Rock Mechanics and Mining Sciences & Geomechanics Abstracts, 1977,14(3): 155-160.

[19]   TETSUKA H, KATAYAMA I, SAKUMA H, et al. Effects of humidity and interlayer cations on the frictional strength of montmorillonite[J]. Earth, Planets and Space, 2018,70(1).

[20]   SAKUMA H, LOCKNER D A, SOLUM J, et al. Friction in clay-bearing faults increases with the ionic radius of interlayer cations[J]. Communications Earth & Environment, 2022,3(1).

[21]   FULTON P M, BRODSKY E E, KANO Y, et al. Low Coseismic Friction on the Tohoku-Oki Fault Determined from Temperature Measurements[J]. Science, 2013,342(6163): 1214-1217.

[22]   UJIIE K, TANAKA H, SAITO T, et al. Low Coseismic Shear Stress on the Tohoku-Oki Megathrust Determined from Laboratory Experiments[J]. Science, 2013,342(6163): 1211-1214.

[23]   KRIM J. Friction at the atomic scale[J]. Scientific American, 1996,275(53): 74-80.

[24]   Ling Xianchang, Luo Jun, Geng Lin, etc A coupled frost heave model of water heat deformation for unsaturated expansive soil in seasonally frozen soil regions [J] Journal of Geotechnical Engineering, 2022,44 (7): 11

[25]   Gao Xiaoyun, Liu Jiaguo, Zhao Guitao, et al The effect of dry wet freeze-thaw cycles under low stress conditions on the strength of expansive soil in seasonally frozen regions [J] Journal of Water Resources and Building Engineering, 2019,17 (02): 24-28

[26]   ZHAO G, ZOU W, HAN Z, et al. Evolution of soil-water and shrinkage characteristics of an expansive clay during freeze-thaw and drying-wetting cycles[J]. Cold Regions Science and Technology, 2021,186: 103275.

[27]   ZHANG C, LIU Z, DENG P. Using molecular dynamics to unravel phase composition behavior of nano-size pores in frozen soils: Does Young–Laplace equation apply in low temperature range?[J]. Canadian Geotechnical Journal, 2018,55(8): 1144-1153.

[28]   REN Z, LIU J, JIANG H, et al. Experimental study and simulation for unfrozen water and compressive strength of frozen soil based on artificial freezing technology[J]. Cold Regions Science and Technology, 2023,205: 103711.

[29]   Liu Yong Unfrozen water testing and molecular simulation study of typical clay minerals [D] Geotechnical Engineering, China University of Mining and Technology, 2019.

[30]   Liu Shan Experimental Study on Mechanical Properties and Microscopic Morphology of Structural Clay [D] China University of Mining and Technology, 2014.

[31]   BOBKO C P. Assessing the mechanical microstructure of shale by nanoindentation; the link between mineral composition and mechanical properties[Z]. 2008.

[32]   VANORIO T, PRASAD M, NUR A. Elastic properties of dry clay mineral aggregates, suspensions and sandstones[J]. Geophysical Journal International, 2003,155(1): 319-326.

[33]   GREATHOUSE J A, CYGAN R T. Molecular Simulation of Clay Minerals[J]. Developments in Clay Science, 2013,5: 405-423.

[34]   Yang Yu, Xu Guoyuan Molecular dynamics simulation study on the tensile mechanical properties of hydrated montmorillonite [J] Journal of Civil and Environmental Engineering (Chinese and English),

2022: 1-12

[35]   Yang Yu, Xu Guoyuan Molecular dynamics simulation of hydration and swelling mechanisms in the inner layer of mixed layer clay [J] Mining Research and Development, 2022, 42 (12): 92-99

[36]   ZHU L P, SHEN W Q, HE M C, et al. Contribution of atomistic study to better understand water saturation effect on mechanical behavior of clayey rocks in triaxial compression[J]. Computers and Geotechnics, 2022,146: 104738.

[37]   KANG X, SUN H, YANG W, et al. Wettability of clay aggregates—A coarse-grained molecular dynamic study[J]. Applied Surface Science, 2020,532: 147423.

[38]   DU J, ZHOU A, SHEN S, et al. Revealing crucial effects of temperature and salinization on swelling behavior of montmorillonite[J]. Chemical Engineering Journal, 2022,429: 132263.

[39]   LI C, XU Y, YANG Y, et al. Evolution of Chemical Bonding and Crystalline Swelling–Shrinkage of Montmorillonite upon Temperature Changes Probed byin Situ   Fourier Transform Infrared Spectroscopy and X-ray Diffraction[J]. Langmuir, 2022.

[40]   Wang Wenming A Study on the Micromechanical Properties of Na Montmorillonite Based on Molecular Dynamics [D] Southwest Jiaotong University, 2021

[41]   Li Guoqing, Qiu Jun, Liu Dongliang Progress in molecular simulation research on montmorillonite [J] Comprehensive Utilization of Mineral Resources, 2019

[42]   ZHENG Y. Modélisation et simulation à l'échelle nanométrique de l'effet de température, de pression et des polluants sur l'argile hydratée de type montmorillonite[D]. Université Lille1 Sciences et Technologies, 2009.

[43]   MARSHALL, EDMUND C. The Physical Chemistry and Mineralogy of Soils. Volume 1[J]. Soil Science, 1965,99(5): 355.

[44]   YANG W, ZAOUI A. Uranyl adsorption on (001) surfaces of kaolinite: A molecular dynamics study[J]. Applied Clay Science, 2013,80-81: 98-106.

[45]   CHEN Z, HU L. Adsorption of Naphthalene on Clay Minerals: A Molecular Dynamics Simulation Study[J]. Materials, 2022,15(15): 5120.

[46]   ANCIAN B, BERNARD O, CHEVALET J, et al. Pierre Turq, an inspirational scientist in charge and at interfaces[J]. Molecular Physics, 2014,112(9-10): 1213-1221.

[47]   BUYUKOZTURK O. Multiscale framework for translating atomistic behavior to engineering scales[EB/OL]. [2023/02/19]. http://web.mit.edu/liss/mechanicsofconcrete.html.

[48]   FRENKEL D, SMIT B. Understanding molecular simulation: From algorithms to applications[M]. Academic Press, 2001.

[49]   YANG W. Interactions de radionucléides et de CO2 avec les argiles: mécanismes à élucider à l'échelle nanométrique[J]. 2014.

[50]   PLIMPTON S. Fast Paraller Algorithms for Short-Range Molecular Dynamics[J]. journal of computational physics, 1995,117: 1-19.

[51]   Yang Hua Molecular dynamics study on the thermodynamic behavior of active polymers [D] Beijing Jiaotong University, 2016

[52]   CYGAN R T, LIANG J, KALINICHEV A G. Molecular Models of Hydroxide, Oxyhydroxide, and Clay Phases and the Development of a General Force Field[J]. The Journal of Physical Chemistry B,

2004,108(4): 1255-1266.

[53]   CYGAN R T, GREATHOUSE J A, KALINICHEV A G. Advances in Clayff Molecular Simulation of Layered and Nanoporous Materials and Their Aqueous Interfaces[J]. The Journal of Physical Chemistry C, 2021,125(32): 17573-17589.

[54]   SEPPÄLÄ A, PUHAKKA E, OLIN M. Effect of layer charge on the crystalline swelling of Na+ , K+and Ca2+ montmorillonites: DFT and molecular dynamics studies[J]. Clay Minerals, 2016,51(2): 197-211.

[55]   AL-ZAOARI K, ZHENG Y, WEI P, et al. Early stage of swelling process of dehydrated montmorillonite through molecular dynamics simulation[J]. Materials Chemistry and Physics, 2022,283: 126015.

[56]   BERENDSEN H J C, GRIGERA J R, STRAATSMA T P. The missing term in effective pair potentials[J]. The Journal of Physical Chemistry, 1987,91(24): 6269-6271.

[57]   SMITH D E, DANG L X. Computer simulations of NaCl association in polarizable water[J]. The Journal of chemical physics, 1994,100(5): 3757-3766.

[58]   BERENDSEN H J C, POSTMA J P M, GUNSTEREN W F V, et al. Interaction models for water in relation to protein hydration in Intermolecular forces[J]. Springer Netherlands, 1981.

[59]   ABASCAL J L F, SANZ E, GARCÍA FERNÁNDEZ R, et al. A potential model for the study of ices and amorphous water: TIP4P/Ice[J]. The Journal of Chemical Physics, 2005,122(23): 234511.

[60]   ABASCAL J L F, VEGA C. A general purpose model for the condensed phases of water: TIP4P/2005[J]. The Journal of Chemical Physics, 2005,123(23): 234505.

[61]   SKLOGWIKI.   TIP4P/Ice   model   of   water[EB/OL].   [08/03/2023]. http://www.sklogwiki.org/SklogWiki/index.php/TIP4P/Ice_model_of_water.

[62]   JARZYNSKI C. Nonequilibrium Equality for Free Energy Differences[J]. Physical review letters, 1997,78(14): 2690-2693.

[63]   WANG P, DUAN Y, ZHENG H, et al. Molecular structure and dynamics of water on the surface of cement hydration products: Wetting behavior at nanoscale[J]. Applied Surface Science, 2023,611: 155713.

[64]   BÁEZ L A, CLANCY P. Computer Simulation of the Crystal Growth and Dissolution of Natural Gas Hydrates[J]. Annals of the New York Academy of Sciences, 1994,715(1): 177-186.

[65]   CLANCY T C, MATTICE W L. Computer simulation of polyolefin interfaces[J]. Computational & theoretical polymer science, 1999,9(3-4): 261-270.

[66]   NGUYEN A H, MOLINERO V. Identification of Clathrate Hydrates, Hexagonal Ice, Cubic Ice, and Liquid Water in Simulations: the CHILL+ Algorithm[J]. The Journal of Physical Chemistry B, 2015,119(29): 9369-9376.

[67]   MALKIN T L, MURRAY B J, SALZMANN C G, et al. Stacking disorder in ice I[J]. Physical Chemistry Chemical Physics, 2015,17(1): 60-76.

[68]   HONDOH T. Dislocation mechanism for transformation between cubic ice Ic and hexagonal ice Ih[J]. Philosophical magazine (Abingdon, England), 2015,95(32): 3590-3620.

[69]   HIRONO T, TSUDA K, KANEKI S. Role of Weak Materials in Earthquake Rupture Dynamics[J]. Scientific Reports, 2019,9(1).

[70]   KUBO T, KATAYAMA I. Effect of temperature on the frictional behavior of smectite and illite[J]. Journal of Mineralogical and Petrological Sciences, 2015,110(6): 293-299.

[71] BEHNSEN J, FAULKNER D R. Permeability and frictional strength of cation-exchanged montmorillonite[J]. Journal of Geophysical Research: Solid Earth, 2013,118(6): 2788-2798.

[72] MORROW C A, MOORE D E, LOCKNER D A. Frictional strength of wet and dry montmorillonite[J]. Journal of Geophysical Research: Solid Earth, 2017,122(5): 3392-3409.

[73] SAFFER D M, FRYE K M, MARONE C, et al. Laboratory results indicating complex and potentially unstable frictional behavior of smectite clay[J]. Geophysical research letters, 2001,28(12): 2297-2300.

[74] TEMBE S, LOCKNER D A, WONG T. Effect of clay content and mineralogy on frictional sliding behavior of simulated gouges: Binary and ternary mixtures of quartz, illite, and montmorillonite[J]. Journal of Geophysical Research, 2010,115(B3).

[75] OOHASHI K, HIROSE T, TAKAHASHI M, et al. Dynamic weakening of smectite-bearing faults at intermediate velocities: Implications for subduction zone earthquakes[J]. Journal of Geophysical Research: Solid Earth, 2015,120(3): 1572-1586.

[76] ABBASI B, MUHUNTHAN B, SALEHINIA I, et al. Nanoscale Stick-Slip Behavior of Na-Montmorillonite Clay[J]. Journal of Engineering Mechanics, 2020,146(12): 4020138.

[77] HÖLSCHER H, SCHIRMEISEN A, SCHWARZ U D. Principles of atomic friction: from sticking atoms to superlubric sliding[J]. Philosophical Transactions of the Royal Society A: Mathematical, Physical and Engineering Sciences, 2008,366(1869): 1383-1404.

[78] ERLANDSSON R, HADZIIOANNOU G, MATE C M, et al. Atomic scale friction between the muscovite mica cleavage plane and a tungsten tip[J]. Journal of Chemical Physics, 1988,89(8): 5190-5193.

[79] BHUSHAN B, KULKARNI A V. Effect of normal load on microscale friction measurements[J]. Thin Solid Films, 1996,278(1): 49-56.

[80] SIRONG Y, ZHONGZHEN Y, YIU-WING M. Effects of SEBS-g-MA on tribological behaviour of nylon 66/organoclay nanocomposites[J]. Tribology International, 2007,40(5): 855-862.

[81] COOK E H, BUEHLER M J, SPAKOVSZKY Z S. Mechanism of friction in rotating carbon nanotube bearings[J]. Journal of the Mechanics and Physics of Solids, 2013,61(2): 652-673.

[82] SUN W, MAI Y. Molecular dynamics simulations of friction forces between silica nanospheres[J]. Computational Materials Science, 2019,162: 96-110.

[83] YAPHARY Y L, YU Z, LAM R H W, et al. Molecular dynamics simulations on adhesion of epoxy-silica interface in salt environment[J]. Composites Part B: Engineering, 2017,131: 165-172.

[84] DUNCKLE C G, ALTFEDER I B, VOEVODIN A A, et al. Temperature dependence of single-asperity friction for a diamond on diamondlike carbon interface[J]. Journal of Applied Physics, 2010,107(11): 114903.

[85] LENG Y, CUMMINGS P T. Shear dynamics of hydration layers[J]. The Journal of Chemical Physics, 2006,125(10).

[86] XU W, YIN Z, ZHENG Y. Investigating silica interface rate-dependent friction behavior under dry and lubricated conditions with molecular dynamics[J]. Acta Geotechnica, 2023.

[87] WEI P, XIONG Y, ZHENG Y, et al. Nanoscale friction at the quartz-quartz/kaolinite interface[J]. Colloids and Surfaces A: Physicochemical and Engineering Aspects, 2023,676: 132296.

[88] IKARI M J, SAFFER D M, MARONE C. Effect of hydration state on the frictional properties of

montmorillonite-based fault gouge[J]. Journal of Geophysical Research, 2007,112(B6).

[89]   SAKUMA H, KAWAI K, KATAYAMA I, et al. What is the origin of macroscopic friction?[J]. Sci Adv, 2018,4(12): v2268.

[90]   SAKUMA H, KAWAI K, KOGURE T. Interlayer energy of pyrophyllite; implications for macroscopic friction[J]. The American mineralogist, 2020,105(8): 1204-1211.

[91]   VIANI A, GUALTIERI A F, ARTIOLI G. The nature of disorder in montmorillonite by simulation of X-ray powder patterns[J]. American Mineralogist, 2002,87: 966-975.

[92]   WEI P, ZHENG Y, XIONG Y, et al. Effect of water content and structural anisotropy on tensile mechanical properties of montmorillonite using molecular dynamics[J]. Applied Clay Science, 2022,228: 106622.

[93]   ZHANG S, PEI H. Determining the bound water content of montmorillonite from molecular simulations[J]. Engineering Geology, 2021,294: 106353.

[94]   LI H, BRANICIO P S. Ultra-low friction of graphene/C60/graphene coatings for realistic rough surfaces[J]. Carbon, 2019,152: 727-737.

[95]   ZHANG L, ZHENG Y, WEI P, et al. Nanoscale mechanical behavior of kaolinite under uniaxial strain conditions[J]. Applied Clay Science, 2021,201: 105961.

[96]   Li Yucheng, Chen Yonggui, Liu Li, et al Research progress on multi-scale expansion properties of high-pressure compacted bentonite [J] Journal of Geotechnical Engineering, 2023: 1-9.

[97]   FRENKEL D, SMIT B, TOBOCHNIK J, et al. Understanding Molecular Simulation[J]. Computers in Physics, 1997,11(4): 351.

[98]   DARDEN T, YORK D, PEDERSEN L. Particle mesh Ewald: An N·log(N) method for Ewald sums in large systems[J]. Journal of Chemical Physics, 1993,98(12): 10089-10092.

[99]   SCHNEIDER T, STOLL E. Molecular-dynamics study of a three-dimensional one-component model for distortive phase transitions[J]. Physical Review B, 1978,17(3): 1302-1322.

[100] GAO J, LUEDTKE W D, GOURDON D, et al. Frictional Forces and Amontons' Law: From the Molecular to the Macroscopic Scale[J]. The Journal of Physical Chemistry B, 2004,108(11): 3410-3425.

[101] WANG J, LIU Y, YANG C, et al. Modeling the Viscoelastic Behavior of Quartz and Clay Minerals in Shale by Nanoindentation Creep Tests[J]. Geofluids, 2022,2022: 1-16.

[102] ZHANG G, WEI Z, FERRELL R. Elastic modulus and hardness of muscovite and rectorite determined by nanoindentation[J]. Applied Clay Science, 2009,43(2): 271-281.

[103] XU W Q, YIN Z Y, ZHENG Y Y. FRP–soil interfacial mechanical properties with molecular dynamics simulations: Insights into friction and creep behavior[J]. International Journal for Numerical and Analytical Methods in Geomechanics, 2023.

[104] WEI P, ZHENG Y, ZAOUI A, et al. Atomistic study on thermo-mechanical behavior and structural anisotropy of montmorillonite under triaxial tension and compression[J]. Applied Clay Science, 2023,233: 106817.

[105] PENG C, WANG G, QIN L, et al. Molecular dynamics simulation of NH4-montmorillonite interlayer hydration: Structure, energetics, and dynamics[J]. Applied clay science, 2020,195: 105657.

[106] MORROW C P, YAZAYDIN A Ö, KRISHNAN M, et al. Structure, Energetics, and Dynamics of Smectite Clay Interlayer Hydration: Molecular Dynamics and Metadynamics Investigation of Na-

Hectorite[J]. The Journal of Physical Chemistry C, 2013,117(10): 5172-5187.

[107] CHÁVEZ-PÁEZ M, Van WORKUM K, de PABLO L, et al. Monte Carlo simulations of Wyoming sodium montmorillonite hydrates[J]. The Journal of chemical physics, 2001,114(3): 1405-1413.

[108] Kuang Lianfei, Zhou Guoqing, Shang Xiangyu, et al Molecular dynamics simulation of interlayer water molecular structure in sodium montmorillonite [J] Journal of Coal Science, 2013,38 (03): 418-423

[109] FU M H, ZHANG Z Z, LOW P F. Changes in the Properties of a Montmorillonite-Water System during the Adsorption and Desorption of Water: Hysteresis1[J]. Clays & Clay Minerals, 1990,38(5): 485-492.

[110] BEREND I, CASES J, FRANCOIS M, et al. Mechanism of adsorption and desprotion of water vapor by homoionic montmorillonites. II: The Li+, Na+, K+, Rb+, and Cs+-exchanged forms[J]. Clays and Clay Minerals, 1995,43(3): 324-336.

[111] KARABORNI S, SMIT B, HEIDUG W, et al. The Swelling of Clays: Molecular Simulations of the Hydration of Montmorillonite[J]. Science, 1996,271(5252): 1102-1104.

[112] CHANG F C, SKIPPER N T, SPOSITO G. Computer Simulation of Interlayer Molecular Structure in Sodium Montmorillonite Hydrates[J]. Langmuir, 1995,11(7): 2734-2741.

[113] BOEK E S, COVENEY P V, SKIPPER N T. Monte Carlo Molecular Modeling Studies of Hydrated Li-, Na-, and K-Smectites: Understanding the Role of Potassium as a Clay Swelling Inhibitor[J]. Journal of the American Chemical Society, 1995,117(50): 12608-12617.

[114] MARRY V, TURQ P, CARTAILLER T, et al. Microscopic simulation of structure and dynamics of water and counterions in a monohydrated montmorillonite[J]. The Journal of Chemical Physics, 2002,117(7): 3454-3463.

[115] KOSAKOWSKI G, CHURAKOV S V, THOENEN T. Diffusion of Na and Cs in montmorillonite[J]. Clays and Clay Minerals, 2008,56(2): 190-206.

[116] PORION P, MICHOT L J, FAUGERE A M, et al. Structural and dynamical properties of the water molecules confined in dense clay sediments: A study combining H-2 NMR spectroscopy and multiscale numerical modeling[J]. Journal of Physical Chemistry C, 2007,111(14): 5441-5453.

[117] ISABELLE, BEREND, JEAN-MAURICE, et al. Mechanism of adsorption and desorption of water vapor by homoionic montmorillonites; 2, The Li (super +) , Na (super +) , K (super +) , Rb (super +) and Cs (super +) -exchanged forms[J]. Clays and Clay Minerals, 1995,43(3): 324-336.

[118] CALVET R. Hydration of montmorillonite and diffusion of exchangeable cations. II. Diffusion of exchangeable cations in montmorillonite. [Clay soils][J]. Annales agronomiques, 1973.

[119] CEBULA D J, THOMAS R K, MIDDLETON S, et al. Neutron diffraction from clay-water systems[J]. Clays and clay minerals, 1979,27(1): 39-52.

[120] BEREND I. Les mécanismes d'hydratation de montmorillonites homoioniques pour des pressions relatives inferieures à 0.95[D]. France (Université de soutenance) Vandoeuvre-lès-Nancy INPL - Institut National Polytechnique de Lorraine, 1991.

[121] MATE C M, MCCLELLAND G M, ERLANDSSON R, et al. Atomic-scale friction of a tungsten tip on a graphite surface[J]. Physical Review Letters, 1987,59(17): 1942-1945.

[122] FILLETER T, MCCHESNEY J L, BOSTWICK A, et al. Friction and dissipation in epitaxial graphene films[J]. Physical Review Letters, 2009,102(8): 86102.

[123] LI A, LIU Y, SZLUFARSKA I. Effects of Interfacial Bonding on Friction and Wear at Silica/Silica

Interfaces[J]. Tribology Letters, 2014,56(3): 481-490.

[124] LIU E, BLANPAIN B, CELIS J P, et al. Comparative study between macrotribology and nanotribology[J]. Journal of Applied Physics, 1998,84(9): 4859-4865.

[125] DUQUE-REDONDO E, MANZANO H, EPELDE-ELEZCANO N, et al. Molecular Forces Governing Shear and Tensile Failure in Clay-Dye Hybrid Materials[J]. Chemistry of Materials, 2014,26(15): 4338-4345.

[126] ZHAOYANG M, GAMAGE R P, CHENGPENG Z. Mechanical properties of alpha -quartz using nanoindentation tests and molecular dynamics simulations[J]. International journal of rock mechanics and mining sciences (Oxford, England : 1997), 2021,147: 104878.

[127] Yao Lu Experimental study on the medium to high velocity friction properties of fault gouges in the Longmenshan fault zone [J] International Earthquake Dynamics, 2014 (8): 2

[128] Li Wenpu Research on the mechanical properties of coal and rock and the law of gas migration under the influence of mining [D] Mining Engineering, Chongqing University, 2014

[129] FALL A, WEBER B, PAKPOUR M, et al. Sliding Friction on Wet and Dry Sand[J]. Physical Review Letters, 2014,112(17).

[130] MASUDA K, ARAI T, TAKAHASHI M. Effects of frictional properties of quartz and feldspar in the crust on the depth extent of the seismogenic zone[J]. Progress in Earth and Planetary Science, 2019,6(1).

[131] YANG L, WANG D, GUO Y, et al. Tribological behaviors of quartz sand particles for hydraulic fracturing[J]. Tribology International, 2016,102: 485-496.

[132] KANAGAWA K, MURAYAMA H, SUGITA A, et al. Weakening of quartz rocks at subseismic slip rates due to frictional heating, but not to lubrication by wear materials of hydrated amorphous silica or silica gel[J]. Tectonophysics, 2020,784: 228429.

[133] BARTHÉLÉMY J, SOUQUE C, DANIEL J. Nonlinear homogenization approach to the friction coefficient of a quartz-clay fault gouge[J]. International Journal for Numerical and Analytical Methods in Geomechanics, 2013,37(13): 1948-1968.

[134] AHARONOV E, SCHOLZ C H. A Physics-Based Rock Friction Constitutive Law: Steady State Friction[J]. Journal of Geophysical Research: Solid Earth, 2018,123(2): 1591-1614.

[135] HU J, SUN Q. The effect of high temperature and pressure on rock friction coefficient: a review[J]. International Journal of Earth Sciences, 2020,109(2): 409-419.

[136] KASYAP S S, SENETAKIS K. Experimental Investigation of the Coupled Influence of Rate of Loading and Contact Time on the Frictional Behavior of Quartz Grain Interfaces under Varying Normal Load[J]. International journal of geomechanics, 2019,19(10): 4019111-4019112.

[137] ZHANG H, LIU S, XIAO H. Sliding friction of shale rock on dry quartz sand particles[J]. Friction, 2018,7(4): 307-315.

[138] YE Z, EGBERTS P, HAN G H, et al. Load-Dependent Friction Hysteresis on Graphene[J]. ACS Nano, 2016,10(5): 5161-5168.

[139] LEVIEN L, PREWITT C T, WEIDNER D J. Structure and elastic properties of quartz at pressure[J]. American Mineralogist, 1980,65((9-10)): 920-930.

[140] ZHURAVLEV L T. The surface chemistry of amorphous silica. Zhuravlev model[J]. Colloids and Surfaces A: Physicochemical and Engineering Aspects, 2000,173(1-3): 1-38.

[141] ZHURAVLEV L T. Concentration of hydroxyl groups on the surface of amorphous silicas[J]. Langmuir, 1987,3(3): 316-318.

[142] ZHU H, ZHANG D, WANG T, et al. Understanding geopolymer binder-aggregate interfacial characteristics at molecular level[J]. Cement and concrete research, 2021,149: 1.

[143] BISH D L. Rietveld Refinement of the Kaolinite Structure at 1.5 K[J]. Clays & Clay Minerals, 1993,41(6): 738-744.

[144] PLIMPTON S. Fast Parallel Algorithms for Short-Range Molecular Dynamics[J]. Journal of Computational Physics, 1995,117(1): 1-19.

[145] TELEMAN O, JÖNSSON B, ENGSTRÖM S. A molecular dynamics simulation of a water model with intramolecular degrees of freedom[J]. Molecular physics, 1987,60(1): 193-203.

[146] BOUHADJA M, SKELTON A A. Dynamical Properties of Water and Ions at the Quartz (101)–Water Interface at a Range of Solution Conditions: A Classical Molecular Dynamics Study[J]. The Journal of Physical Chemistry C, 2018,122(3): 1535-1546.

[147] KROUTIL O, CHVAL Z, SKELTON A A, et al. Computer Simulations of Quartz (101)–Water Interface over a Range of pH Values[J]. The Journal of Physical Chemistry C, 2015,119(17): 9274-9286.

[148] DARDEN T, YORK D, PEDERSEN L. Particle mesh Ewald: AnN·log(N) method for Ewald sums in large systems[J]. The Journal of Chemical Physics, 1993,98(12): 10089-10092.

[149] MATE C M, MCCLELLAND G M, ERLANDSSON R, et al. Atomic-scale friction of a tungsten tip on a graphite surface[J]. Physical Review Letters, 1987,59(17): 1942.

[150] SENETAKIS K, COOP M R, TODISCO M C. The inter-particle coefficient of friction at the contacts of Leighton Buzzard sand quartz minerals[J]. Soils and Foundations, 2013,53(5): 746-755.

[151] LIU Z, ZHOU H, ZHANG W, et al. A new experimental method for tensile property study of quartz sandstone under confining pressure[J]. International Journal of Rock Mechanics and Mining Sciences, 2019,123: 104091.

[152] ZHAO X, HAMILTON M, SAWYER W G, et al. Thermally Activated Friction[J]. Tribology Letters, 2007,27(1): 113-117.

[153] SANG Y, DUBE M, GRANT M. Thermal effects on atomic friction[J]. Phys Rev Lett, 2001,87(17): 174301.

[154] MA Z, PATHEGAMA GAMAGE R, ZHANG C. Effects of temperature and grain size on the mechanical properties of polycrystalline quartz[J]. Computational Materials Science, 2021,188: 110138.

[155] HU Y Z, GRANICK S. Microscopic study of thin film lubrication and its contributions to macroscopic tribology[J]. Tribology letters, 1998,5(1): 81-88.

[156] ASURI S, KESHAVAMURTHY P. Expansive Soil Characterisation: an Appraisal[J]. INAE Letters, 2016,1(1): 29-33.

[157] WATANABE K, WAKE T. Measurement of unfrozen water content and relative permittivity of frozen unsaturated soil using NMR and TDR[J]. Cold Regions Science and Technology, 2009,59(1): 34-41.

[158] KOZLOWSKI T. A comprehensive method of determining the soil unfrozen water curves[J]. Cold Regions Science and Technology, 2003,36(1-3): 81-92.

[159] LIU B, LI D. A simple test method to measure unfrozen water content in clay–water systems[J]. Cold Regions Science and Technology, 2012,78: 97-106.

[160] E. P. LOZOWSKI J R S. The Icing of an Unheated, Nonrotating Cylinder. Part II. Icing Wind Tunnel Experiments[J]. 1983.

[161] MASAKAZU MATSUMOTO S S I O. Molecular dynamics simulation of the ice nucleation and growth process leading to water freezing[J]. 2002.

[162] SANZ E, VEGA C, ESPINOSA J R, et al. Homogeneous ice nucleation at moderate supercooling from molecular simulation[J]. J Am Chem Soc, 2013,135(40): 15008-15017.

[163] LUPI L, HUDAIT A, MOLINERO V. Heterogeneous Nucleation of Ice on Carbon Surfaces[J]. Journal of the American Chemical Society, 2014,136(8): 3156-3164.

[164] JOHNSTON J C, MOLINERO V. Crystallization, Melting, and Structure of Water Nanoparticles at Atmospherically Relevant Temperatures[J]. Journal of the American Chemical Society, 2012,134(15): 6650-6659.

[165] BENET J, MACDOWELL L G, SANZ E. A study of the ice-water interface using the TIP4P/2005 water model[J]. Physical chemistry chemical physics : PCCP, 2014,16(4): 22159-22166.

[166] ZHANG L, LI W, FANG T, et al. Accurate Relative Energies and Binding Energies of Large Ice–Liquid Water Clusters and Periodic Structures[J]. The Journal of Physical Chemistry A, 2017,121(20): 4030-4038.

[167] BAI G, GAO D, LIU Z, et al. Probing the critical nucleus size for ice formation with graphene oxide nanosheets[J]. Nature, 2019,576(7787): 437-441.

[168] JIN X, YANG W, GAO X, et al. Modeling the unfrozen water content of frozen soil based on the absorption effects of clay surfaces[J]. Water resources research, 2020,56(12): n/a-n/a.

[169] SOSSO G C, TRIBELLO G A, ZEN A, et al. Ice formation on kaolinite: Insights from molecular dynamics simulations[J]. The Journal of Chemical Physics, 2016,145(21): 211927.

[170] SOSSO G C, LI T, DONADIO D, et al. Microscopic Mechanism and Kinetics of Ice Formation at Complex Interfaces: Zooming in on Kaolinite[J]. The Journal of Physical Chemistry Letters, 2016,7(13): 2350-2355.

[171] COX S J, RAZA Z, KATHMANN S M, et al. The microscopic features of heterogeneous ice nucleation may affect the macroscopic morphology of atmospheric ice crystals[J]. Faraday Discussions, 2014,167: 389.

[172] ZIELKE S A, BERTRAM A K, PATEY G N. Simulations of Ice Nucleation by Kaolinite (001) with Rigid and Flexible Surfaces[J]. The journal of physical chemistry B, 2016,120(8): 1726-1734.

[173] MASON B J. Ice-nucleating properties of clay minerals and stony meteorites[J]. Quarterly journal of the Royal Meteorological Society, 1960,86(370): 552-556.

[174] HU X L, MICHAELIDES A. Ice formation on kaolinite: Lattice match or amphoterism?[J]. Surface science, 2007,601(23): 5378-5381.

[175] BERNAL J D, FOWLER R H. A Theory of Water and Ionic Solution, with Particular Reference to Hydrogen and Hydroxyl Ions[J]. The Journal of Chemical Physics, 1933,1(8): 515-548.

[176] WEI P, ZHUANG D, ZHENG Y, et al. Temperature and pressure effect on tensile behavior of ice-Ih under low strain rate: A molecular dynamics study[J]. Journal of Molecular Liquids, 2022,355: 118945.

[177] WEBER B, NAGATA Y, KETZETZI S, et al. Molecular Insight into the Slipperiness of Ice[J]. The Journal of Physical Chemistry Letters, 2018,9(11): 2838-2842.

[178]   AMARASINGHE P M, ANANDARAJAH A, GHOSH P. Molecular dynamic study of capillary forces on clay particles[J]. Applied Clay Science, 2014,88-89: 170-177.

[179]   BLAZQUEZ S, VEGA C. Melting points of water models: Current situation[J]. The Journal of Chemical Physics, 2022,156(21): 216101.

[180]   GARCÍA FERNÁNDEZ R, ABASCAL J L F, VEGA C. The melting point of ice Ih for common water models calculated from direct coexistence of the solid-liquid interface[J]. The Journal of Chemical Physics, 2006,124(14): 144506.

[181]   WANG H, QIAN H, GAO Y, et al. Classification and physical characteristics of bound water in loess and its main clay minerals[J]. Engineering Geology, 2020,265: 105394.

[182]   MATSUMOTO M, SAITO S, OHMINE I. Molecular dynamics simulation of the ice nucleation and growth process leading to water freezing[J]. NATURE, 2002,416.

[183]   ANDERSON D M, TICE A R. PREDICTING UNFROZEN WATER CONTENTS IN FROZEN SOILS FROM SURFACE AREA MEASUREMENTS[J]. highway research record, 1972.

[184]   TSYTOVICH N A. The mechanics of frozen ground[Z]. SWINZOW G K. New York, N. Y: McGraw-Hill Book Co, 1975.

[185]   FURUKAWA Y, YAMAMOTO M, KURODA T. Ellipsometric study of the transition layer on the surface of an ice crystal[J]. Journal of Crystal Growth, 1987,82(4): 665-677.

[186]   SMIT W J, BAKKER H J. The Surface of Ice Is Like Supercooled Liquid Water[J]. Angewandte Chemie, 2017,129(49): 15746-15750.

[187]   SMIT W J, TANG F, SANCHEZ M A, et al. Excess Hydrogen Bond at the Ice-Vapor Interface around 200 K[J]. Phys Rev Lett, 2017,119(13): 133003.

[188]   SPOSITO G. Single-particle motions in liquid water. II. The hydrodynamic model[J]. The Journal of Chemical Physics, 1981,74(12): 6943-6949.

[189]   CHEN Y Y, XIAO K L, YUE J Z, et al. Atomistic study on the anomalous temperature-dependent dynamic tensile strength of ice under shock loading[J]. Philosophical magazine (Abingdon, England), 2021: 1-16.

[190]   GOLD L W. Engineering properties of fresh-water ice[J]. Journal of Glaciology, 1977,19(81): 197-212.

[191]   FALENTY A, HANSEN T C, KUHS W F. Formation and properties of ice XVI obtained by emptying a type sII clathrate hydrate[J]. Nature, 2014,516(7530): 231-233.

[192]   LOBBAN C, FINNEY J L, KUHS W F. The structure of a new phase of ice[J]. Nature, 1998,391(6664): 268-270.

[193]   CAO P, WU J, ZHANG Z, et al. Mechanical properties of bi- and poly-crystalline ice[J]. AIP Advances, 2018,8(12): 125108.

[194]   VOOSEN P. New feedbacks speed up the demise of Arctic sea ice[J]. Science, 2020,369: 1043-1044.

[195]   ZHANG Y, WANG Q, HAN D, et al. Dynamic splitting tensile behaviours of distilled-water and river-water ice using a modified SHPB setup[J]. International Journal of Impact Engineering, 2020,145: 103686.

[196]   BINDSCHADLER, ROBERT, A., et al. Tidally Controlled Stick-Slip Discharge of a West AntarcticIce Stream.[J]. Science, 2003,301(5636): 1087-1090.

[197]   LI X, JIN X, WANG X, et al. Investigation of permafrost engineering geological environment with

electrical resistivity tomography: A case study along the China-Russia crude oil pipelines[J]. Engineering Geology, 2021,291: 106237.

[198] KIM H, KEUNE J N. Compressive strength of ice at impact strain rates[J]. Journal of Materials Science, 2007,42(8): 2802-2806.

[199] SHAZLY M, PRAKASH V, LERCH B A. High strain-rate behavior of ice under uniaxial compression[J]. International Journal of Solids and Structures, 2009,46(6): 1499-1515.

[200] WU X, PRAKASH V. Dynamic compressive behavior of ice at cryogenic temperatures[J]. Cold Regions Science and Technology, 2015,118: 1-13.

[201] SALETTI D, GEORGES D, GOUY V, et al. A study of the mechanical response of polycrystalline ice subjected to dynamic tension loading using the spalling test technique[J]. International Journal of Impact Engineering, 2019,132: 103315.

[202] GODIO A, REGE R B. The mechanical properties of snow and ice of an alpine glacier inferred by integrating seismic and GPR methods[J]. Journal of Applied Geophysics, 2015,115: 92-99.

[203] ELVIN A A. Number of grains required to homogenize elastic properties of polycrystalline ice[J]. Mechanics of materials, 1996,22(1): 51-64.

[204] QIU W, PENG R. Research on the numerical simulation for plastic model of ice as building materials under triaxial compression[J]. Construction and Building Materials, 2021,268: 121183.

[205] XIAO S, SKALLERUD B H, WANG F, et al. Enabling sequential rupture for lowering atomistic ice adhesion[J]. Nanoscale, 2019,11(35): 16262-16269.

[206] XIAO S, HE J, ZHANG Z. Nanoscale Deicing by Molecular Dynamics Simulation[J]. Nanoscale, 2016,8(30): 14625-14632.

[207] NAVABI A M H. Mechanical Characterization via Full Atomistic Simulation: Applications to Nanocrystallized Ice[Z]. Ann Arbor: ProQuest Dissertations & Theses, 2016.

[208] YIN Q, HU L, WU X, et al. Temperature-dependent phase transformation of ice-1h under ultrafast uniaxial compression: A molecular dynamics simulation[J]. Computational Materials Science, 2019,162: 340-348.

[209] NIELS B. Structure and Properties of Ice[J]. Science, 1952,115(2989): 385-390.

[210] BERENDSEN H, GRIGERA J R, STRAATSMA T P. The missing term in effective pair potentials[J]. Journal of Physical Chemistry, 1987,91(24): 6269-6271.

[211] GAY S C, SMITH E J, HAYMET A D J. Dynamics of melting and stability of ice 1h: Molecular-dynamics simulations of the SPC/E model of water[J]. The Journal of Chemical Physics, 2002,116(20): 8876-8880.

[212] ZHANG Z, DUAN Z. Prediction of the PVT properties of water over wide range of temperatures and pressures from molecular dynamics simulation[J]. Physics of the Earth and Planetary Interiors, 2005,149(3-4): 335-354.

[213] RYCKAERT J P, CICCOTTI G, BERENDSEN H. Numerical integration of the cartesian equations of motion of a system with constraints: molecular dynamics of n-alkanes[J]. J.Comput.Phys, 1977,23(3): 327-341.

[214] HOOVER W G. Canonical dynamics: Equilibrium phase-space distributions[J]. Phys Rev A Gen Phys, 1985,31(3): 1695-1697.

[215] DEL ROSSO L, CELLI M, GRAZZI F, et al. Cubic ice Ic without stacking defects obtained from ice XVII[J]. Nature Materials, 2020,19(6): 663-668.

[216] YANG H, HE M, LU C, et al. Deformation and failure processes of kaolinite under tension: Insights from molecular dynamics simulations[J]. Science China Physics, Mechanics & Astronomy, 2019,62(6): 64612.

[217] ZHANG Y, GAO S, DU X, et al. Molecular dynamics simulation of strength weakening mechanism of deep shale[J]. Journal of Petroleum Science and Engineering, 2019,181: 106123.

[218] Guo Yao, Li Gang, Jia Chengyan, et al Research on Ultrasonic Testing of Ice Mechanical Parameters [J] Polar Research, 2016,28 (01): 152-157

[219] FLETCHER, N. H. The Chemical Physics of Ice: Mechanical properties[J]. 1970,10.1017/CBO9780511735639(CHAPTER 8): 165-197.

[220] GOLD L W. On the elasticity of ice plates[J]. Canadian journal of civil engineering, 1988,15(6): 1080-1084.

[221] WAITE W F, HELGERUD M B, NUR A, et al. Laboratory Measurements of Compressional and Shear Wave Speeds through Methane Hydrate[J]. Annals of the New York Academy of Sciences, 2000,912(1): 1003-1010.

[222] STUKOWSKI A. Visualization and analysis of atomistic simulation data with OVITO–the Open Visualization Tool[J]. Modelling and simulation in materials science and engineering, 2010,18(1): 15012.

[223] YAO Y, LI J, NI J, et al. Effects of gravel content and shape on shear behaviour of soil-rock mixture: Experiment and DEM modelling[J]. Computers and Geotechnics, 2022,141: 104476.

[224] KAYADELEN C, GÜNAYDıN O, FENER M, et al. Modeling of the angle of shearing resistance of soils using soft computing systems[J]. Expert Systems with Applications, 2009,36(9): 11814-11826.

[225] DU K, LI X, WANG S, et al. Compression-shear failure properties and acoustic emission (AE) characteristics of rocks in variable angle shear and direct shear tests[J]. Measurement, 2021,183: 109814.